CHAPTER I

INTRODUCTION

Cytochrome P450s

Cytochrome P450s are ~ 50 kDa hemoproteins found throughout nature, with 57 P450s encoded in the human genome (1). The heme protoporphyrin IX prosthetic group, linked with the axial cysteine residue, imparts unique chemistry and spectroscopic properties to this important family of enzymes. Evidence of cytochrome P450s was first identified in 1958, when a pigment was observed in microsomal fractions from pig (2) and rat liver (3) following reduction and treatment with CO. P450s were first characterized in 1962 (4), although at this time P450 was believed to be a single enzyme. In 1964, Omura and Sato named the enzyme cytochrome P450 for "pigment 450," due to the observation that the reduced form of the enzyme binds CO to form a maximal absorbance band at 450 nm (5). The same year, P450 was classified as a hemoprotein, and the molar extinction coefficient for CO binding to reduced P450 was measured in the seminal work by Omura and Sato, allowing future researchers a facile means of measuring P450 concentrations (5, 6). In 1963, Estabrook et al. determined that P450 functions as the terminal oxygenase by demonstrating the hydroxylation of 17-hydroxylprogesterone (a reaction later attributed to P450 21A2) (7). When the hemoprotein (with CO bound) was exposed to light of discrete wavelengths, the wavelength at which the protein had an absorbance maximum caused the reversal of the inhibition by CO. The finding that this wavelength was at 450 nm showed that P450 was

the terminal oxygenase, uniting two observations: a hemoprotein bound CO in its reduced form with a maximal absorbance at 450 nm (i.e. P450), and microsomes (i.e. P450) can carry out oxidations.

For most microsomal P450 reactions, a second enzyme – NADPH-cytochrome P450 reductase – is required for electron transfer. This enzyme facilitates the flow of electrons from NADPH to FAD, FMN, and finally to the iron of the P450. While the requirement for NADPH-cytochrome P450 reductase for many microsomal reactions had been established, it was thought to be coupled only to cytochrome *c* (hence its original name, "NADPH-cytochrome *c* reductase"). The presence of NADPH-cytochrome *c* reductase in the endoplasmic reticulum was shown in 1962, suggesting that a second protein must be present in this organelle to serve as an electron acceptor (8). The requirement for NADPH-cytochrome P450 reductase for P450 catalysis was unequivocally resolved in 1968 by Lu and Coon when they showed ω-hydroxylation of fatty acids required fractions of cytochrome P450, NADPH-cytochrome P450 reductase, and lipid (9). This was the first time that a reconstituted P450 system was used successfully. Vermilion and Coon purified the reductase from rat in 1974 (10).

The realization was made that cytochrome P450 was actually made up of several families of P450 enzymes when multiple forms were isolated in rabbit in 1975 (11). Guengerich, Lu, and Levin developed some standard protocols for the very difficult purification of multiple P450s from rats (12-14), and Guengerich went on to identify and purify for the first time human P450s 2C9 (15), 2D6 and 1A2 (16), and 3A4 (17).

The first P450 ($P450_{cam}$) was crystallized in 1985 by Poulos et al. (18) and the structure was solved in 1987 (19). For nearly a decade, $P450_{cam}$ remained the lone P450

characterized by x-ray crystallography, although numerous crystal structures were published with this P450 bound to various ligands. Finally, in 1995, structures for P450 BM3 (20) and P450 eryF (21) were solved, and soon after, the number of protein data bank deposits soared. Since then dozens of structures of P450s, including mammalian P450s (22), have been solved. In 2007, a structure of human P450 1A2 complexed with αNF was solved, although as discussed in Chapter II, it is unlikely that the ligand is in a catalytically competent position (Figure 1) (23). Ghosh et al. solved the structure for P450 19A1 in the presence of andro in 2009 (Figure 2) (24). This was the first time a crystal structure resulted from protein purified from an animal (in this case, human tissue was used). The general cytochrome P450 structure consists of primarily of α-helices that among many things help anchor the heme prosthetic group and control active site accessibility. P450s with ≥ 40% sequence identity are classified in the same family and are designated with a number (P450 1, P450 2, etc.), while subfamilies that contain ≥ 55% sequence identity are identified with a letter (P450 1A, P450 1B, etc.) The final number gives each P450 gene (or protein) a unique identity (P450 1A1, 1A2, etc.) (1).

P450s are involved in the metabolism of 75% of the drugs currently on the market (25) and much focus has been in the context of pharmaceutical research, but many P450s are capable of catalyzing reactions involving endogenous substrates (e.g. fat-soluble vitamins, steroids, and eicosanoids) (26) (Table 1). Typically P450s that oxidize exogenous compounds have larger active sites in order to accommodate a wide variety of drugs, pesticides, and pollutants, while P450s that utilize endogenous substrates tend to be less promiscuous and have smaller active sites. Important exceptions to this include

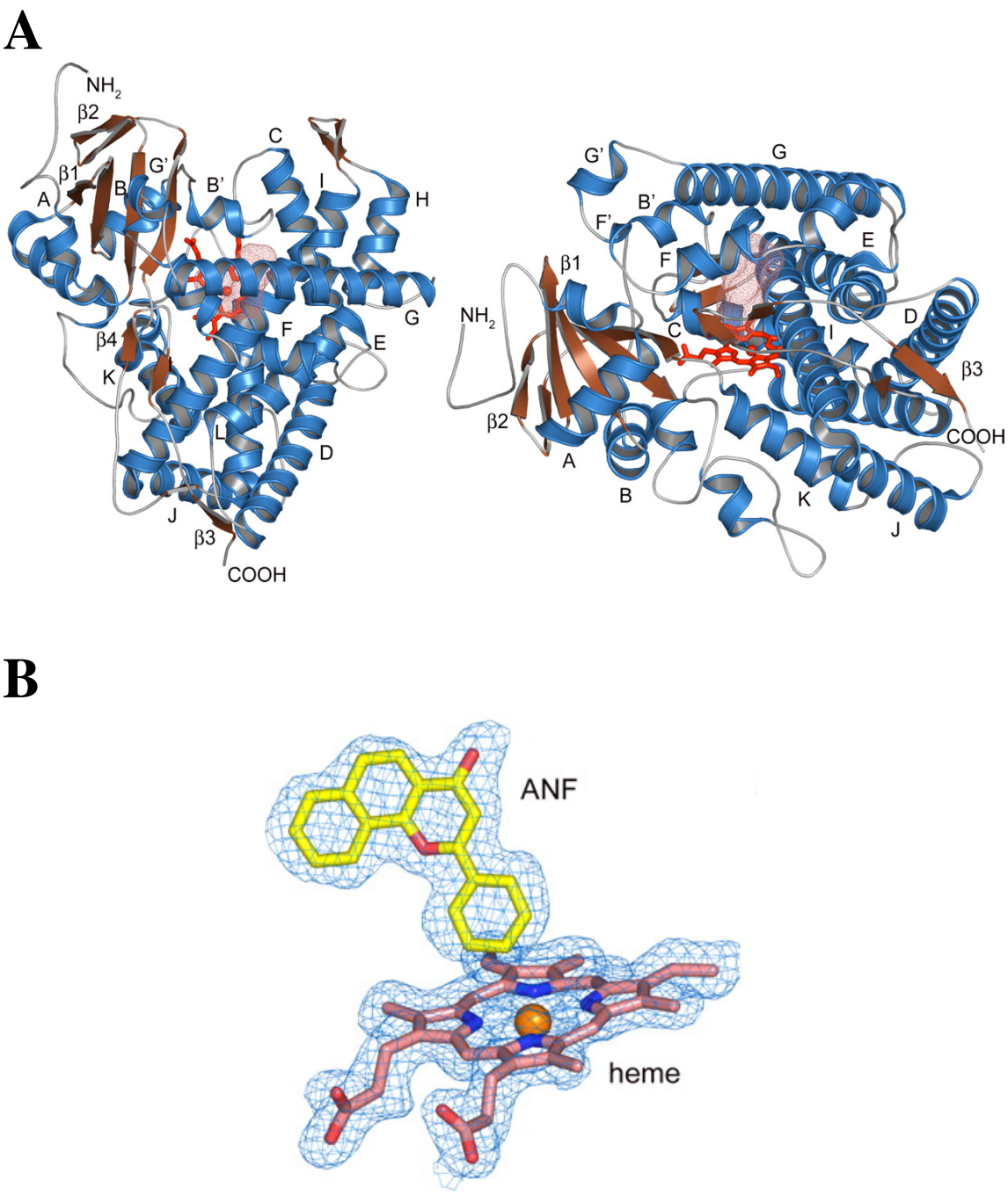

Figure 1. X-ray crystal structure of human P450 1A2 complexed with αNF. *A*, Shown in red is the heme, and the red electron density signifies the active site pocket. *B*, Relative orientation of αNF relative to the heme. From (23).

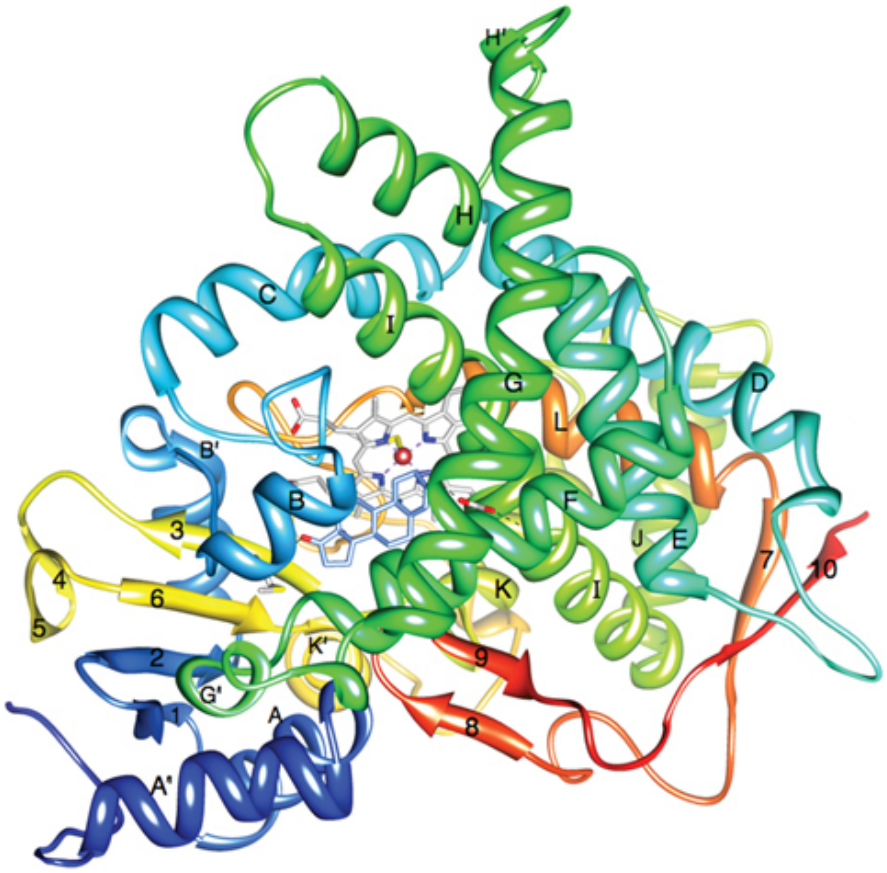

Figure 2. X-ray crystal structure of human P450 19A1 complexed with andro. From (24).

Table 1. Classification of cytochrome P450s based on their major substrates. Modified from Guengerich et al. (27).

Sterols	Xenobiotics	Fatty acids	Eicosanoids	Vitamins	Unknown
1B1	1A1	2J2	4F2	2R1	2A7
7A1	1A2	4A11	4F3	24	2S1
7B1	2A6	4B1	4F8	26A1	2U1
8B1	2A13	4F12	5A1	26B1	2W1
11A1	2B6		8A1	26C1	3A43
11B1	2C8			27B1	4A22
11B2	2C9				4F11
17	2C18				4F22
19	2C19				4V2
21A2	2D6				4X1
27A1	2E1				4Z1
39	2F1				20A1
46	3A4				27C1
51	3A5				
	3A7				

P450 2A6, which has an active site volume that is ~ 25% of that of other drug metabolizing P450s (28), and the active site of 2E1 is even smaller (29). Both enzymes preferentially oxidize exogenous substrates.

P450s typically catalyze monooxygenations and are also capable of reduction, ring expansion, dealkylation, aromatization, and other reactions based on the same high-valent iron chemistry (examples of the most common reactions catalyzed by P450s are shown in Figure 3) (30). A generalized P450 catalytic cycle is shown in Figure 4. Typically the first step is binding of the substrate to the ferric form (not coordinating with the iron itself). Following reduction of the heme to the ferrous form, oxygen then binds to the P450. A second reduction and the addition of a proton occur to generate a ferrous peroxide intermediate. Loss of water generates "Compound I," the unstable intermediate thought to perform most reactions. While the overall configuration of Compound I is more complex, it is typically denoted as "FeO^{3+}." Hydroxylation by Compound I is followed by product release, and the ferric form of the enzyme is regenerated. The overall stoichiometry is (RH is a substrate):

$$RH + O_2 + NADPH + H^+ \rightarrow ROH + H_2O + NADP^+$$

Sequential P450s

An unusual feature of some P450s is the ability to catalyze multi-step, sequential reactions. Recent examples include P450s catalyzing multi-step reactions with exogenous substrates such as P450s 1A2 (32), 2A6 (33), and 2E1 (34). The two-step oxidation of

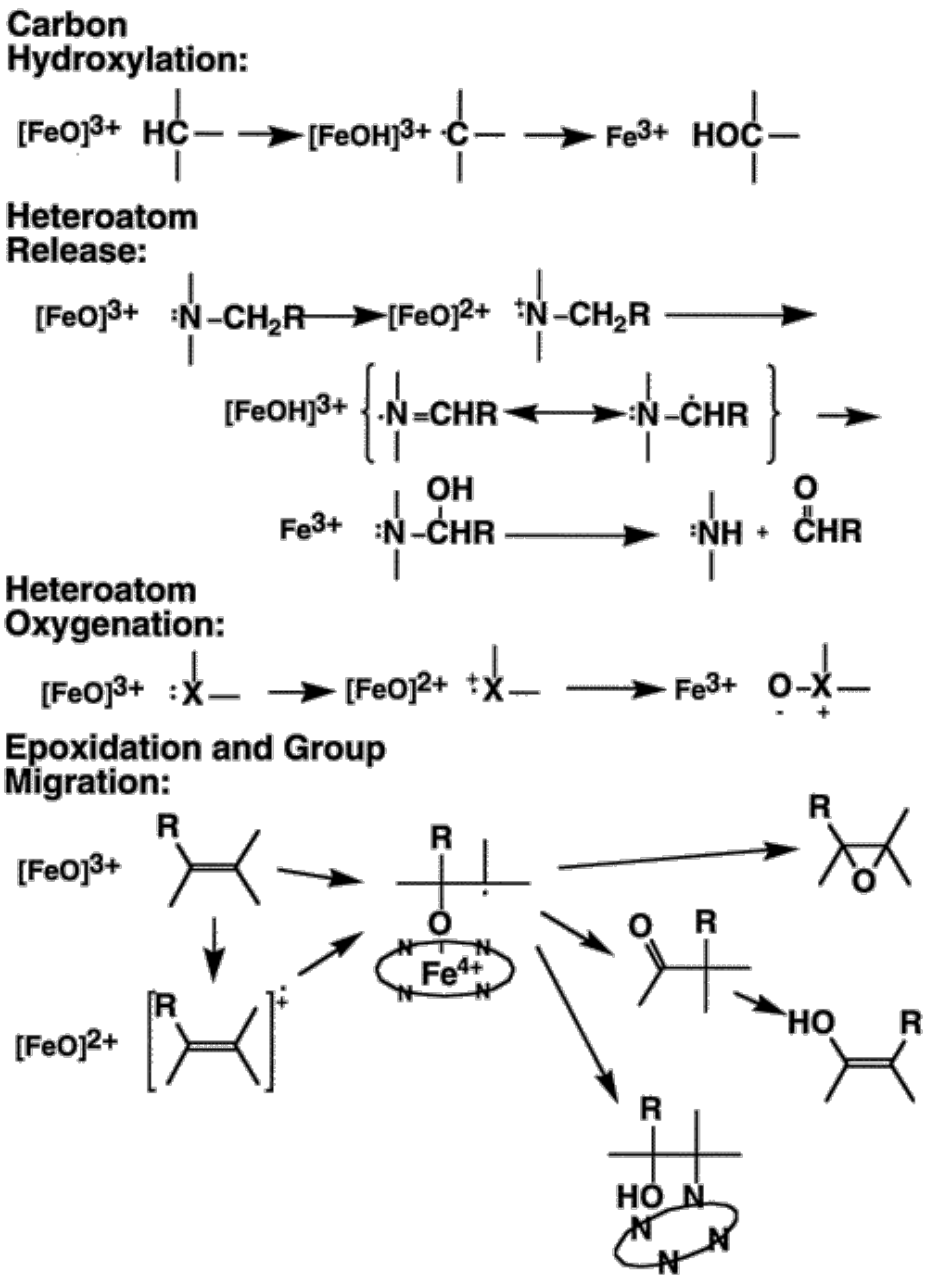

Figure 3. **A collection of common reactions catalyzed by cytochrome P450s.** From (31).

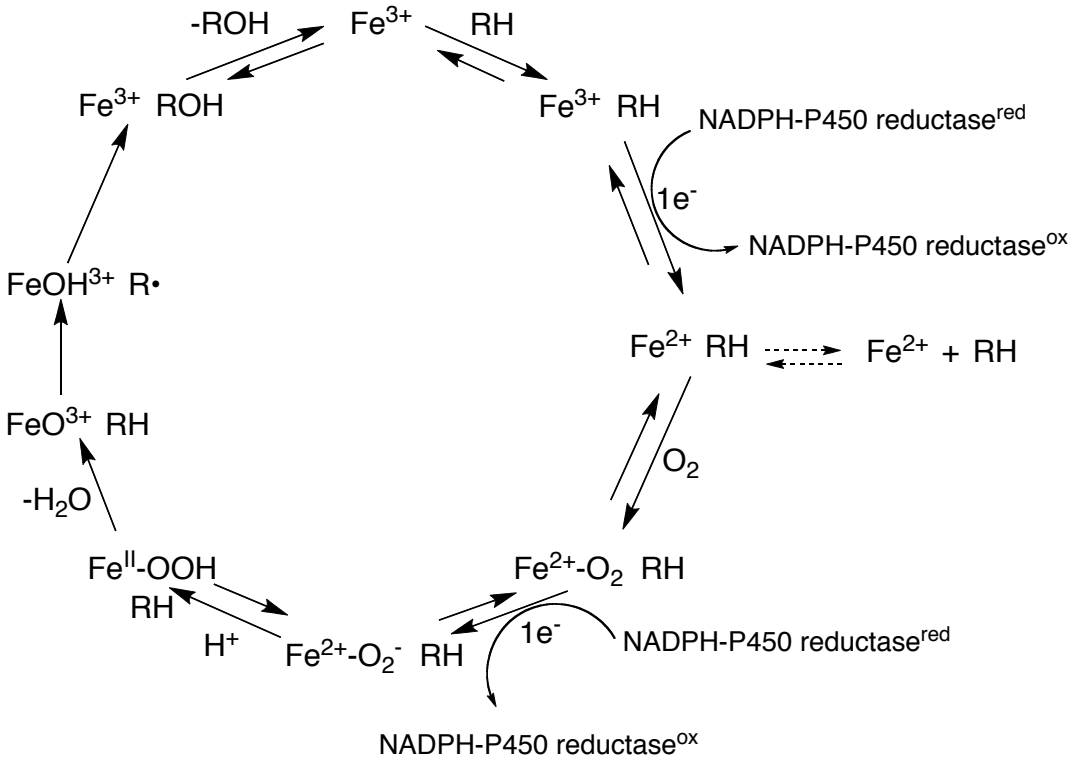

Figure 4. Generalized cytochrome P450 catalytic cycle.

pyrene by P450 1A2 is the focus of Chapter II. In this case, P450 1A2 catalyzes the conversion of the polycyclic aromatic hydrocarbon pyrene first to 1-OH pyrene and then to at least four different di-OH pyrene compounds (Figure 5). The capability to catalyze sequential reactions was not extended to all substrates; for example, in this study only one product was seen in the case of αNF oxidation by P450 1A2.

These multi-step processes are more commonly associated with P450s involved in steroid metabolism (P450s 11A1, 11B2, 17A1, 19A1, and 51A1). As discussed, many P450s catalyze oxidations, but sequential reactions often include more unusual chemistry, including aromatizations, side chain cleavages, etc. (Figure 6). Pregnenolone and aldosterone are generated from P450 11A1 and 11B2 reactions, respectively, in three-step processes. P450 17A1 exhibits both steroid 7α-hydroxylation and lyase activities in a two-step reaction to generate androstenedione from progesterone, and, in a separate pathway, generating dehydroepiandrosterone from pregnenolone. P450 51A1 is a key enzyme in the cholesterol biosynthetic pathway and catalyzes a three-step *C*-demethylation of the substrate lanosterol. The focus of Chapter IV is P450 19A1, which catalyzes a three-step reaction to convert androgens to estrogens (Figure 7). Two relatively stable intermediates (a 19-hydroxy and a 19-aldehyde intermediate) are formed in succession before the aromatization of the steroid A ring and the loss of formic acid. It is from this final step that the common name for P450 19A1, aromatase, was derived.

A few laboratories have undertaken pre-steady-state studies to characterize the kinetics of sequential P450s and the relative processive (i.e. the intermediates do not dissociate over the course of turnover) or distributive (i.e there is some or complete exchange of intermediates) nature over the course of the multi-step reaction. The focus

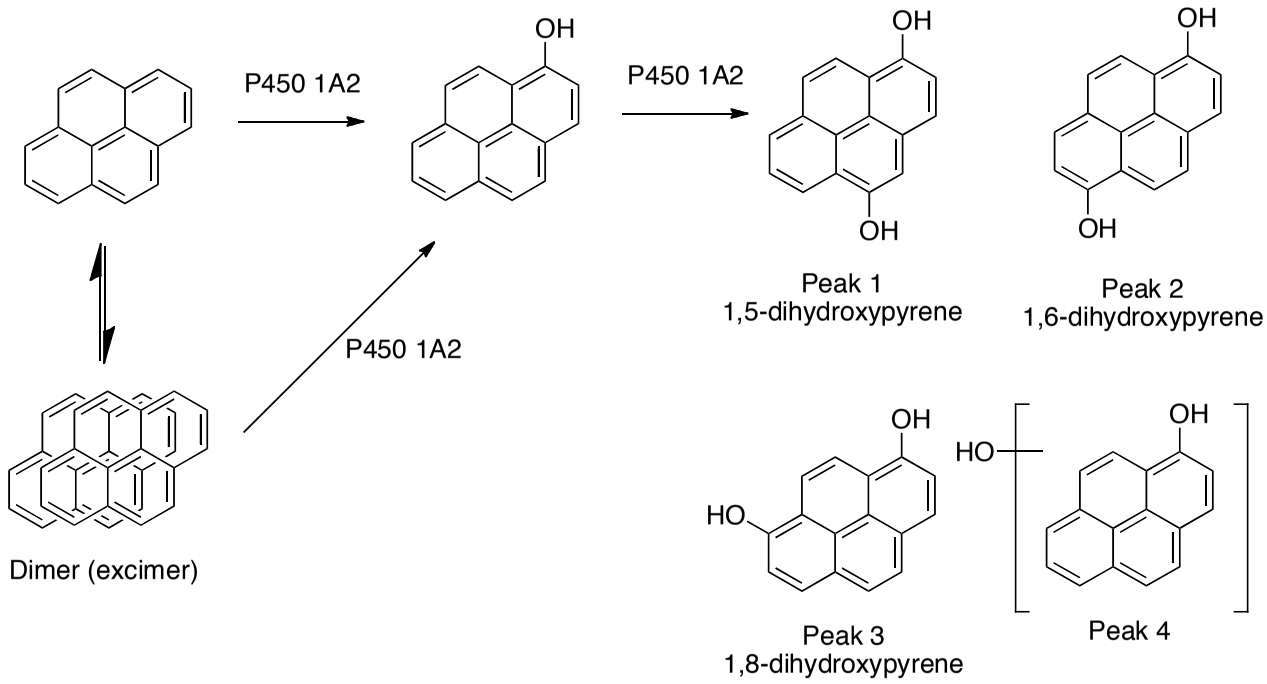

Figure 5. Oxidation of pyrene by P450 1A2.

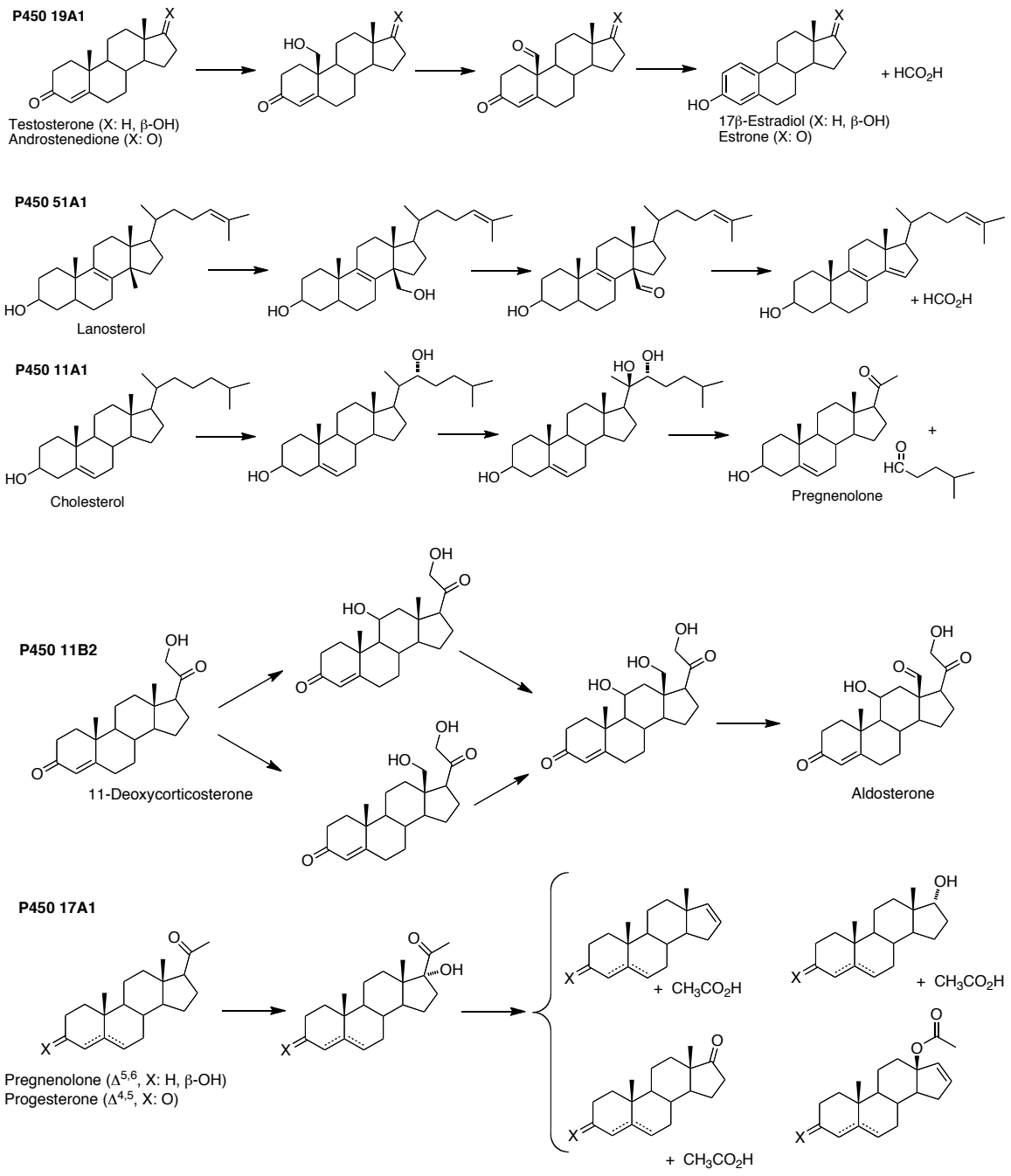

Figure 6. Examples of sequential reactions catalyzed by cytochrome P450s.

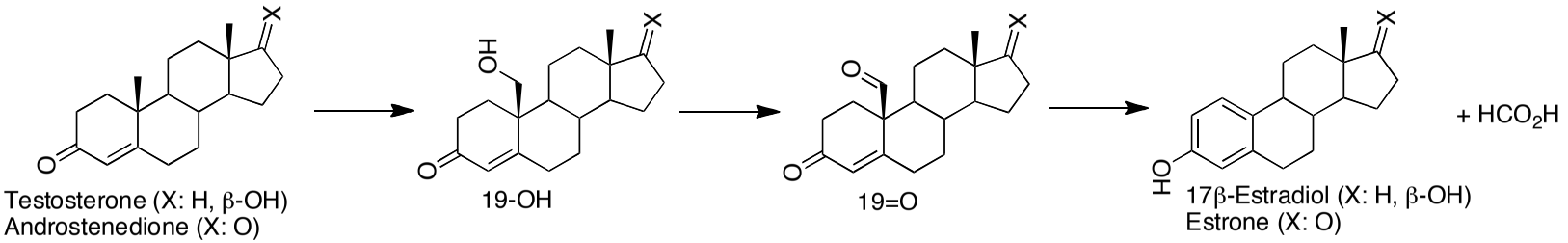

Figure 7. Conversion of androgens to estrogens by P450 19A1.

has been on P450s 2A6 (33), 2E1 (34), 11B2 (35), and 17A1 (36). The most common method to determine the extent of processivity is the use of a pulse-chase assay. NADPHis added to an incubation of P450 with radiolabeled substrate to initiate the reaction. At some timepoint(s), an excess of nonradiolabeled intermediate is added. After quenching the reaction, the relative amount of radiolabel present in the product in the absence *vs*. the presence of nonlabeled intermediate treatment is measured. A high percentage of label retention indicates processivity, while a low percentage shows a more distributive mechanism, meaning that the radiolabeled intermediate was displaced at least in part by the nonlabeled intermediate.

In the case of P450 2A6, a variety of steady-state and pre-steady state kinetics were used to generate a global fit for the conversion of nitrosamines to aldehydes and then carboxylic acids. In addition to generating individual rate constants for the steps of turnover, pulse-chase studies were used to determine the degree of processivity. Two different substrates were examined, and in one case, 80-90% of the radiolabel was retained in the product, while 40-60% was retained in the other (33). For the conditions of these experiments, complete exchange (i.e. fully distributive) would yield 5-10% label retention, so P450 2A6 proved to be either highly processive or relatively processive, depending on the substrate.

The conversion of ethanol to acetic acid and then acetaldehyde by P450 2E1 was also studied rigorously to produce a kinetic model containing individual rate constants (34). Product retention was either 40% or 80%, depending on whether the non-labeled intermediate pulse was four times the initial substrate concentration or 1.3 times, respectively. Like P450 2A6, P450 2E1 proved to be relatively processive, with little

exchange of the intermediate during turnover. In both P450s 2A6 and 2E1 studies the dissociation constants for the two intermediates were found to be in the mM range, so it is important to note that low K_d values do not imply processivity (*vide infra*, Chapter IV) and vice versa.

Individual rate constants associated with the chemistry and dissociation steps were measured for P450 11B2, although those associated with ligand binding were not determined (35). By using a rapid chemical-quench apparatus (*vide infra*) and radiolabeled substrates, progress curves were generated from radio-HPLC chromatograms to show the relative concentrations of substrate, intermediates, and product with respect to time, which was then fit mathematically to derive individual rate constants. Although pulse-chase studies were not performed, it was concluded (based on rapid chemical-quench experiments) that very little exchange occurs during the conversion of deoxycorticosterone to corticosterone and 18-hydroxycorticosterone to finally form the product aldosterone. This study ended the controversy surrounding the first step of the sequential reaction; namely, that corticosterone rather than 18-hydroxydeoxycorticosterone was first formed. The rate limiting step in this reaction was found to be product release, and steady-state studies revealed a k_{cat} of 0.02 s^{-1} for the converstion of dexoycorticosterone to aldosterone.

Similar studies have measured individual rate constants for P450 17A1 (37), again focusing on the chemistry and dissociation steps. P450 17A1 is capable of processing two different substrates. In the Δ^5 pathway, pregnenolone is converted first to 17α-hydroxy-pregnenolone and then dehydroepiandrosterone. In the Δ^4 pathway, progesterone is converted to 17α-hydroxy-progesterone and then to androstenedione. In the experimental

system used (purified heterologously expressed P450 17A1), all steroids in the Δ^5 pathway could be isolated, and all but androstenedione were observed in the Δ^4 pathway. In pulse-chase studies, there was no change in radiolabel retention upon addition of nonlabeled 17α-hydroxypregnenolone, indicating a processive mechanism (specifically, 20% of the label was found in the product, regardless of the addition of non-labeled intermediate) for the Δ^5 pathway. The dissociation rate of 17α-hydroxy-progesterone was measured to be 10-fold faster than that for 17α-hydroxy-pregnenolone, which may (or may not) suggest that Δ^4 pathway is distributive (to the extent that conversion of 17α-hydroxy-progesterone to androstenedione formation is prevented in this system). However, studies by another laboratory (using HEK-293 cells transfected with P450 17A1) concluded that 17α-hydroxy-pregnenolone freely dissociates in the Δ^5 pathway (38). However, most sequential P450 studies to date indicate that these multi-step reactions are more processive than distributive, regardless of the preference for endogenous *vs*. exogenous substrates, and some prove highly processive with some substrates.

Much debate surrounds the degree of intermediate exchange for P450 19A1 (*vide infra*, Chapter IV), and it is hypothesized that how processive or distributive this enzyme is can be determined through kinetic experiments (i.e. pulse chase studies). Steady-state time course reactions of conversion of andro to estrone implied exchangeable intermediates (39, 40), but studies using chemically modified intermediates instead suggested processivity (41). All of these studies used microsomes rather than purified P450 19A1, and in at least one case it was unclear what the relative concentrations of substrate and P450 19A1 were. More rigorous testing with purified P450 19A1, as in the

case of P450s 2A6, 2E1, and 17A1, would reveal the degree of processivity. Such experimentation is described in Chapter IV. Based on previous work with sequential P450s, it was hypothesized that P450 19A1 would reveal a more processive than distributive mechanism.

No studies have been undertaken to determine the degree of processivity associated with P450 51A1. As this reaction closely resembles that of P450 19A1 (i.e. formation of first a hydroxy and then an aldehyde intermediate) it would be interesting to examine how useful 19A1 pulse-chase assays are for modeling the P450 51A1 reaction and degree of processivity.

Steady-State and Pre-Steady-State Kinetics and Techniques

Identifying substrates, any stable intermediates, and products related to enzyme turnover is an important first step in characterization, but any serious study on an enzyme should include an analysis of the kinetics. The implications from kinetic studies can aid work in many other disciplines, including pharmacology (i.e. aid in designing inhibitors, pharmacokinetic studies, etc.) and molecular biology (breakdown/synthesis rates of signaling molecules such as hormones, etc.).

The most common type of enzyme kinetic analysis involves steady-state methods in which the constants k_{cat} (a first order rate constant for the rate-limiting step in catalysis) k_{cat}/K_m (a measurement of enzyme efficiency), and K_m (the concentration of substrate required to reach one-half the rate of the maximal velocity of the reaction) are obtained. Typically reactions are set up in which the enzyme is incubated with varying concentrations of substrate, the reaction is quenched at some defined time point, and the

amount of product formed is measured by some means (quantitation typically using spectroscopy and appropriate internal or external standards).

In the case of heterologously purified monocistronic P450s such as P450s 1A2 and 19A1 discussed in Chapters II-IV (*vs*. bicistronic P450s in which the expression vector contains the P450 gene in addition to the gene for NADPH-cytochrome P450 reductase), membranes have to be reconstituted in the form of lipid vesicles prior to incubation with substrate. These vesicles are formed by a brief incubation (typically 5 min at room at 25 °C) of a synthetic phospholipid (e.g. L-α-1,2-dilauroyl-*sn*-glycero-3-phosphocholine), NADPH-cytochrome P450 reductase, and the purified P450, typically in a ~ 100:2:1 ratio. Some reconstitution is much more complicated, as in the case of P450 3A4, which requires additional lipids, cytochrome b_5, and the detergent cholate (42).

Dissociation constants (K_d) are also useful parameters for characterizing enzymes and are usually easily obtained for P450s owing to unique spectral properties. Substrates usually display "Type I" changes (increase at 390 nm and decrease at 420 nm) as binding of the ligand causes displacement of H_2O as the sixth axial ligand. This type of spectral change indicates the shift from a low-spin to a high-spin iron state. When the iron of the enzyme is in a high-spin state, this typically increases its reduction potential, which is important for completing the next step in the P450 catalytic cycle (Figure 4). "Type II" changes show the opposite spectral changes (decrease at 390 nm and increase at 420 nm) and are due to direct coordination to the heme iron (43), indicating a shift of the iron to a low-spin state and actually liganding to the iron.

In order to obtain the individual rate constants of the various steps in the P450 catalytic cycle (Figure 4), pre-steady-state techniques are employed. Two instruments imperative for such studies are the stopped-flow spectrophotometer (Figure 8) and the rapid chemical-quench apparatus (Figure 9). A stopped-flow spectrophotometer instrument requires spectroscopic output for measurements (typically absorbance or fluorescence, but CD can also be used), and can measure extremely fast changes associated with binding, turnover, etc. with a dead-time of 2 ms or less. The contents of two syringes are rapidly mixed in a cell that is monitored by UV-vis or fluorescence (or CD). To quench the reaction (or, more precisely, to stop observing the spectral changes), a stop syringe pushes the contents out of the cell at a time point defined by the user via a computer.

A chemical-quench system does not rely on spectroscopic output and thus can measure many steps of turnover essentially silent in spectroscopy. Rate constants associated with turnover are examined typically using radiolabeled starting materials. Two drive syringes containing buffer are used to push the contents of the two sample syringes (one containing P450 and substrate, and another with NADPH) out of the sample loop and into a reaction loop. The length of this loop determines the length of the reaction. The reaction is quenched by pushing the sample out of the loop, where it meets the contents of a third drive syringe, the quench. Typically metal chelators, acids, salts, or organic solvents are used to stop the reaction, depending on the particular enzyme used. Care must be taken when selecting a quench material to ensure that the substrates, intermediates, and products do not undergo further chemistry upon quenching. After collecting the samples from the various time points (i.e. various loops), the compounds

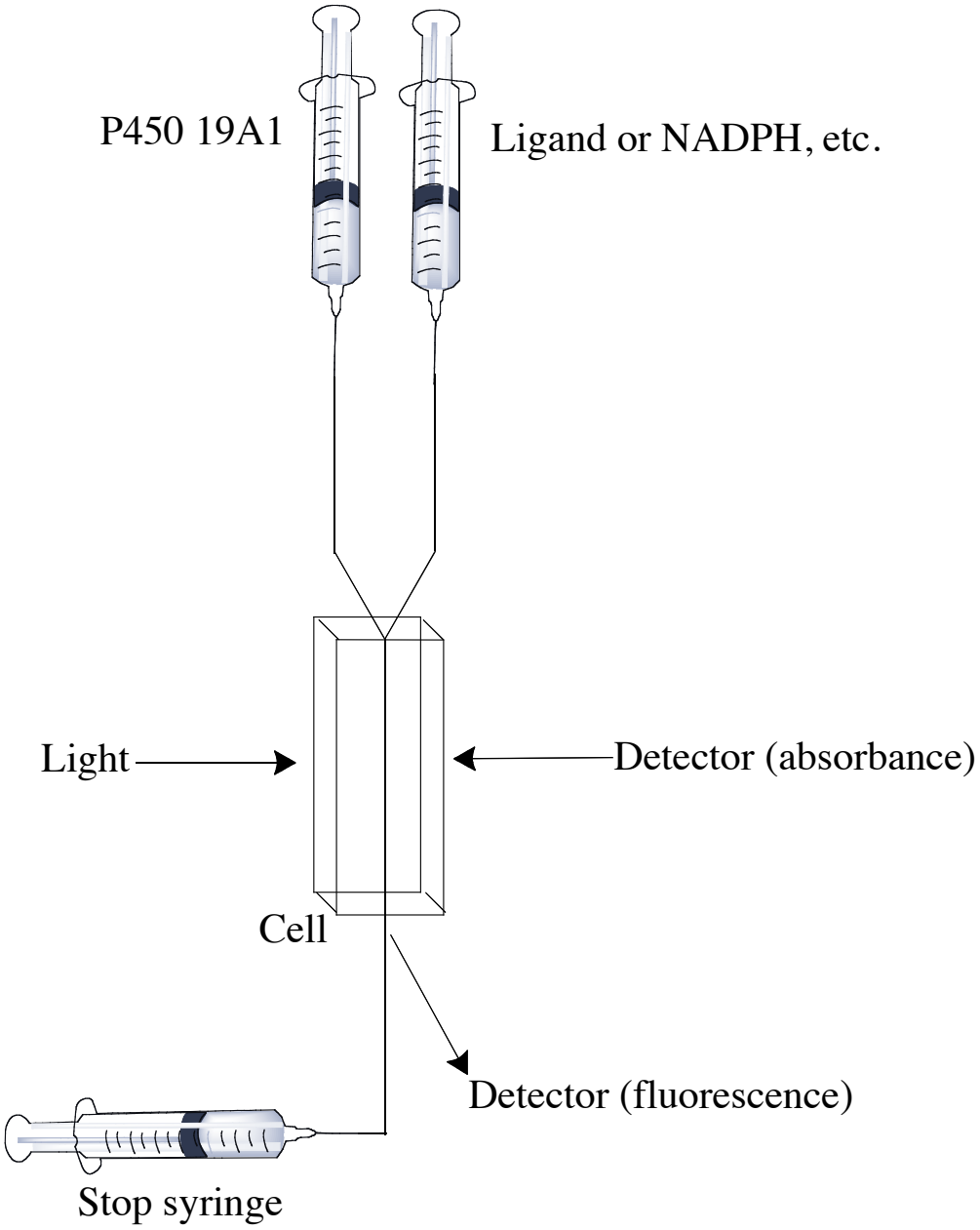

Figure 8. Stopped-flow spectrophotometer. The components of two syringes are mixed in the cell, where spectral changes are observed until pushed into a stop syringe.

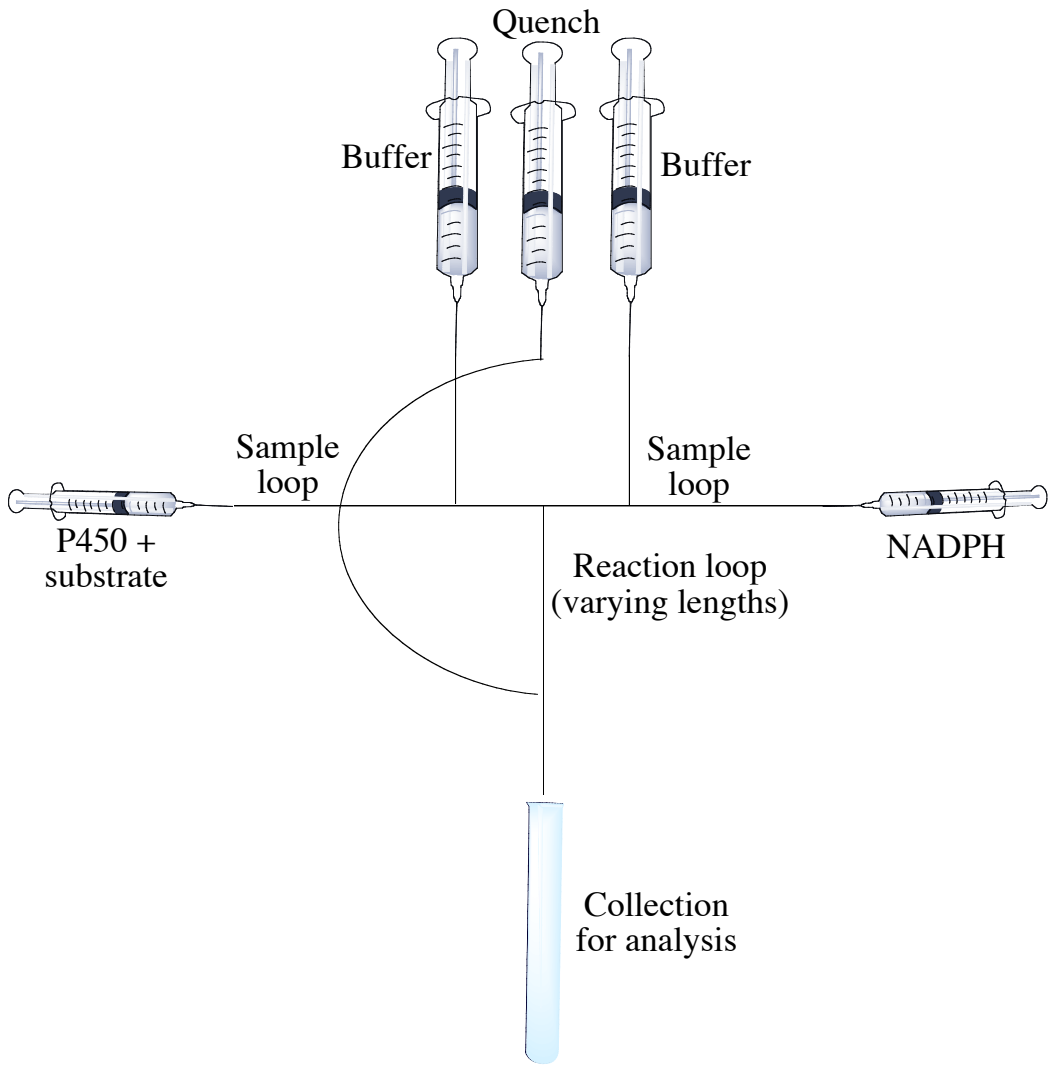

Figure 9. Rapid chemical-quench apparatus. Enzyme and NADPH are pushed through the sample loops into the reaction loop (varying lengths to give varying reaction times) by the buffer syringes. The reaction is terminated by contact with the contents of the quench syringe, and the mixture is pushed into the collection tube for analysis.

are typically separated by radio-HPLC to determine the relative concentrations of the substrate, intermediate(s), and product(s) over time.

Typically reactions are done under single turnover conditions, in which the concentrations of substrate and enzyme are equal, or under burst conditions, in which the substrate is present at a much higher concentration than enzyme. An observed burst comes from a faster initial rate followed by a slower rate and implies that product release defines at least in part the overall rate (i.e. rate-limiting step). The amplitude of the burst also reveals important information on the initial concentration of enzyme containing bound substrate. Nearly ten-fold less total volume per reaction is used in rapid chemical-quench experiments than in those using the stopped-flow spectrophotometer, although the point should be made that a single stopped-flow trace can produce an entire kinetic course.

Rate constants result from fitting the data from these pre-steady-state studies using mathematical equations. More rigorous fitting methods include global fitting, in which several types of kinetic data are fit concurrently in order to constrain the calculated rate constants. For these and other types of more complicated types of fits, software such as DynaFit (44) or Kintek Explorer® (45) are used rather than relatively simple exponential equations. In the case of DynaFit, text scripts are written that include a mechanism (e.g. E + A ⇆ EA) and then a combination of experimentally derived rate constants and rate constants to be determined by the fitting process (the latter are inserted into the script as a reasonable guess for a rate followed by "?"). After uploading the data to be fit and the script, reiterations of the program are run to generate a series of differential equations based on the given rate constants. These unknown constants are

modified (or "floated") in subsequent scripts until the best fit (that which best describes the raw data and makes scientific sense) is achieved. For Kintek Explorer®, the raw data is uploaded and a mechanism is again developed. Results of changing the individual rate constants can be observed in real-time, as the fit is instantaneously modulated. Examples of both DynaFit scripts and raw Kintek Explorer® output can be found in the Appendix. Both software systems are powerful tools for understanding complicated kinetics: DynaFit particularly for the kinds of data it can process, and Kintek Explorer® for its rapid output.

In this work, steady-state incubations using the model membrane vesicles were performed with various substrate concentrations to yield *v vs*. substrate concentration plots. Fitting these plots to equations allows the extraction of k_{cat} and K_m (steady-state) parameters. A stopped-flow spectrophotometer was used to examine rates associated with ligand binding and iron reduction (Figure 4). As mentioned, Type I changes are typically associated with substrate (and, often, intermediate and product) binding. Measuring these changes under pre-steady-state time frames using stopped-flow spectroscopy yielded the rate constants associated with ligand binding, which are expected to be diffusion controlled (46). Pulse-chase assays were performed to determine the extent of processivity in P450 19A1 turnover. A rapid chemical-quench was used to generate a progress curve under single turnover conditions showing the change in substrate, intermediates, and product over time.

Research Aims

A unifying theme in this work is the kinetic characterization of the multi-step turnover of reactions catalyzed by P450s 1A2 and 19A1, despite the very different types of substrates preferred (exogenous compounds, typically polycyclic aromatic hydrocarbons for P450 1A2, and androgens for P450 19A1). While pre-steady-state analyses of P450 11B2 (35) and 17A1 (36) have been reported, no global fits (i.e. using several types of data to generate a kinetic mechanism of turnover) are available for sequential P450s that utilize endogenous substrates. Classifying P450 19A1 as a processive or distributive enzyme is an important consideration in elucidating sequential enzyme kinetics.

Prior work in this laboratory on rabbit P450 1A2 indicated, for the first time, cooperativity associated with several 1-alkoxy-4-nitrobenzene substrates and $Ph(NC)_2$ (47). Homotropic negative cooperativity, in which binding of a second substrate molecule inhibits the rate of catalysis, was seen for the dealkylation of $(CH_3)_2CH\text{-}O\text{-}PhNO_2$ by P450 1A2. When $Ph(NC)_2$ was added, heterotropic positive cooperativity was observed with regard to substrate binding, meaning that rates of substrate binding are enhanced upon the addition of a non-substrate ligand. P450 1A2 has a major role in detoxication of pollutants, and to a lesser extent, clearance of drugs, and is induced by cigarette smoke and charred meat. As this was the first evidence of cooperativity with P450 1A2 at this time, it was important to determine if this phenomenon was limited to this small substrate class because evidence of cooperativity can affect drug dosing, exposure limits, etc.

Past work by Dr. Emre Isin in 2005-2006 in this laboratory focused on binding of two fluorescent compounds, αNF and pyrene, to rabbit P450 1A2 using stopped-flow

fluorescent spectroscopy. Using similar techniques, Dr. Isin was also able to show that pyrene formed excimers, or dimers in an excited electronic state, both in solution and in the presence of rabbit P450 1A2. While it was known αNF inhibits P450 1A2 (48), no studies had been undertaken to determine if these compounds were also substrates.

Because a reliable two-column method for the purification of P450 1A2 from rabbit liver from β-naphthoflavone-treated rabbits had already been developed (49), the goals of this project were to determine if pyrene and αNF were substrates for rabbit P450 1A2, and, if so, the reaction indicated any cooperative behavior (i.e. binding of one substrate molecule enhanced the rate of oxidation of a second, *vide infra*). A crystal structure for human P450 1A2 (23) in the presence αNF was available (Figure 1), so the potential existed to use structural modeling to rationalize any observed differences in cooperativity among these potential substrates. Further, due to the spectroscopic properties of these substrates as well as P450 1A2, both pre-steady-state and steady-state kinetic technique could be used to determine individual rate constants and dissociation constants of ligand binding. Global fitting of these different types of data could be used to generate a minimal kinetic model of P450 1A2 turnover with novel substrates.

In order to characterize P450 19A1 kinetically, a reliable method of heterologous expression and purification was first required. Most published work cites purification of P450 19A1 from placenta, which relies on access to human tissues and precludes mutagenesis experiments (24, 50-53). Chromatography steps also consist of two to four columns, (51, 54-56) (some of which utilize monoclonal antibodies) which can be time-consuming and sacrifice overall protein yields. Other protocols require the use of non-ionic detergents, which can be difficult to remove (57) or the use of substrates or

inhibitors that stabilize the protein during purification (51, 55) but are detrimental to kinetic studies if not removed. For heterologous expression, baculovirus-infected insect cells have been used (58, 59), which are more costly and time-consuming to maintain. Expression in *Escherichia coli* has been reported (60-62), but have lower levels of expression, require multiple columns for purification, and/or rely on stabilizing ligands as cited above. A clear need exists for a consistent, robust protocol for the heterologous expression and purification of active P450 19A1 from *E. coli*.

Following development of a reliable expression and purification method of P450 19A1, the intention was to characterize the enzyme kinetically. While several steady-state parameters (primarily k_{cat} and K_m values for estrone and 17β-estradiol formation from andro and testosterone, respectively, including (50-53)) exist, pre-steady-state experiments have not been conducted to determine the individual rate constants for the steps of P450 19A1 turnover. Such an extensive kinetic characterization can be achieved by measuring the rates of binding of substrate, intermediates, and product to P450 19A1, determining the rates of reduction of iron in the presence of these ligands, and monitoring the concentrations of each ligand in a single turnover experiment. Steady-state work would be expanded to include k_{cat} and K_m values for conversion of the two intermediates to estrone in addition to the well-characterized conversion of andro to estrone. As discussed in detail (*vide supra*), pulse-chase experiments can be used to determine the degree of processivity of P450 19A1 turnover. Combining several types of steady-state and pre-steady-state data using global kinetic fitting software allows the generation of the first minimum kinetic model to describe overall turnover of P450 19A1. Such an in-depth kinetic analysis can be beneficial in the design of novel aromatase inhibitors.

CHAPTER II

COOPERATIVITY IN OXIDATION REACTIONS CATALYZED BY CYTOCHROME P450 1A2: HIGHLY COOPERATIVE PYRENE HYDROXYLATION AND MULTIPHASIC KINETICS OF LIGAND BINDING[1]

Introduction

Most reactions catalyzed by P450s can be described with hyperbolic, classical Michaelis-Menten kinetics. However, examples of heterotropic cooperativity (i.e., one ligand enhancing the rate of oxidation of another (63)) were reported in the 1970s (64-67), and in the early 1990s reports of homotropic cooperativity (e.g. sigmoidal and other atypical *v vs*. substrate concentration plots (63) began to appear (68, 69). Examples of *in vivo* evidence for heterotropic cooperativity are known (70, 71). Homotropic cooperativity is difficult to demonstrate *in vivo* but the process can be documented in isolated hepatocytes (72).

Explanations and hypotheses have been presented for (human) P450 3A4, perhaps the most commonly reported example of P450 cooperativity, and also for other P450s for which cooperative behavior has been reported, particularly (human) P450s 2C8, 2C9, 2B6, and 1A2 (73-77). Most of these P450s that have been crystallized have large cavities for ligand binding (78-80). Some of the major features of the more common proposals to explain cooperativity include: (i) a classic allosteric reaction with a second

[1] This project, including manuscript writing, was done in collaboration with Drs. Emre M. Isin, Robert L. Eoff, Glenn A. Marsch, Donald F. Stec, and F. Peter Guengerich.

ligand binding site controlling binding to the catalytic substrate binding site (81, 82); (ii) co-occupancy of the cognate substrate binding site with multiple ligands, leading to a more productive rearrangement of the substrate for catalysis due to either steric packing or more specific protein-ligand interactions (69, 83, 84); (iii) selective populations of P450 (in slow equilibrium) that interact in different ways (85); (iv) multimeric states of P450 (86) and possibly interactions with accessory proteins (87) that are involved; and (v) elements of an induced fit process, in which the protein adapts a conformation as a result of an initial interaction with a ligand (88). Some of these possibilities are not mutually exclusive. Deficiencies in this area are the small extent of cooperativity seen in many cases (i.e., low *n* values in Hill plots), the often limited number of experimental data points, and the over-interpretation of models based on limited data.

P450 1A2 is an important enzyme, not so much in regard to physiological function per se but because of its role in the oxidation of many drugs (89) and carcinogens, particularly aryl and heterocyclic amines (90). A recent crystal structure of the protein bound to the inhibitor αNF provides insight into how this protein binds substrates (23). The active site is somewhat larger than necessary for the ligand αNF to fit, but the accessible volume is considerably less than that available in other mammalian P450s, e.g. 2C8, 2C9, and 3A4 (78-80). P450 1A2 also exhibits cooperativity in some reactions, at least with regard to homotropic behavior. In the case of *O*-dealkylation of $(CH_3)_2CH$-O-$PhNO_2$, rabbit P450 1A2 showed patterns that could be described mathematically as negative cooperativity (47). However, a more appropriate fit of the results involves two sets of k_{cat} and K_m values. Evidence that these phenomena are the result of concurrent occupancy of P450 1A2 by two ligands comes from a study with two

ligands, a $(CH_3)_2CH$-O-$PhNO_2$ substrate and the iron ligand $Ph(NC)_2$, which elicits a heme spectral perturbation opposite to that of the Type I substrate, i.e. a Type II change involving an increase in A_{420} and decrease in A_{390}. A key finding was that the extrapolated K_d values for P450 1A2 binding of $(CH_3)_2CH$-O-$PhNO_2$ were perturbed when measured in the presence of $Ph(NC)_2$ and vice versa (47). However, these studies did not reveal details of the mode of interaction.

One approach this laboratory has utilized to study the cooperativity of P450 3A4 is time-resolved analysis of events in ligand binding, i.e. kinetic studies (91, 92). These studies have revealed complex, multiphasic, and slow events that are considered relevant to issues in cooperativity, and evidence has been presented that these events have their basis in sequential as opposed to parallel events (91, 92). These complex events are not seen in the binding of ligands to "simpler" mammalian P450s, e.g. P450 2A6 (93), or bacterial P450 101A1 (94) or P450 105D5 (95).

In this chapter, the cooperative nature of some substrates oxidized by P450 1A2 was studied. It was hypothesized that cooperativity in catalysis by P450 1A2 is not limited to a small class of substrates (1-alkoxy-4-nitrobenzenes), and instead may include important chemicals such as drugs and pollutants. Further it was hypothesized that such cooperative behavior may have a structural basis in that it depends on the ability of more than one substrate molecule to bind in the active site to exert cooperative effects. Rabbit P450 1A2 was used because its heme spectral properties permit a number of studies that cannot be done with the human ortholog, which is isolated exclusively in the high-spin iron state in the absence of any ligand (47, 96). A very strong positive cooperativity pattern was found for the oxidation of pyrene, unprecedented in P450 literature. Pyrene

also proved to be a very useful ligand because of its fluorescence properties. Pre-steady-state kinetic analyses were done using UV-visible, fluorescence, and CD spectroscopy and comparisons were made with αNF (a substrate that does not show apparent cooperativity). The availability of the crystal structure of a human P450 1A2-αNF complex provided a basis for modeling ligands in rabbit P450 1A2, which may be relevant to cooperative phenomena.

Experimental Procedures

Chemicals—αNF, pyrene, 1-OH pyrene, and luminescence grade solvents for fluorescence studies were purchased from Sigma-Aldrich (Milwaukee, WI). Pyrene was recrystallized from C_2H_5OH before use. $(CH_3)_2CH$-O-$PhNO_2$ was synthesized as described previously (47).

Enzymes—P450 1A2 was purified from liver microsomes prepared from β-naphthoflavone-treated New Zealand White rabbits using a two-step ion-exchange chromatography procedure (49), as modified (96). The preparations used in the work contained < 13% cytochrome P420, an inactive form. NADPH-P450 reductase (rat) was expressed in *E. coli* and purified as described elsewhere (97).

Measurement of Enzyme Activity—Substrates were incubated with a reconstituted enzyme system that generally included 0.25 μM P450 1A2, 0.50 μM NADPH-P450 reductase, 23 μM L-α-1,2-dilauroyl-*sn*-glycero-3-phosphocholine (dispersed by

sonication before use, as a 1 mg/ml stock solution), and the substrate of interest, generally in a reaction volume of 1.5 ml. All incubations were in 100 mM potassium phosphate buffer (pH 7.4) (the enzyme precipitates at lower ionic strength). Stock concentrations of substrates were prepared in CH_3OH, and the final concentration of CH_3OH in reactions was ≤ 1% (v/v). The reported solubility of pyrene in H_2O is 0.65 μM (98). The solubility under the experimental conditions used here is probably higher, with a 1% (v/v) concentration of organic solvent (and dispersion in some cases with the phospholipid vesicles and possibly the proteins). Catalytic studies with polycyclic aromatic hydrocarbons, including pyrene and particularly benzo[*a*]pyrene, have often been done at relatively high concentrations (50-80 μM (99-102)). However, the concentration is typically limited in the spectroscopic experiments to a low μM range to avoid artifacts.

Incubations (in a shaking water bath, 37 °C, 50 rpm shaking; Amerex Instruments model 903, Lafayette, CA) were initiated by the addition of an NADPH-generating system (101) and run for 2 min (pyrene), 1.5 min (1-OH pyrene), or 20 min (αNF). Reactions were stopped by the addition of 2.0 ml CH_2Cl_2 and mixed with a vortex device, and 1.5 ml of the organic layer was removed and dried under an N_2 stream for HPLC analysis.

αNF reaction products were dissolved in CH_3OH and separated by HPLC using an octadecylsilane (C_{18}) column (6.2 mm × 80 mm, 3 μm, Agilent Technologies, Palo Alto, CA). The following program was used at a flow rate of 1.0 ml min^{-1} (solvent A: 50% H_2O, 10 mM potassium phosphate buffer (pH 7.4), 50% CH_3OH; solvent B: 100% CH_3OH): 0-4 min: linear gradient from 0-100% B, 4-10 min: 100% B (isocratic).

Separations were monitored by scanning from 290 to 400 nm using a ThermoFinnigan UV3000 rapid-scanning UV detector (ThermoFisher Scientific, Waltham, MA). P450 3A4 has been shown previously to oxidize αNF only to the 5,6-oxide (84). P450 3A4/NADPH-P450 reductase-containing bacterial membranes (103) were incubated with αNF and prepared for HPLC analysis under identical conditions as the P450 1A2 reactions. One dominant product was observed after αNF oxidation by P450 1A2, which had the same t_R and UV spectrum as the 5,6-epoxide product resulting from P450 3A4 oxidation. Quantification of product formation was estimated using the extinction coefficient of αNF (ε_{290} 23.7 mM^{-1} cm^{-1}) (104).

Pyrene and 1-OH pyrene reaction products were dissolved in CH_3OH and separated by HPLC using the following program at a flow rate of 1.0 ml min^{-1} (solvent A, 90% 10 mM $NH_4CH_3CO_2$ buffer (pH 6.8)/10% CH_3OH (v/v); solvent B, 100% CH_3OH): 0-20 min: linear gradient from 45% to 80% B; 20-21 min: linear gradient to 100% B; 21-25 min: 100% B (isocratic). Separation of products was monitored using a McPherson FL-750 BX fluorescence detector (Chelmsford, MA), with excitation at 240 nm and emission monitored using a > 380 nm long pass filter, as well as by UV scanning (UV3000 detector, *vide supra*, in series) from 230 to 400 nm (105). After the relevant spectra had been accumulated, individual wavelength traces were used subsequently.

Benzo[*a*]pyrene hydroxylation assays, in which mainly 3-hydroxylation is measured, were done using the basic fluorescence extraction method of Nebert and Gelboin (99), with slight modification (101). 3-Hydroxybenzo[*a*]pyrene (Midwest Research Laboratories, Kansas City, MO) was used as a standard, with standardization of the stock solution using an extinction coefficient from Raha (106).

Characterization of Di-OH Pyrene Products—An enzyme system of 0.25 μM P450 1A2, 0.50 μM NADPH-P450 reductase, phospholipid (*vide supra*), and 50 μM 1-OH pyrene (total volume 285 ml) was incubated for 10 min under the same conditions as described above and the products were extracted. HPLC conditions were altered slightly; the following program was used with a flow rate of 1.0 ml min^{-1}: (solvent A, 90% H_2O/10% CH_3OH (v/v); solvent B, 100% CH_3OH): 0-30 min: linear gradient from 45% to 70% B. Seven sequential HPLC injections (20 μl each) were made, and the four product fractions (peaks 1-4) were collected, based on monitoring by UV at 275 nm (Figure 10*A*). The fractions from each injection were combined, extracted with CH_2Cl_2, and first dried using a rotary evaporator and then under an N_2 stream. The four fractions were further dried *in vacuo*, using a vacuum pump, in a dessicator with P_2O_5 for 5 h at room temperature. Each sample was then dissolved in d_6-acetone and transferred to a 2.5 mm NMR tube under an argon atmosphere for NMR spectroscopy analysis, where 1-dimensional, COSY, HSQC, and HMBC ^1H (^{13}C) NMR spectra were obtained. Peaks 1 and 4 were then spiked with 60 nmol of CH_3CO_2H as an internal standard in d_6-acetone; 300 nmol of CH_3CO_2H was added to peaks 2 and 3. The integration of the resulting singlet at 1.96 ppm was set at H = 3 to allow quantitation of the di-OH pyrenes. The fluorescence emission spectrum of each of the fractions was recorded in the NMR solvent (excitation at 240 nm). The fractions were then dried and dissolved in CH_3OH, and the absorbance spectra (200-600 nm) were recorded.

Anaerobic Experiments—Samples were deaerated in all-glass cuvettes or tonometers using a vacuum/argon manifold system and a glucose oxidase-catalase-

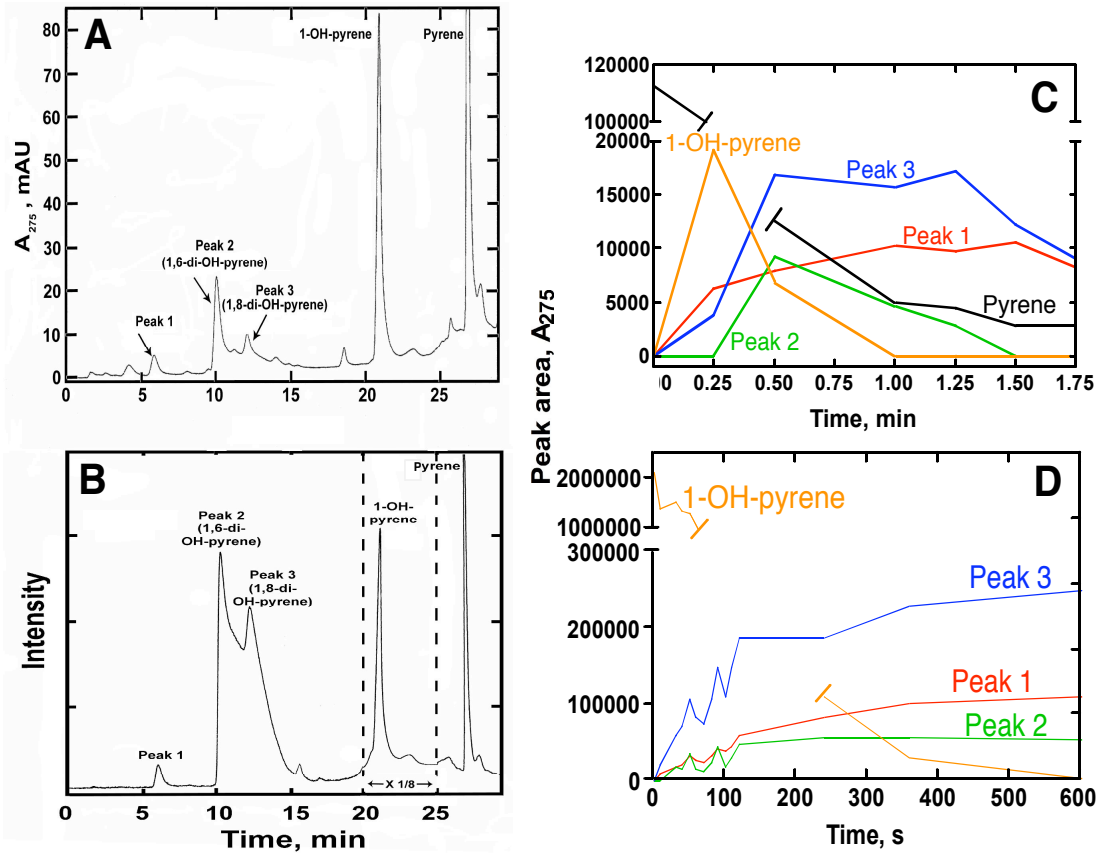

Figure 10. Time courses and chromatograms of the oxidation of pyrene by P450 1A2. *A*, HPLC of products, A_{275} trace (reaction with 10 μM pyrene, 0.25 μM P450, 10 min). *B*, HPLC of products, fluorescence trace (excitation 240 nm, emission filter > 380 nm) (same enzyme system as in Part *A*). *C*, Time course of product formation from pyrene (1 μM starting concentration). *D*, Time course of product formation from 1-OH pyrene (10 μM starting concentration).

glucose enzymatic scrubbing system as described earlier (107) and modified (108). Contents of tonometers were transferred into the drive syringes of the stopped-flow spectrophotometer as described (108). Anaerobic titrations were done in a glass cuvette/titrator assembly using techniques previously described (109).

Spectroscopy—UV-visible spectra were recorded with a Cary14/OLIS, an Aminco DW2/OLIS, or a Hewlett Packard 8452A/OLIS diode array spectrophotometer (On-Line Instrument Systems, Bogart, GA). Steady-state spectral titrations of ferric P450 1A2 with αNF and pyrene were carried out as described previously (43). In the case of the 1-OH pyrene titrations, a different procedure was used because of the inherent absorbance of the ligand in the near-UV region. In this case, tandem (Yankeelov) cuvettes were used. At each concentration of 1-OH pyrene, each of two cuvettes contained 1.0 ml of 2.0 μM P450 1A2 in one chamber and twice the desired final concentration of 1-OH pyrene in the other side. A baseline spectrum was recorded in the OLIS-Cary 14 spectrophotometer (mean of duplicate scans). The contents of the two chambers of the sample cuvette were then mixed; the reference cuvette was not mixed. The resulting difference spectrum was recorded (mean of duplicate scans).

Fluorescence spectra were recorded with either an OLIS DM-45 (On-Line Instrument Systems) or a Fluorolog-3 spectrofluorometer in the 111 configuration (JY Horiba, Edison, NJ). Steady-state fluorescence spectra were acquired at 25 °C, with slit widths at a 1-3 nm bandpass, depending on fluorophore concentration. Either CH_3OH or luminescence grade propanol was used to dissolve ligands. For the steady-state titration

experiments, either the emission (at a fixed wavelength) or the excitation (at a fixed emission wavelength) scans were recorded.

CD spectra were recorded in 1 mm cuvettes with a JASCO J-810 instrument (Easton, MD) in the Vanderbilt Center for Structural Biology. In the case of the CD scans, P450 1A2 was incubated with substrate for 15 min before taking measurements; kinetic scans were initiated as soon as substrate was added. The absorbance in all CD studies was < 0.20. CD output, in mdeg, was converted to standard mean residue ellipticity, $[\theta]$ (in deg cm^2 $dmol^{-1}$), using the relationship

$$[\theta] = \frac{100(signal)}{cnl}$$

where *signal* is the CD output in mdeg, *c* is the protein concentration in mM, *n* is the number of amino acid residues, and *l* is the cell path length in cm.

Stopped-flow absorbance and fluorescence kinetic measurements were made using an OLIS RSM-1000 instrument (On-Line Instrument Systems) as described in detail previously (92). Absorbance (UV-visible) measurements were made in the rapid-scanning mode (scanning 10^3 spectra s^{-1}); kinetic parameters were derived from traces of absorbance (*vs*. time) at individual wavelengths and fit to single, bi-, or tri-exponential equations using the manufacturer's software. Kinetic fluorescence measurements were made with the OLIS RSM-1000 instrument using long pass or bandpass filters (Oriel, Stratford, CT) attached to the photomultiplier tube and utilized a direct kinetic mode, with fitting of data as described for absorbance. In most cases, 1.24 mm slits (8 nm

bandwidth) were used. Data are presented as either "scatter" plots or "connected" signals *vs*. time. Generally, four to eight individual stopped-flow experiments were averaged.

Mass and NMR Spectrometry—LC-MS-MS spectra were acquired using an Acquity UPLC system (Waters, Milford, MA) with the same octadecylsilane (C_{18}) column (6.2 mm × 80 mm, 3 μm) as described (*vide supra*) connected to a Finnigan LTQ mass spectrometer (ThermoFisher Scientific, Waltham, MA) and operated in the ESI negative ion mode. Reaction products were dissolved in CH_3OH and kept at 4 °C prior to injection with an autosampler, while the column was kept at ambient temperature. In addition to an ion scan from *m/z* 100-500, two selective ion monitoring scans at *m/z* 217 and 233 were taken which triggered MS-MS fragmentation events. Product ion MS-MS scans were acquired from *m/z* 100-300. The following LC conditions were used, with a 375 μl min^{-1} flow rate (solvent A, 90% 10 mM $NH_4CH_3CO_2$ buffer (pH 6.8)/10% CH_3OH (v/v); solvent B, 100% CH_3OH): 0-30 min: linear gradient from 45-100% B. ESI conditions were as follows: source voltage 4 kV, source current 100 µA, auxiliary gas flow rate setting 20, sweep gas flow rate setting 5, sheath gas flow setting 34, capillary voltage –26 V, capillary temperature 350 °C, tube lens voltage –138 V. MS-MS conditions were as follows: normalized collision energy 35%, activation Q setting 0.250, and activation time 30 ms.

NMR experiments were acquired using either a 14.0 T Bruker magnet (Bruker, Billerica, MA) equipped with a Bruker AV-II console operating at 600.13 MHz in the case of peaks 2, 3, and 4 or an 11.7 T Bruker magnet equipped with a Bruker DRX console operating at 500.13 MHz in the case of peak 1. All spectra were acquired in 2.5 mm NMR tubes using a Bruker 5 mm TCI cryogenically cooled NMR probe. Chemical

shifts were referenced internally to acetone (7.1 ppm) that also served as the ^{2}H lock solvent. For 1-dimensional ^{1}H NMR, typical experimental conditions included 32K data points, 13 ppm sweep width, a recycle delay of 1.5 s, and 128-512 scans, depending on sample concentration. For 2-dimensional ^{1}H-^{1}H COSY spectra, experimental conditions included 2048 × 512 data matrix, 13 ppm sweep width, recycle delay of 1.5 s, and 32 scans per increment. The data was processed using a squared sinebell window function, symmetrized, and displayed in magnitude mode. Multiplicity-edited HSQC experiments were acquired using a 1024 × 256 data matrix, a $J^{(C-H)}$ value of 145 Hz which resulted in a multiplicity selection delay of 34 ms, a recycle delay of 1.5 s, and 24 scans per increment, along with GARP decoupling on ^{13}C during the acquisition time (150 ms). The data was processed using a π/2 shifted squared sine window function and displayed with CH/CH_3 signals phased positive and CH_2 signals phased negative. $J_1^{(C-H)}$ filtered HMBC experiments were acquired using a 2048 × 256 data matrix, a J(C-H) value of 9 Hz for detection of long range couplings resulting in an evolution delay of 55 ms, $J_1^{(C-H)}$ filter delay of 145 Hz (34 ms) for the suppression of one-bond couplings, a recycle delay of 1.5 s, and 96 scans per increment. The HMBC data were processed using a π/2 shifted squared sine window function and displayed in magnitude mode.

Analysis of Kinetic and Binding Data—Pre-steady-state data were initially fit to exponential equations using the OLIS software. In some cases binding rate measurements were made at several ligand concentrations and fit to plots of rate *vs*. ligand concentration to estimate k_{on} and k_{off} values. For complex fits, the program DynaFit (44) was used to fit

data to possible mechanisms. Steady-state kinetic data were fit to hyperbolic or sigmoidal plots, which in the latter case developed as a Hill plot of the form

$$v = \frac{k_{cat} \cdot [S]^n}{S_{50}^n + [S]^n}$$

where S denotes substrate and *n* is an exponent used for fitting but has no direct physical meaning. Fitting was done with the program GraphPad Prism (GraphPad, San Diego, CA). The DynaFit program was also utilized with sigmoidal steady-state kinetics. Some of the ligand binding data were fit to the quadratic equation Y = B + (A/2)(1/E) $[(K_d$+E+X)- $((K_d$+E+X)^2-(4EX))$^{1/2}]$ in GraphPad Prism, with B being the intercept, A the maximum change, E the enzyme concentration, and X the ligand concentration (the form used in the program was Y = B + (A/2)*(1/E)((Kd+E+X)-sqrt((Kd+E+X)^2-(4*E*X))).

Homology Modeling and Docking— A recently published crystal structure of a human P450 1A2-αNF complex (23) was used as the template to develop a homology model of rabbit P450 1A2 using the SWISS-MODEL automated homology modeling tool (110). Coordinate files for molecules of pyrene were generated using the Dundee PRODRG2 server (111) and manually docked into the binding cavity (replacing αNF) using Turbo Frodo (112). Simulated annealing was then performed in CNS Solve 1.1 using the input file model anneal (113, 114). The heme group was fixed during simulated annealing. The energy-minimized models were not adjusted following annealing.

Results

Characterization of Oxidation Products of αNF and Pyrene—Although αNF is generally considered an inhibitor of P450 family 1 enzymes (48, 64), it was found to be slowly oxidized by rabbit P450 1A2. The only product detected using HPLC was the 5,6-epoxide (partly recovered as the 5,6-dihydrodiol (100)), which was identified by t_R and UV comparison with the product isolated from reactions with P450 3A4 (previously established by NMR methods) (84).[2]

Oxidation of another fluorescent substrate, pyrene, yielded five (fluorescent) products (Figures 10*A* and 10*B*). 1-OH pyrene was identified by co-chromatography and its identical UV and mass spectra compared with commercial material. The time course of the products (Figure 10*C*) suggested that peaks 1, 2, and 3 might be products of 1-OH pyrene, and an experiment using 1-OH pyrene as substrate confirmed this hypothesis (Figure 10*D*).

MS established that the other four products were di-OH pyrenes (Figure 11). A reaction with a limited pyrene concentration indicated a rise-fall relationship for 1-OH pyrene, supporting its role as an intermediate product (Figure 10*C*). 1-OH pyrene was converted to all of these (Figures 10*B* and 10*D*). UV and fluorescence spectra were also recorded (Figures 12 and 13). NMR experiments (Figure 14) were used to identify the sites of pyrene hydroxylation (Figure 15). The last of the four eluted peaks (Peak 4) was obtained in trace amounts, contaminated with Peak 3, and the structure was not identified.

[2] This laboratory previously reported the 5,6-epoxidation of αNF by recombinant human P450 1A1 and 1A2, although the reaction was not examined at multiple substrate concentrations (100).

Figure 11. Characterization of di-OH pyrenes: mass spectra. *A*, Peak 1. *B*, Peak 2. *C*, Peak 3. *D*, Peak 4.

A

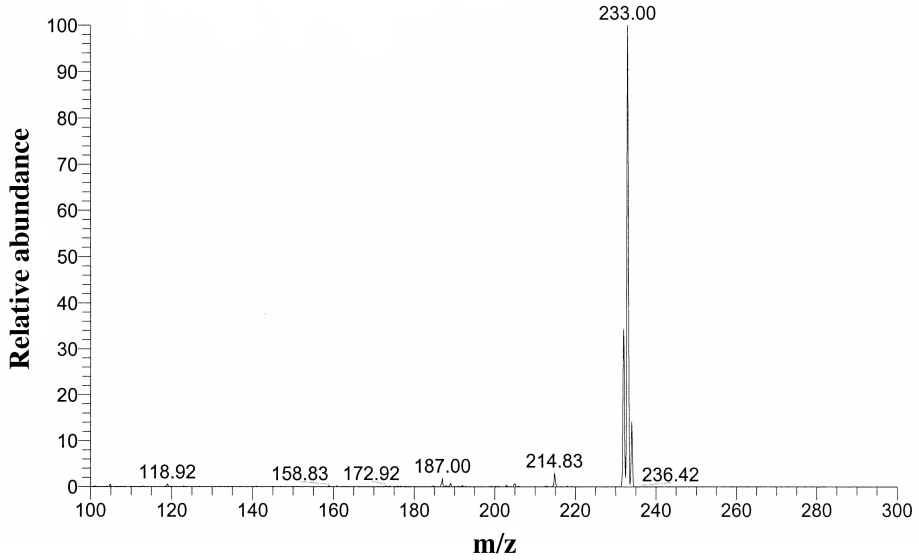
233.00
Relative abundance
100
90
80
70
60
50
40
30
20
10
0
118.92
158.83
172.92
187.00
214.83
236.42
100
120
140
160
180
200
220
240
260
280
300
m/z

B

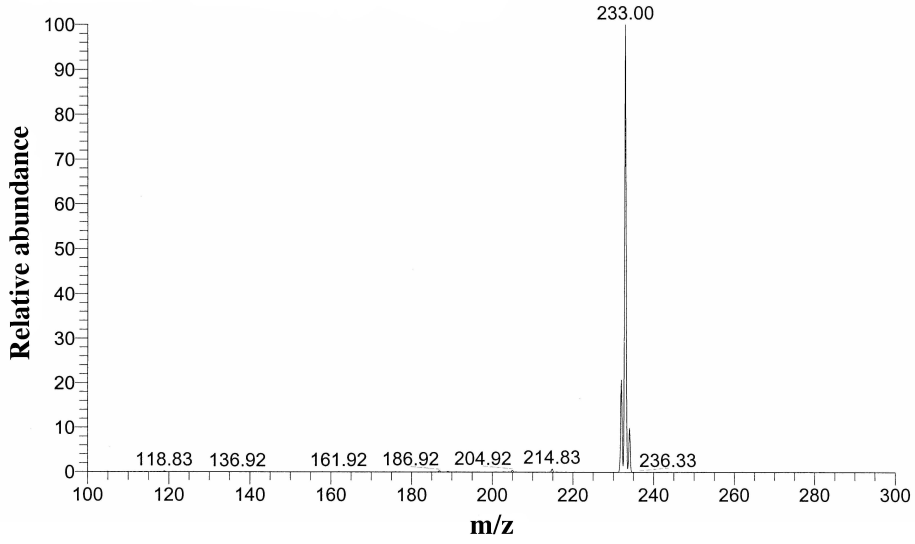
233.00
Relative abundance
100
90
80
70
60
50
40
30
20
10
0
118.83
136.92
161.92
186.92
204.92
214.83
236.33
100
120
140
160
180
200
220
240
260
280
300
m/z

C

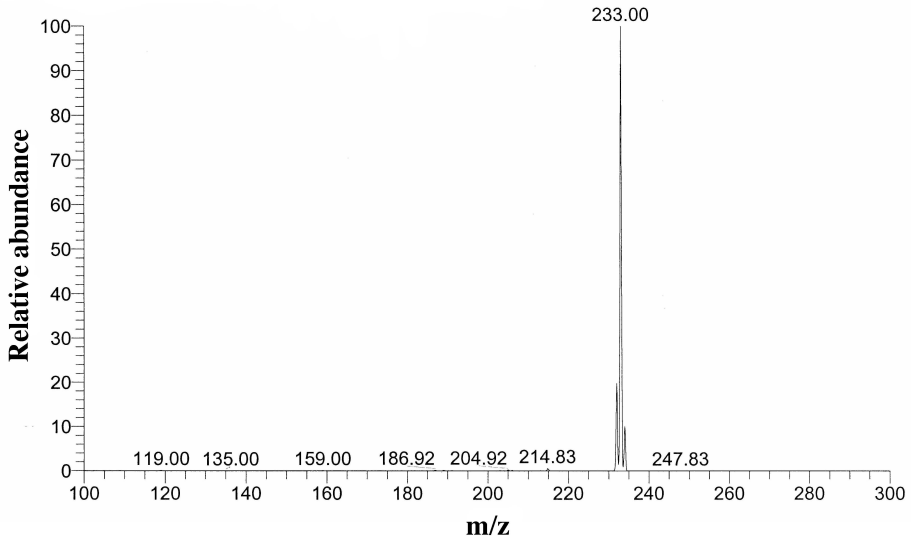
233.00
Relative abundance
119.00
135.00
159.00
186.92
204.92
214.83
247.83
m/z

D

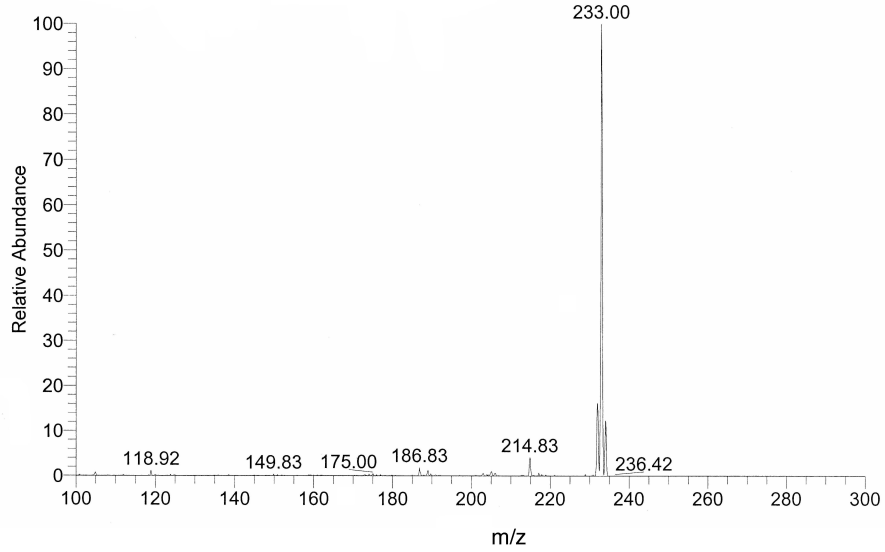
233.00
Relative Abundance
118.92
149.83
175.00
186.83
214.83
236.42
m/z

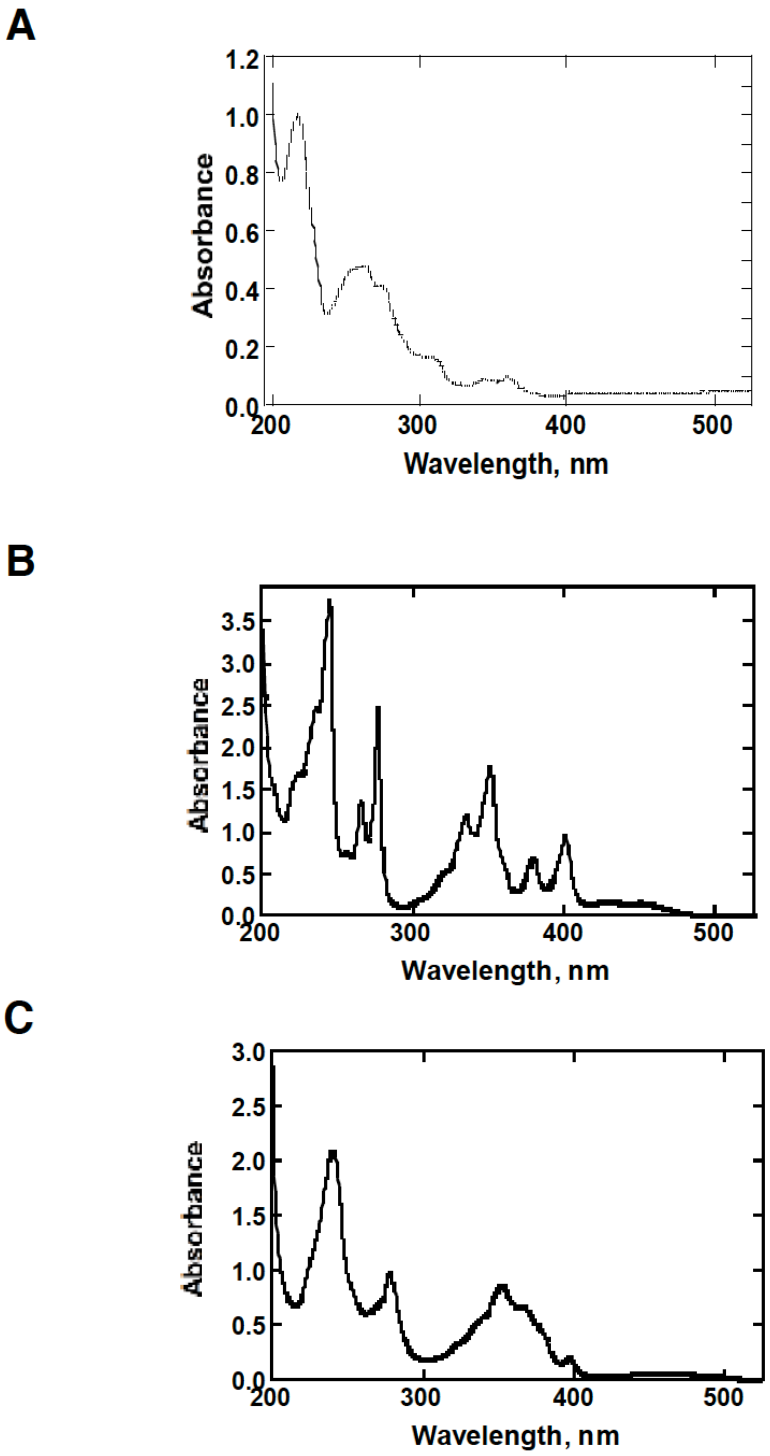

Figure 12. Characterization of di-OH pyrenes: UV spectra. *A*, Peak 1, assigned as 1,5 di-OH pyrene. *B*, Peak 2, 1,6 di-OH pyrene. *C*, Peak 3, 1,8 di-OH pyrene. The spectra were recorded in CH_3OH with an OLIS-Cary 14 instrument and are accurate at the absorbance values indicated.

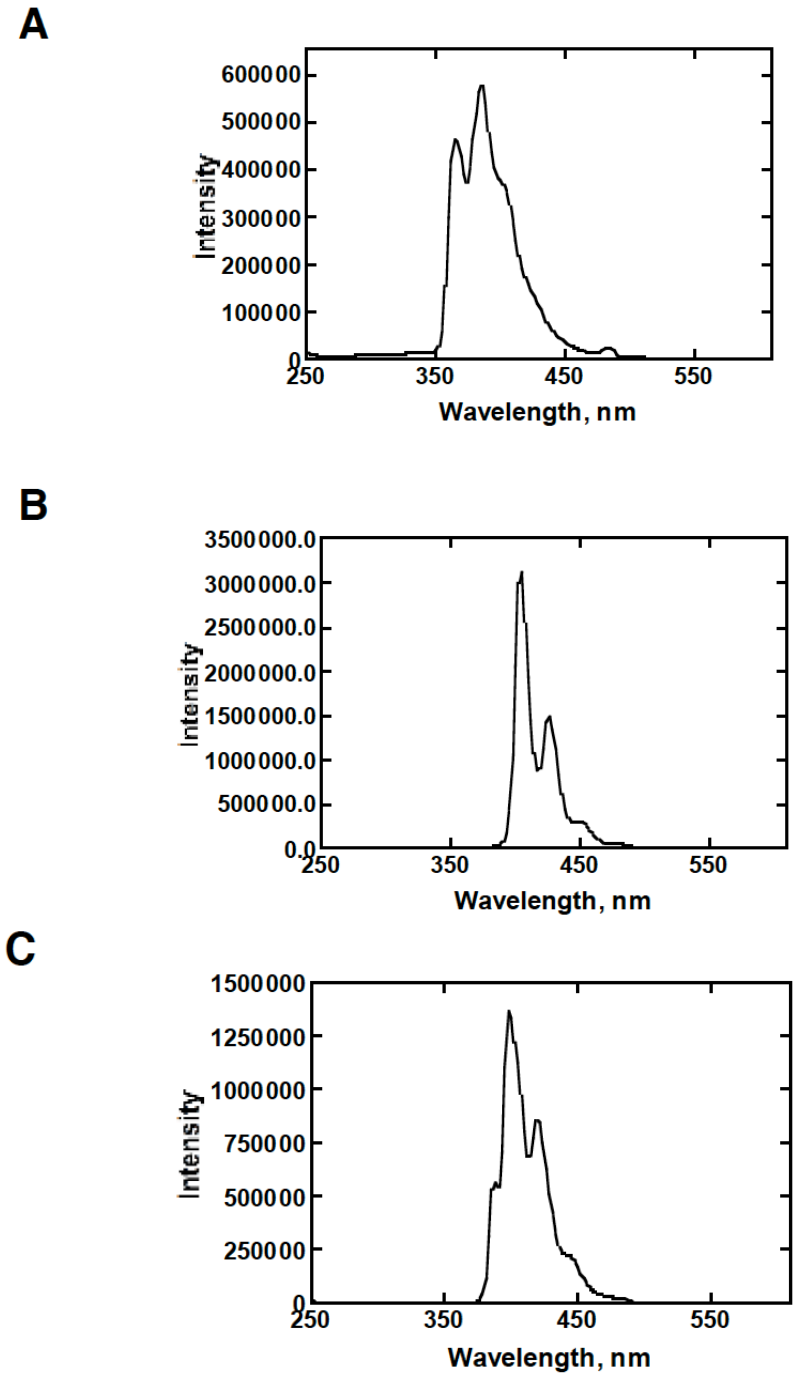

Figure 13. Characterization of di-OH pyrenes: fluorescence spectra. *A*, Peak 1, assigned as 1,5 di-OH pyrene. *B*, Peak 2, 1,6 di-OH pyrene. *C*, Peak 3, 1,8 di-OH pyrene. The spectra were recorded with an OLIS DM-45 instrument, with excitation at 240 nm in all cases.

Figure 14. Characterization of di-OH pyrenes: NMR spectra. *A*, Peak 1, assigned as 1,5 di-OH pyrene. *B*, Peak 2, 1,6 di-OH pyrene. *C*, Peak 3, 1,8 di-OH pyrene. In each case, the 1-dimensional ^{1}H-NMR and the (2-dimensional) COSY, HMQC, and HMBC spectra are shown.

A

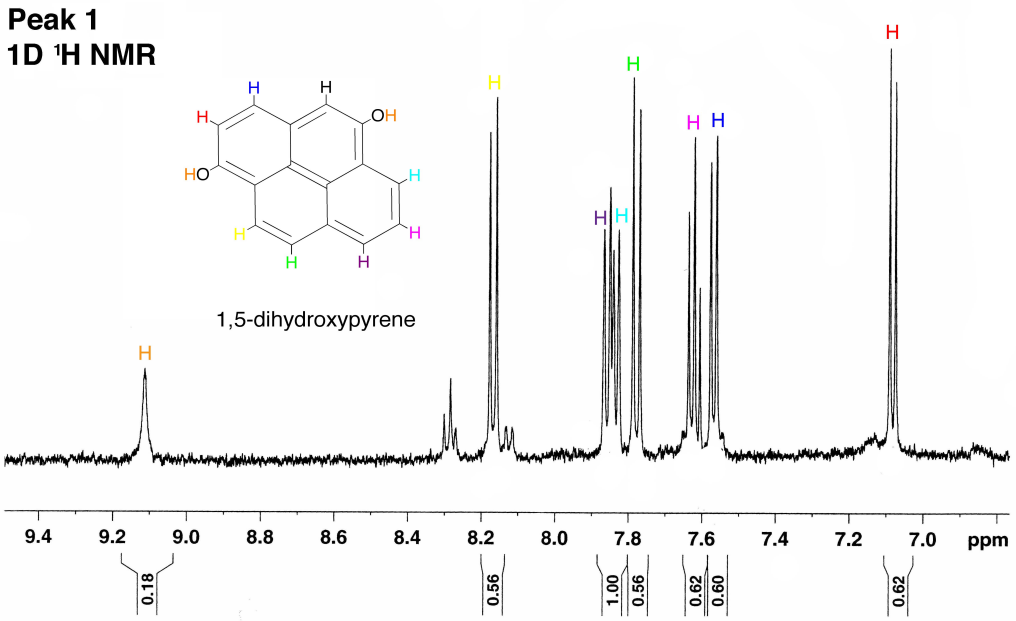
Peak 1
1D ¹H NMR
1,5-dihydroxypyrene
9.4
9.2
9.0
8.8
8.6
8.4
8.2
8.0
7.8
7.6
7.4
7.2
7.0
ppm
0.18
0.56
1.00
0.56
0.62
0.60
0.62

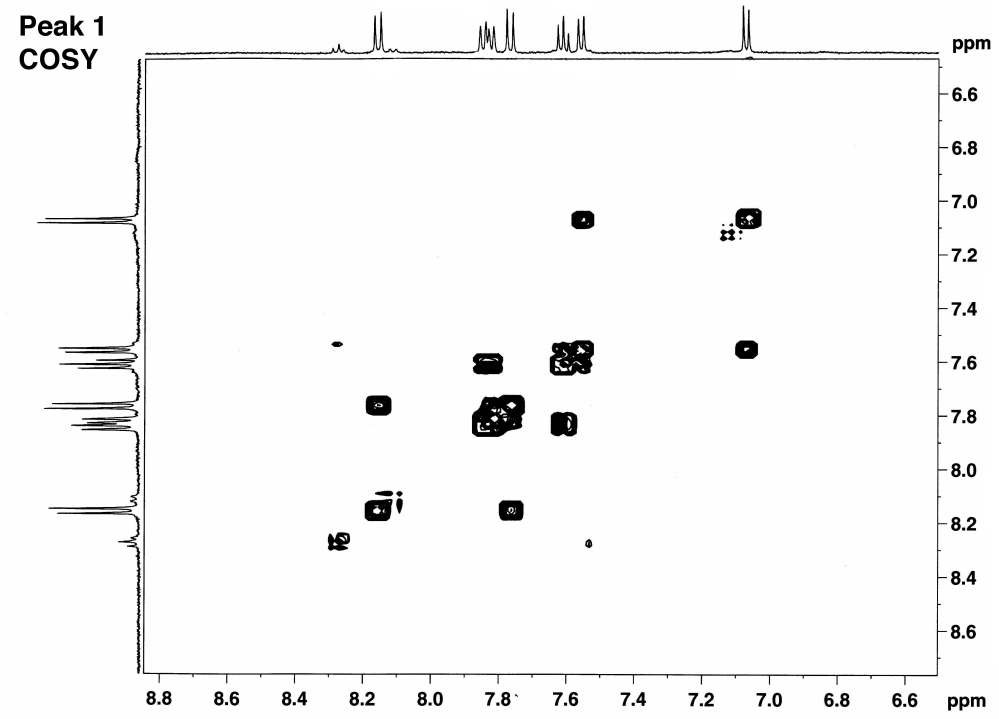
Peak 1
COSY
ppm
6.6
6.8
7.0
7.2
7.4
7.6
7.8
8.0
8.2
8.4
8.6
8.8
8.6
8.4
8.2
8.0
7.8
7.6
7.4
7.2
7.0
6.8
6.6
ppm

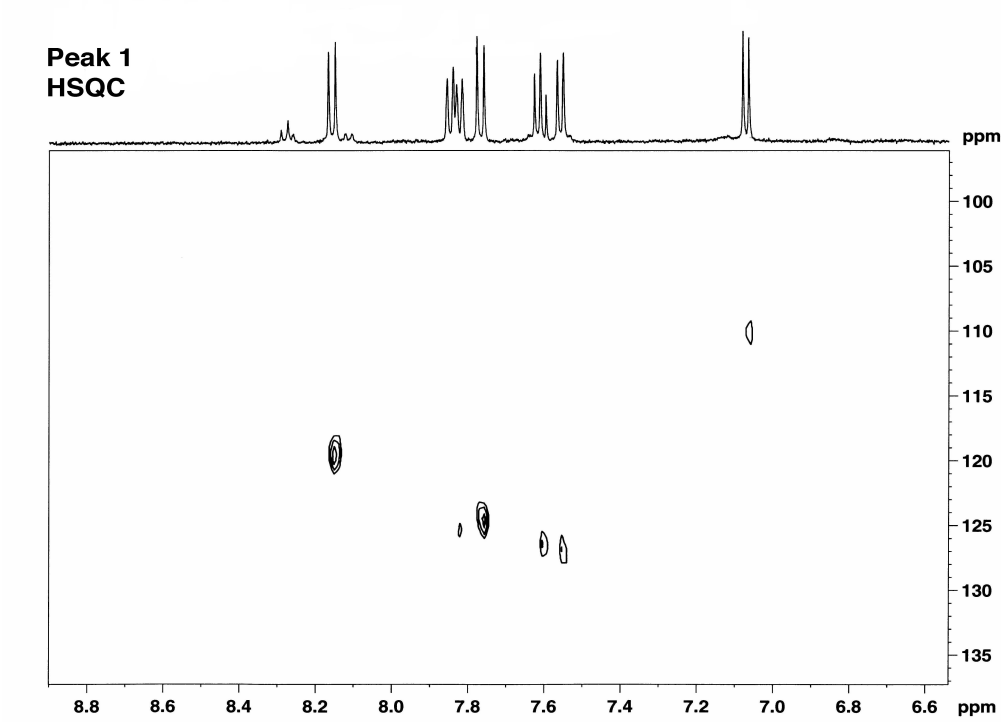
Peak 1
HSQC
ppm
100
105
110
115
120
125
130
135
8.8
8.6
8.4
8.2
8.0
7.8
7.6
7.4
7.2
7.0
6.8
6.6
ppm

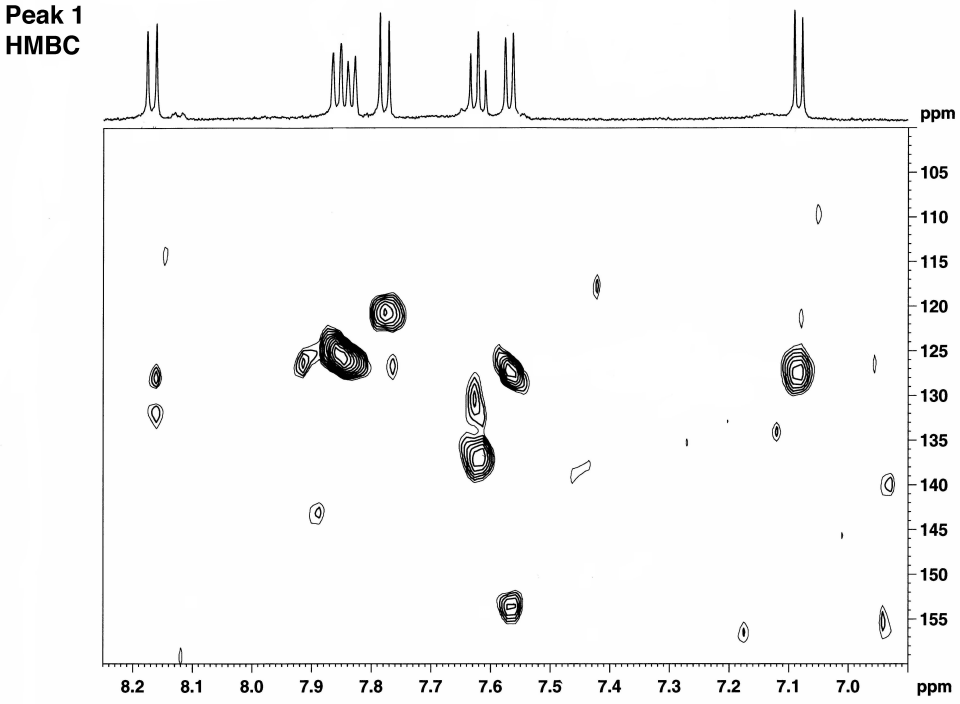
Peak 1
HMBC
ppm
105
110
115
120
125
130
135
140
145
150
155
8.2
8.1
8.0
7.9
7.8
7.7
7.6
7.5
7.4
7.3
7.2
7.1
7.0
ppm

B

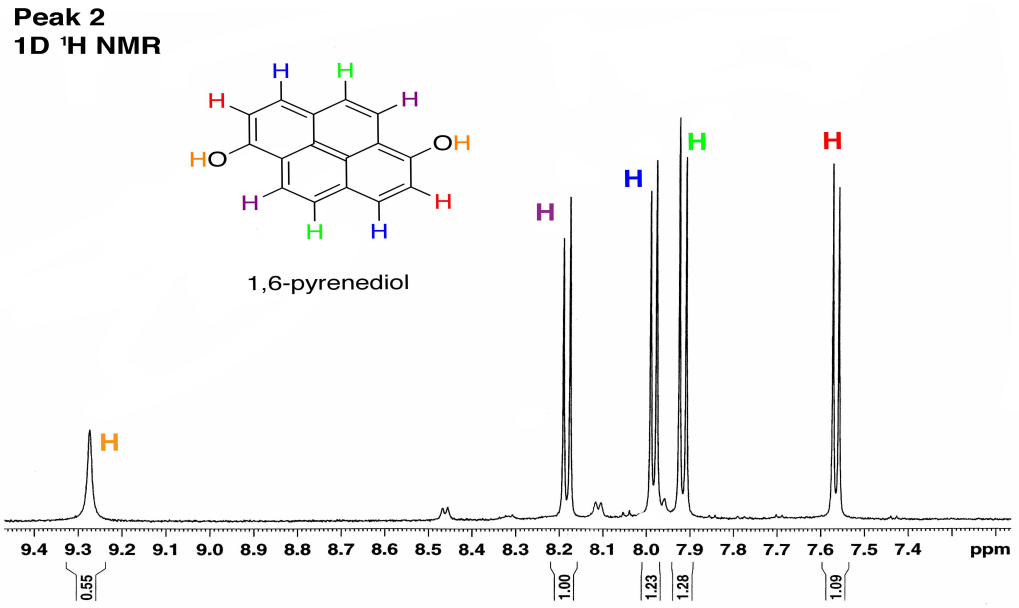
Peak 2
1D ¹H NMR
1,6-pyrenediol
9.4 9.3 9.2 9.1 9.0 8.9 8.8 8.7 8.6 8.5 8.4 8.3 8.2 8.1 8.0 7.9 7.8 7.7 7.6 7.5 7.4 ppm
0.55
1.00
1.23
1.28
1.09

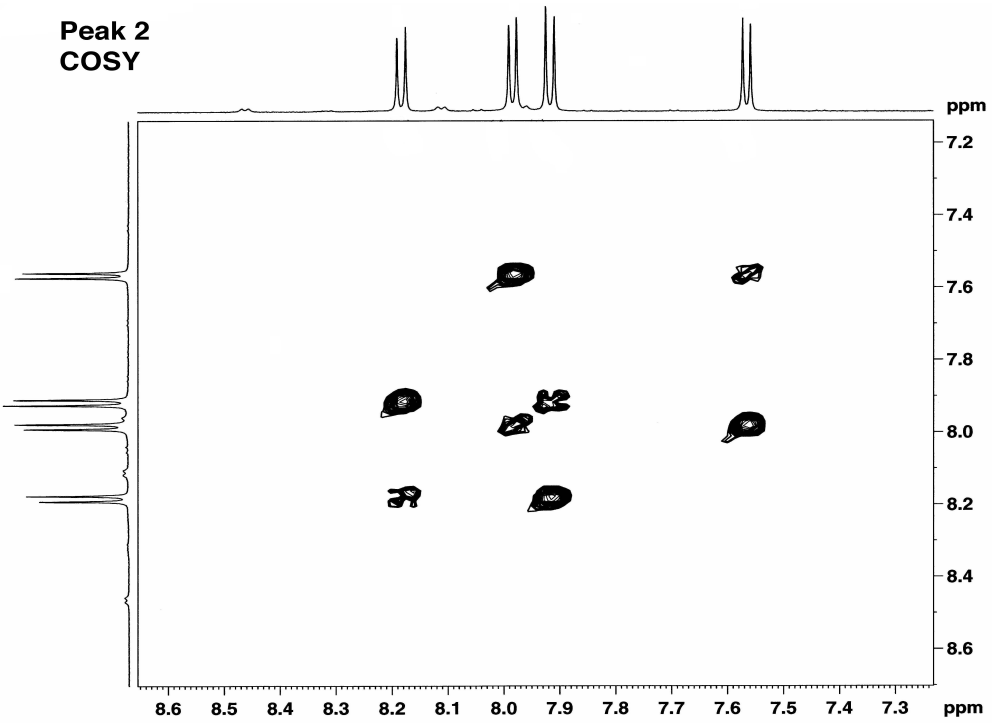
Peak 2
COSY
ppm
7.2
7.4
7.6
7.8
8.0
8.2
8.4
8.6
8.6 8.5 8.4 8.3 8.2 8.1 8.0 7.9 7.8 7.7 7.6 7.5 7.4 7.3 ppm

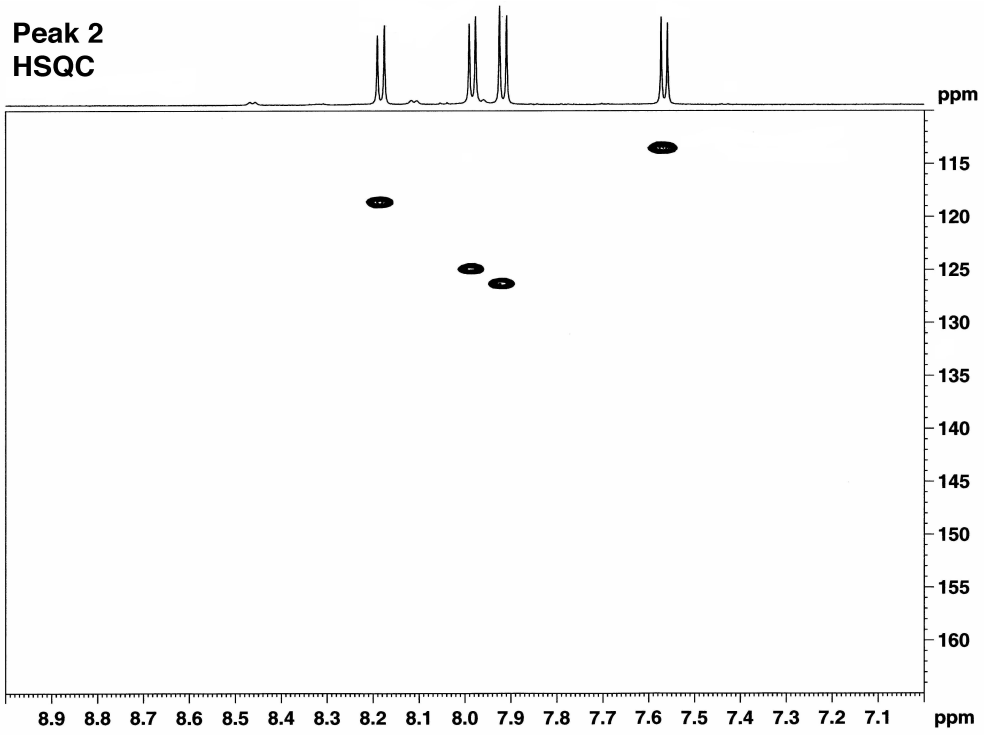
Peak 2
HSQC
ppm
115
120
125
130
135
140
145
150
155
160
8.9 8.8 8.7 8.6 8.5 8.4 8.3 8.2 8.1 8.0 7.9 7.8 7.7 7.6 7.5 7.4 7.3 7.2 7.1
ppm

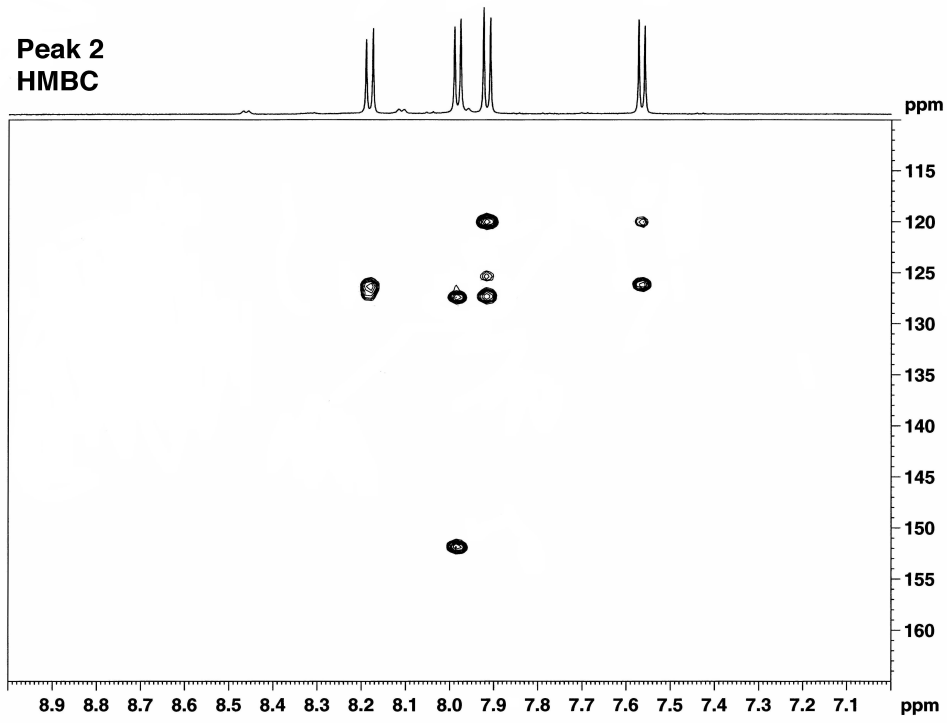
Peak 2
HMBC
ppm
115
120
125
130
135
140
145
150
155
160
8.9 8.8 8.7 8.6 8.5 8.4 8.3 8.2 8.1 8.0 7.9 7.8 7.7 7.6 7.5 7.4 7.3 7.2 7.1
ppm

C

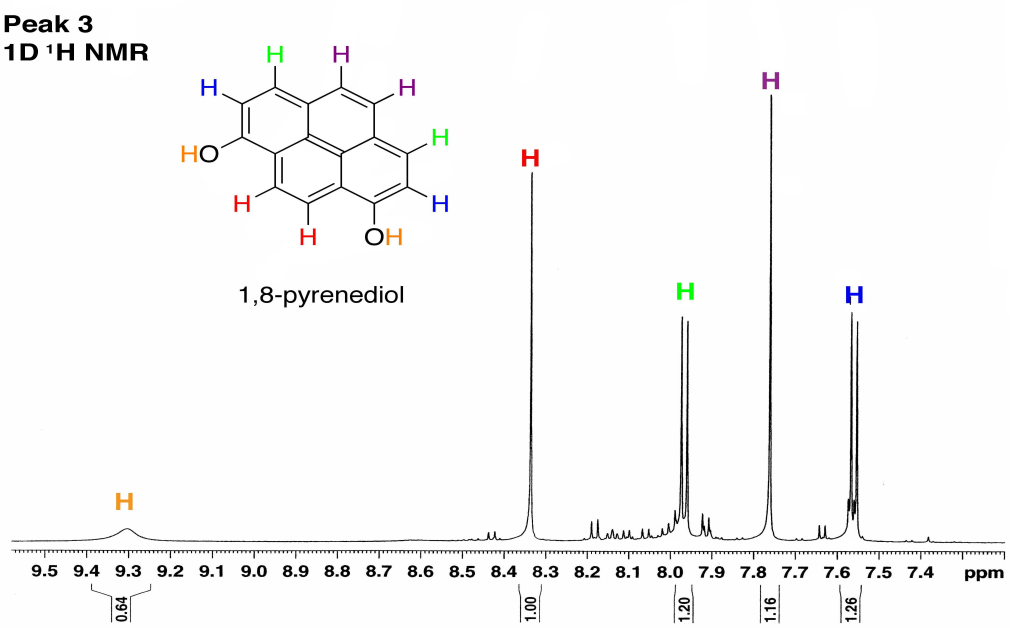
Peak 3
1D ¹H NMR
1,8-pyrenediol
9.5 9.4 9.3 9.2 9.1 9.0 8.9 8.8 8.7 8.6 8.5 8.4 8.3 8.2 8.1 8.0 7.9 7.8 7.7 7.6 7.5 7.4 ppm
0.64
1.00
1.20
1.16
1.26

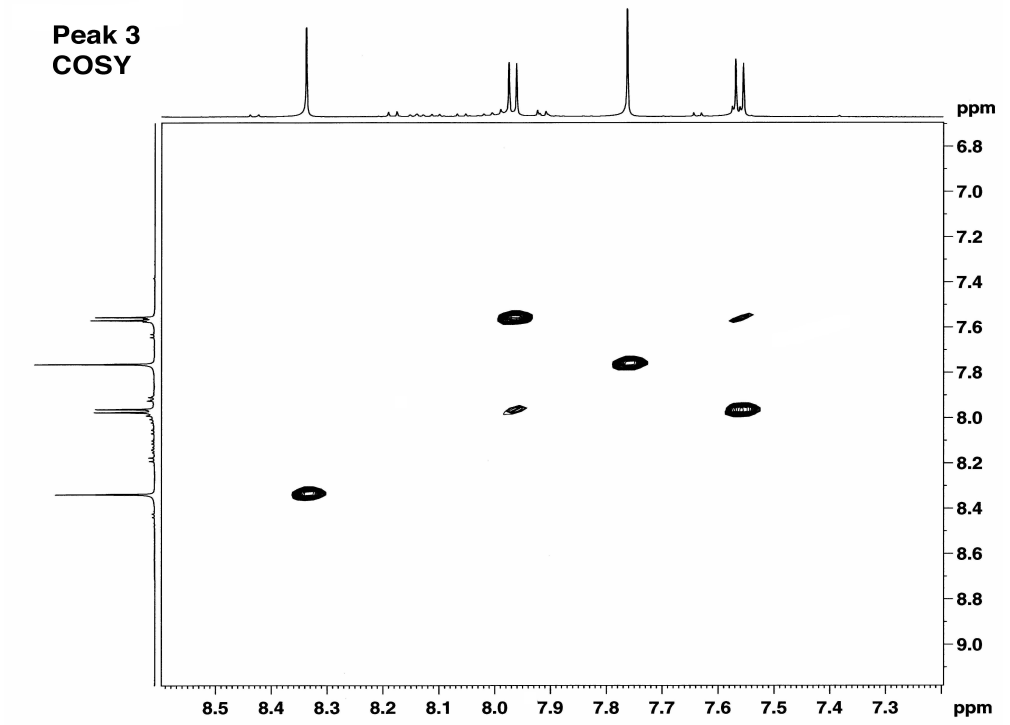
Peak 3
COSY
ppm
6.8
7.0
7.2
7.4
7.6
7.8
8.0
8.2
8.4
8.6
8.8
9.0
8.5 8.4 8.3 8.2 8.1 8.0 7.9 7.8 7.7 7.6 7.5 7.4 7.3 ppm

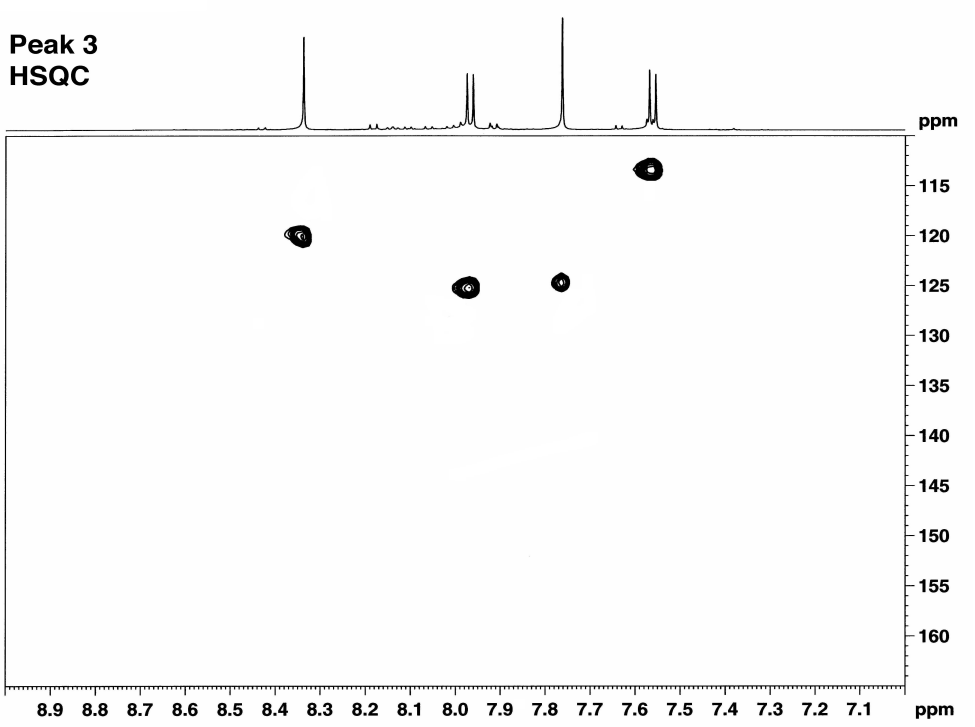
Peak 3
HSQC
ppm
115
120
125
130
135
140
145
150
155
160
8.9 8.8 8.7 8.6 8.5 8.4 8.3 8.2 8.1 8.0 7.9 7.8 7.7 7.6 7.5 7.4 7.3 7.2 7.1
ppm

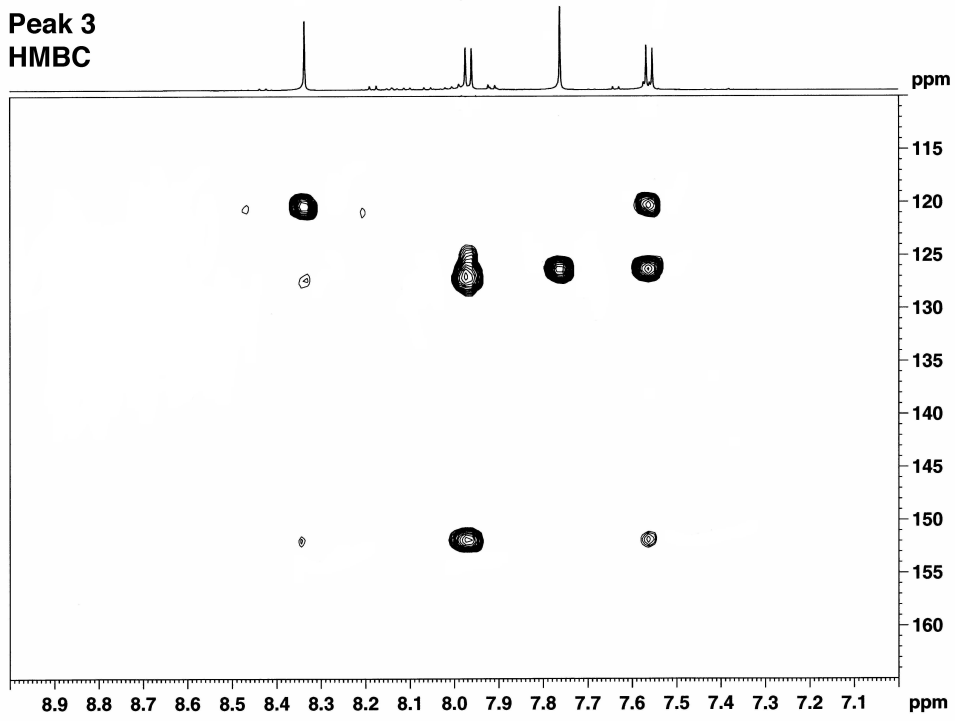
Peak 3
HMBC
ppm
115
120
125
130
135
140
145
150
155
160
8.9 8.8 8.7 8.6 8.5 8.4 8.3 8.2 8.1 8.0 7.9 7.8 7.7 7.6 7.5 7.4 7.3 7.2 7.1
ppm

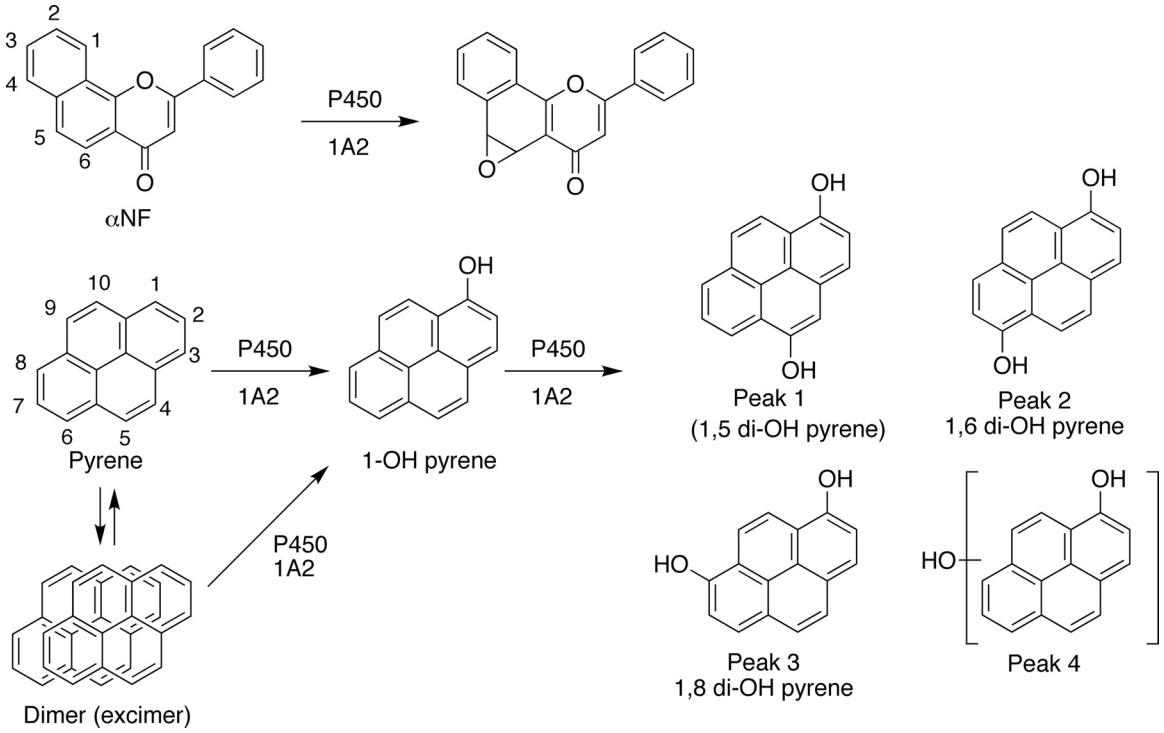

Figure 15. Oxidations of αNF and pyrene by rabbit P450 1A2.

The compounds in Peaks 2 and 3 were readily identified by their NMR patterns, which were both simplified because of the symmetry in the molecules. Further, the NMR and UV spectra of peaks 2 and 3 matched those of 1,6 and 1,8 di-OH pyrene previously reported in the literature (115, 116).

Identification of Peak 1 as 1,5 di-OH pyrene should be considered tentative. Peak integration of the 1-dimensional ^{1}H-NMR (Figure 14) shows 7 protons in the aromatic region, not including the hydroxyl protons. However, all non-symmetric di-OH pyrenes should have 8 protons, so the absent proton is of concern because the MS data (Figure 11) clearly revealed a molecular ion corresponding to a di-OH pyrene (Figure 11). This spectral data eliminated a symmetrical disubstituted pyrene (i.e., 1,3, 1,6, or 1,8 di-OH pyrene). Absence of a singlet and the presence of a triplet in the 1-dimensional ^{1}H-NMR spectrum precluded 1,2 and 1,7 di-OH pyrene, respectively. Further, 1,4, 1,9, and 1,10 di-OH pyrene were tentatively eliminated based on HSQC spectra analysis and correlation information provided by COSY spectra. Thus Peak 1 was tentatively assigned as 1,5 di-OH pyrene, with some caveats regarding missing HMBC correlations and the absence of one of the expected eight protons in the aromatic region.

Steady-state Kinetics of P450 1A2 Reactions—Results of incubations of αNF and pyrene with rabbit P450 1A2 are shown in Figure 15. A plot of the rate of 5,6-epoxidation *vs*. αNF concentration yielded a typical hyperbolic plot (Figure 16*A*). In contrast to the plots of *v vs*. substrate concentration for αNF (Figure 16*A*) and many other rabbit P450 1A2 substrates (117-119), the plots for pyrene 1-hydroxylation were consistently very sigmoidal (Figure 16*B*). When the data were fit to a Hill expression

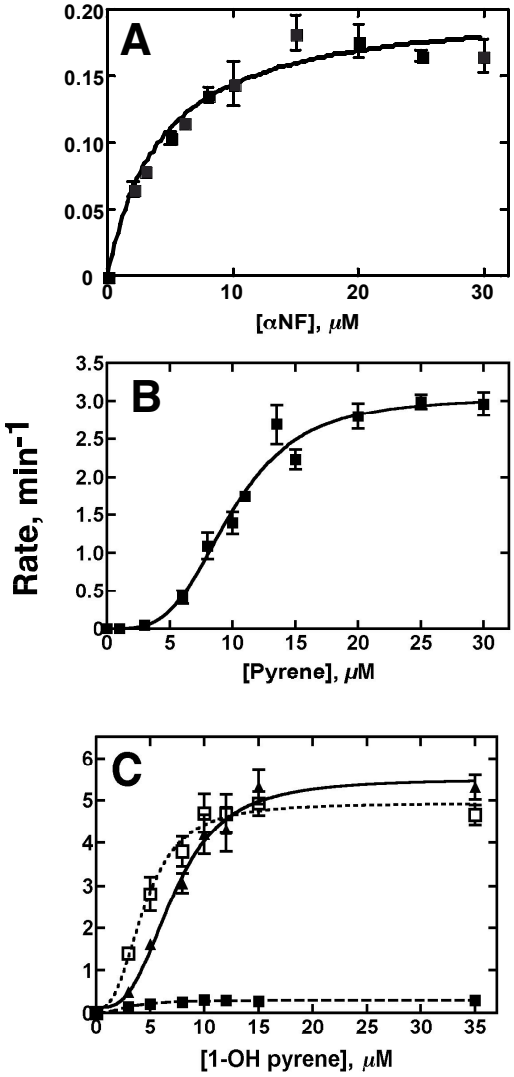

Figure 16. Steady-state kinetics of oxidations catalyzed by P450 1A2. *A*, αNF 5,6-epoxidation, with hyperbolic fitting. k_{cat} 0.21 ± 0.01 min^{-1}, K_m 4.3 ± 0.7 μM. *B*, Pyrene 1-hydroxylation; data points are set to the equation $v = k_{cat} \cdot S^n (S_{50}{}^n + S^n)^{-1}$ with k_{cat} = 3.0 ± 0.1 min^{-1}, n = 3.6 ± 0.6 and S_{50} = 9.9 ± 0.5 μM. *C*, Oxidations of 1-OH pyrene; data points are also set to a Hill equation: Peak 1 (assigned as 1,5 di-OH pyrene, ■): k_{cat} = 0.30 ± 0.02 min^{-1}, n = 2.2 ± 0.8, S_{50} = 3.2 ± 0.5 μM; Peak 2 (1,6 di-OH pyrene, ▲): k_{cat} = 5.5 ± 0.3 min^{-1}, n = 3.0 ± 0.8, S_{50} = 7.2 ± 0.7 μM; Peak 3 (1,8 di-OH pyrene, ❑): k_{cat} = 4.9 ± 0.3 min^{-1}, n = 2.7 ± 0.7, S_{50} = 4.5 ± 0.6 μM. Under these conditions, the substrate concentration was not depleted, even at the low substrate concentrations.

(*vide supra*) the apparent *n* values were ≥ 3. When the oxidations of 1-OH pyrene to the di-OH products were analyzed, the *v vs*. substrate concentration plots were sigmoidal (Figure 16*C*), with *n* values of 2-3. In other studies with (recombinant) human P450 1A2, the same oxidations of αNF and pyrene were observed but the rates were ~ 5-fold slower.The plot was also sigmoidal for pyrene 1-hydroxylation for human P450 1A2 studies (Figure 17).

Steady-state Binding of Ligands to Ferric P450 1A2—Rabbit P450 1A2, as isolated, contains a mixture of low- and high-spin heme iron (96, 120). Binding of some substrates further shifts the equilibrium to the high-spin form (96), a so-called "Type I" shift (43). (Recombinant human P450 1A2 is isolated nearly completely in the high-spin form and is not amenable to such analysis (47, 96).) The preparation used in this work was 77% low-spin, as established by second-derivative analysis of the ferric Soret peak (121, 122) (Figure 18).

Titration of P450 1A2 with either αNF (Figure 19), pyrene, or 1-OH pyrene yielded such Type I spectral changes (Figure 20). The results are indicative of sub-μM K_d values and quadratic fitting of the data points was necessary. The apparent K_d values estimated by this method were 17, 36, and 200 nM for αNF, pyrene, and 1-OH pyrene, respectively (Figures 19 and 20).

Pre-steady-state Kinetics of Ligand Binding to Ferric P450 1A2: Absorbance—Pre-steady-state kinetic analysis was used to address the question of whether the spin-state change (Figure 20) is the first event observed upon binding of substrates and other

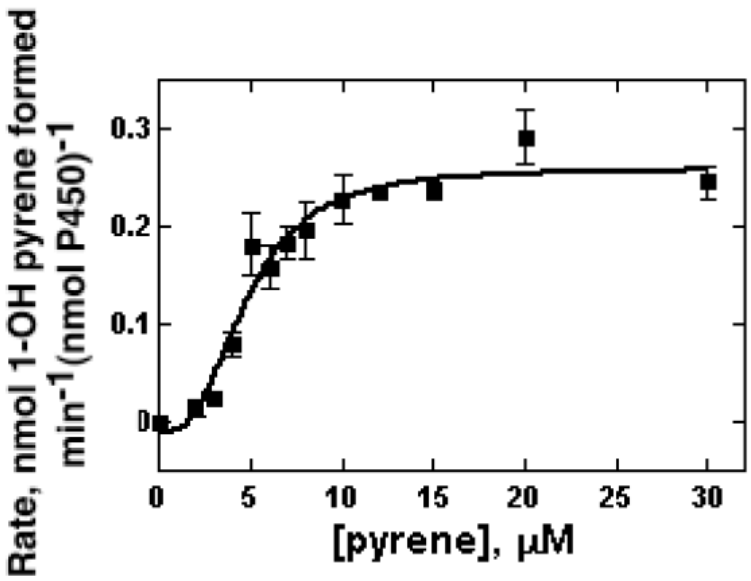

Figure 17. Steady-state kinetics of pyrene 1-hydroxylation by human P450 1A2.

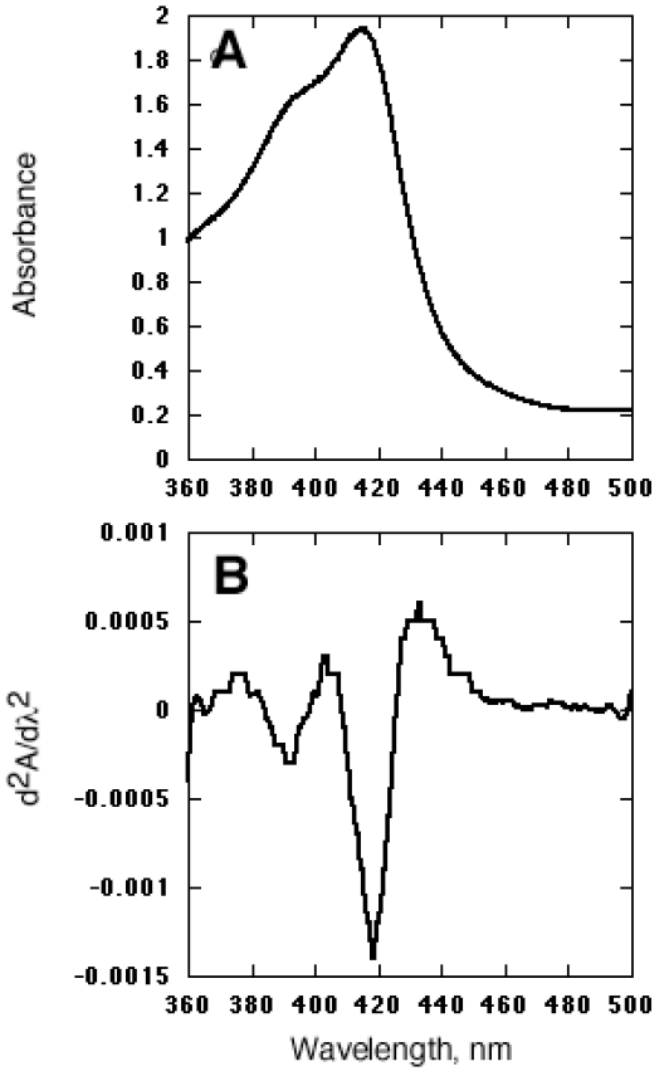

Figure 18. Absorbance and second-derivative spectra of P450 1A2. *A,* Absorbance spectrum of P450 1A2. *B*, Second derivative of *A*. The second derivative spectrum was obtained with the OLIS software of the Cary14/OLIS instrument. Quantitation of the negative peaks at 418 and 390 nm yields estimates of the contents of low- and high-spin heme iron, respectively.

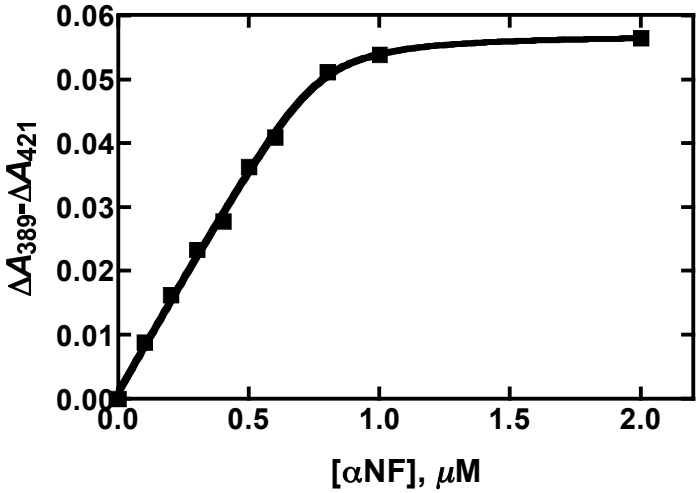

Figure 19. Binding of αNF to P450 1A2. The data points were fit to a quadratic equation with $n = 1$ and $K_d = 17 \pm 8$ nM.

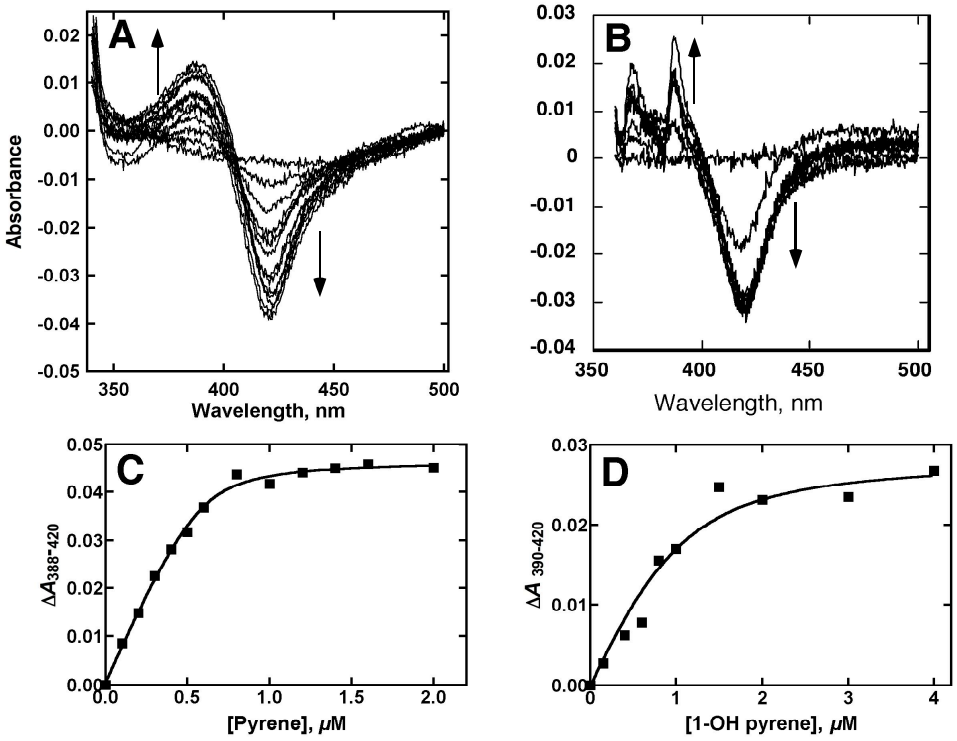

Figure 20. Steady-state ligand binding to ferric P450 1A2. Absorbance difference spectra obtained from titration of P450 1A2 (1 μM). Arrows indicate directions of the spectral shifts upon ligand addition. *A*, Pyrene (0–2 μM). *B*, 1-OH pyrene (0–6 μM). The 1-OH pyrene absorbance at 385 nm was corrected for in the calculations. *C*, Plot of ΔA_{388}-A_{420} versus pyrene concentration, fit to a quadratic expression in GraphPad Prism. K_d = 0.036 (± 0.017) μM. *D*, Plot of ΔA_{390}-A_{420} versus 1-OH pyrene concentration, fit to a quadratic equation. K_d = 0.20 (± 0.13) μM.

ligands. Preliminary analyses with equimolar concentrations of P450 1A2 and pyrene yielded a Type I change (A_{390} increase, A_{424} decrease), fit to an estimated second-order rate of ~ 4×10^5 M^{-1} s^{-1} (Figure 21). Binding of the known substrate $(CH_3)_2CH$-O-$PhNO_2$ (47), under pseudo-first order conditions, yielded a trace that could be best fit to a bi-exponential equation with rates of 2.9 and 0.08 s^{-1} (Figure 21*B*). Binding of αNF under pseudo-first order conditions yielded a plot that fit a bi-exponential equation with rates of 9.8 and 1.2 s^{-1} (Figure 21*C*).[3] Collectively the rates of these changes are rather slow to describe initial binding of ligands to proteins (46). Further, when the αNF experiment (Figure 21*C*) was repeated with the same reagents and the fluorescence quenching of αNF was observed, the plot was biphasic with the fast phase accounting for most of the decrease, at a rate of 50 s^{-1}, which is > 5-fold faster than the absorbance change (see more detailed analyses, *vide infra*). These results imply that the heme Soret changes are secondary to faster processes that occur when P450 1A2 binds ligands. The binding of 1-OH pyrene (20 μM) also yielded biphasic kinetics with rates (5.7 and 0.23 s^{-1}) similar to those observed using αNF and $(CH_3)_2CH$-O-$PhNO_2$ (Figure 21*D*).

Steady-state Interaction of Pyrene with Ferric P450 1A2 and Excimer Formation—Steady-state fluorescence emission spectra of pyrene, in solution with or without P450 1A2, were acquired by optical pumping at either 275 or 338 nm, two excitation wavelengths especially effective in generating pyrene excimer emission at ~

[3] This result is consistent with previous work in this laboratory done only for a shorter time and at a higher αNF concentration (40 μM) (108).

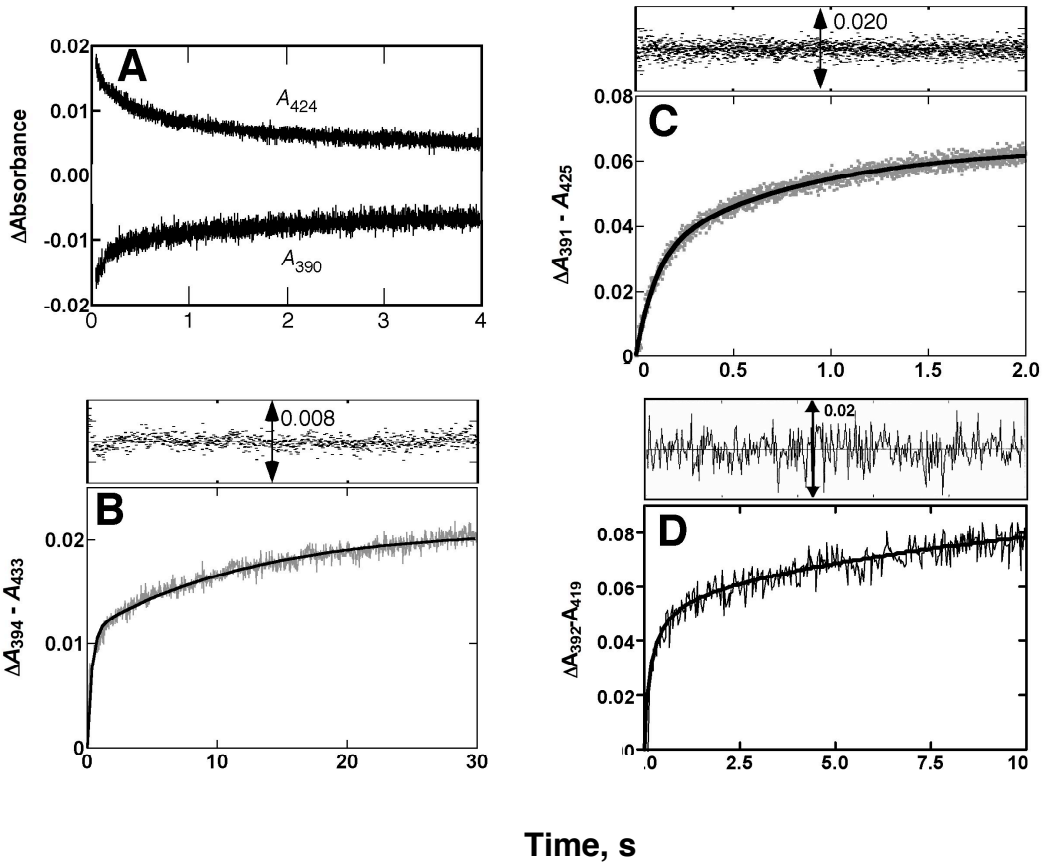

Figure 21. Pre-steady-state kinetics of ligand binding to ferric P450 1A2 (absorbance). *A*, Pyrene. Reaction with a mixture of P450 (2 μM) and pyrene (2 μM), fit to a second order rate constant of ~ 4 × 10^5 M^{-1} s^{-1} using the software of the OLIS RSM-1000 spectrophotometer. *B*, $(CH_3)_2CH$-O-$PhNO_2$ (in excess of P450). The kinetic trace (ΔA_{394}–A_{433}) obtained for $(CH_3)_2CH$-O-$PhNO_2$ (10 μM) binding to P450 1A2 (1 μM) was fit to a bi-exponential plot with rates of 2.9 and 0.08 s^{-1} *C*, αNF. The kinetic trace (ΔA_{391}–A_{425}) obtained for αNF (4 μM) binding to P450 1A2 (2 μM) was fit to a bi-exponential plot with rates of 9.8 and 1.2 s^{-1}. *D*, 1-OH pyrene. The kinetic trace (ΔA_{392}–A_{419}) obtained for 1-OH pyrene (7.5 μM) was fit to a bi-exponential plot with rates of 5.7 and 0.23 s^{-1}. Residuals analyses for the fits are shown in the upper panels.

466 nm. For excimer emission to occur, the two pyrenes must be in close proximity and base-stacked (123, 124).

P450 1A2 quenched the fluorescence of pyrene in a concentration-dependent manner (Figure 22*A*). With an assumption that one molecule of pyrene is bound to each P450 1A2, a quadratic fit yielded an estimated K_d of 56 ± 1 nM (Figure 20*C*). If two pyrenes are bound per P450 under these conditions, then the expression for K_d is more complex, but nevertheless the affinity of P450 1A2 for pyrene is strong and the fluorescence is highly quenched.

A titration of P450 1A2 with pyrene, the opposite of the approach used in Figure 22*A*, revealed further features (Figure 22*B*). In this experiment, fluorescence emission was collected at either 370 or 485 nm (recording excitation scans), corresponding to monomer and excimer fluorescence, respectively, and the intensities of the fluorescence excitation bands at ~ 335 nm from either monomer or pyrene were quantified. The ratio of fluorescence emission at 370 to 485 nm is related to the pyrene monomer to excimer ratio (*M*/*E*) (125), as well as to the amount of quenching (Figure 22*B*). Because of the quenching of pyrene fluorescence by P450 1A2, it is useful to use this ratio instead of the actual fluorescence values. In the absence of P450 the pyrene dimerizes with increasing concentration when titrated into the buffer solution.

In the titration with P450 1A2, at lower concentrations of pyrene, the pyrene (monomer) fluorescence appears to be preferentially quenched. The amount of fluorescent monomer increases with increasing pyrene concentration. After addition of ~ 0.6 pyrene/P450 1A2, the ratio of monomer/excimer decreases, indicative of an increase in the contribution of a dimer of pyrene (Figure 22*B*).

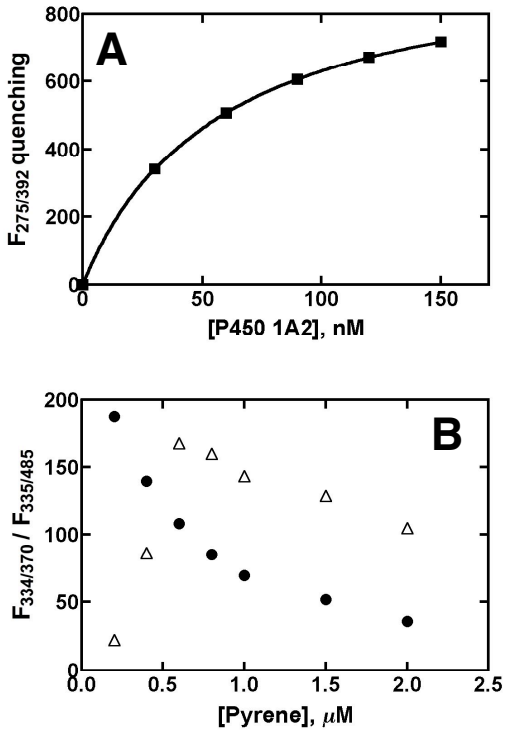

Figure 22. Pyrene/ferric P450 1A2 titrations. *A*, A 500 nM solution of pyrene was used to collect fluorescence emission spectra in the absence or presence of the indicated concentrations of P450 1A2. Excitation was at 275 nm and emission at 392 nm. The data were analyzed using a quadratic expression to correct for the ligand-bound and free enzyme (assuming one ligand bound) and yielded K_d = 56 ± 1 nM. *B*, The pyrene concentration was varied in the absence (●) or presence (△) of P450 1A2 (1.0 μM). The excitation wavelength used for analysis was 335 nm. The ratio of fluorescence emission at 370 nm relative to 485 nm is indicative of the ratio of monomer to excimer fluorescence (*M*/*E*) (the values do not imply molar ratios).

Pre-steady-state Kinetics of Ligand Binding to Ferric P450 1A2: Fluorescence— Preliminary results indicated that the quenching of the fluorescence of ligands occurred faster than the changes in the heme spectrum (*vide supra*). Accordingly the kinetics of these processes were analyzed in more detail.

The quenching of αNF fluorescence seen upon mixing with P450 1A2 fit a bi-exponential plot (Figure 23*A*). As the αNF concentration was increased, a second-order rate constant could be estimated to be 6.5×10^6 M^{-1} s^{-1} (results not presented).[4] This rate constant is much faster (> 10-fold) than that observed for the UV-visible changes (Figure 20*C*). The reaction of pyrene with P450 1A2 showed a very rapid decrease in the monomer fluorescence (Figure 22*B*). The rate of 70 s^{-1} at a pyrene concentration of 2 μM suggests a second-order rate constant of ~ 10^6 - 10^7 M^{-1} s^{-1}, similar to that estimated for αNF (Figure 23*A*).

As the monomer fluorescence decreased, a small increase in the apparent excimer (dimer) fluorescence occurred and then this slowly decreased (Figure 23*C*). One interpretation of this time course is a sequence of pyrene monomer binding to protein, the formation of a dimer, and then the movement of the dimer to interact with protein residues to decrease the excimer fluorescence. Alternatively the protein may be binding a pre-formed dimer from solution and the fluorescence properties may be changing as it moves within the protein. The latter explanation is favored because at higher concentrations of pyrene (10 to 20 μM), an initial decrease in > 455 nm emission (to

[4] The binding model is probably more complex than a simple two-state (bound/unbound) situation, in that the apparent k_{off} (20 s^{-1}) and k_{on} yield the ratio $K_d = k_{off}$ (20 s^{-1})/k_{on} (6.5×10^6 M^{-1} s^{-1}) of ~ 3 μM, which is not consistent with the low K_d estimated from the steady-state absorbance results (Figure 18).

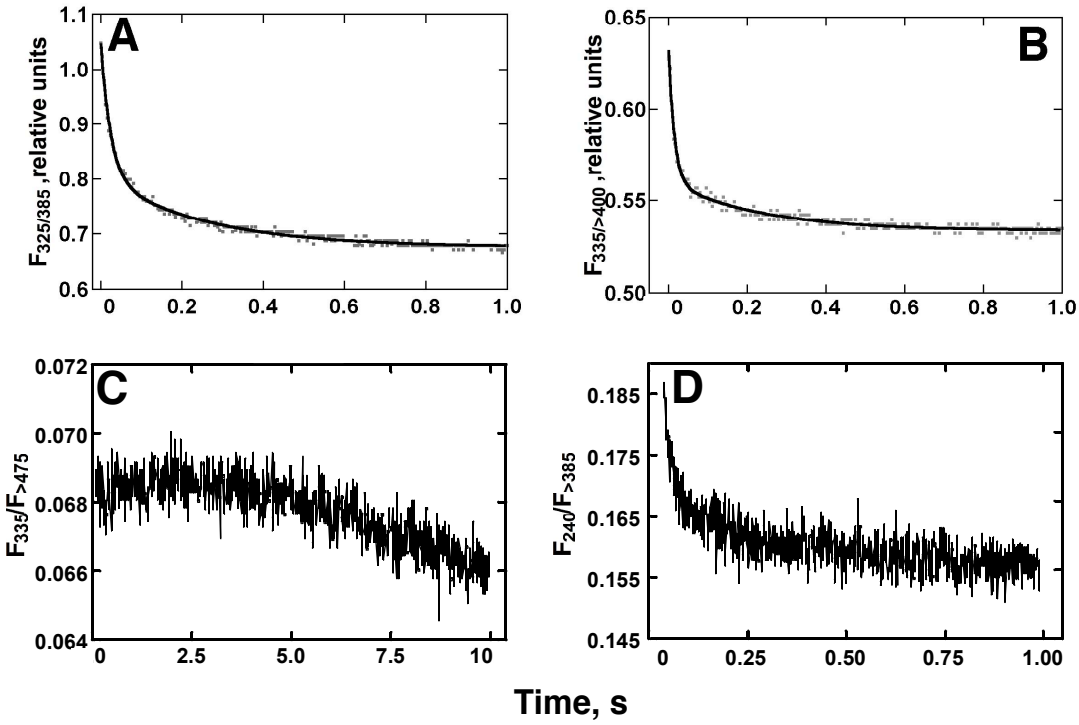

Figure 23. Pre-steady-state kinetics of ligand binding to ferric P450 1A2 (fluorescence). The excitation and emission wavelengths are indicated in the y-axes. *A*, αNF. The kinetic trace for the αNF (3 μM) fluorescence emission decay (> 385) upon interaction with P450 1A2 was fit to a bi-exponential plot with rates of 41 and 4.0 s^{-1}. A plot of the rates (from bi-exponential fits as shown) obtained for the first phase versus αNF concentration yielded a second-order rate constant of 6.5 × 10^6 M^{-1} s^{-1} (results not presented); *B*, Pyrene. The kinetic trace for the pyrene monomer emission (emission > 400 nm) decay upon interaction with P450 1A2 fit to a bi-exponential plot with rates of 70 and 4.4 s^{-1}. *C*, Kinetic trace for pyrene fluorescence emission > 475 nm (indicative of excimer emission) upon interaction with P450 1A2. *D*, 1-OH pyrene. The kinetic trace for 1-OH pyrene (7.5 μM) fluorescence emission > 385 upon interaction with P450 1A2 was fit to a bi-exponential plot with rates of 95 and 4.7 s^{-1}.

~ 1 s) was followed by an increase in this fluorescence and then a decrease (5-10 s period).

The binding of 1-OH pyrene to P450 1A2 was also biphasic (Figure 23*D*), with the fast phase estimated at ~ 85 s^{-1} using a 1-OH pyrene concentration of 15 μM (slower phase ~ 3 s^{-1}). Analysis of the rates of the fast phase as a function of the 1-OH pyrene concentration yielded an apparent k_{on} of ~ 3 × 10^6 M^{-1} s^{-1} (plot not presented). This rate is much faster than that of the Soret absorbance change (~ 3 s^{-1} at 15 μM, Figure 21*D*), which corresponds approximately to the slower fluorescence phase (Figure 23*D*). To my knowledge, 1-OH pyrene does not form excimers (at concentrations relevant to these experiments), and none of the steady-state fluorescence spectra suggested such a phenomenon.

Interactions of Pyrene with Ferrous P450 1A2—Although the catalytic cycle for P450 1A2 is usually depicted in the general manner shown in Figure 4, the point can be made that the events should not necessarily be considered in a linear, sequential manner (93). P450 1A2 is reduced at the same rate in the absence or presence of substrates (108) and the binding and release of substrate at the ferrous level (and possibly others) is possible and probably happens with many P450-substrate combinations (93).

Pyrene binds to ferrous P450 1A2 and produces a change in the heme spectrum (Figure 24*A*). Anaerobic titration yielded an apparent K_d value of 2.3 (± 0.8) μM (Figure 24*B*). Kinetic analysis of the binding showed a rapid increase in A_{426} (Figures 24*C* and 24*D*), followed by a slower bi-exponential decrease in A_{426} (Figures 24*E* and 24*F*).

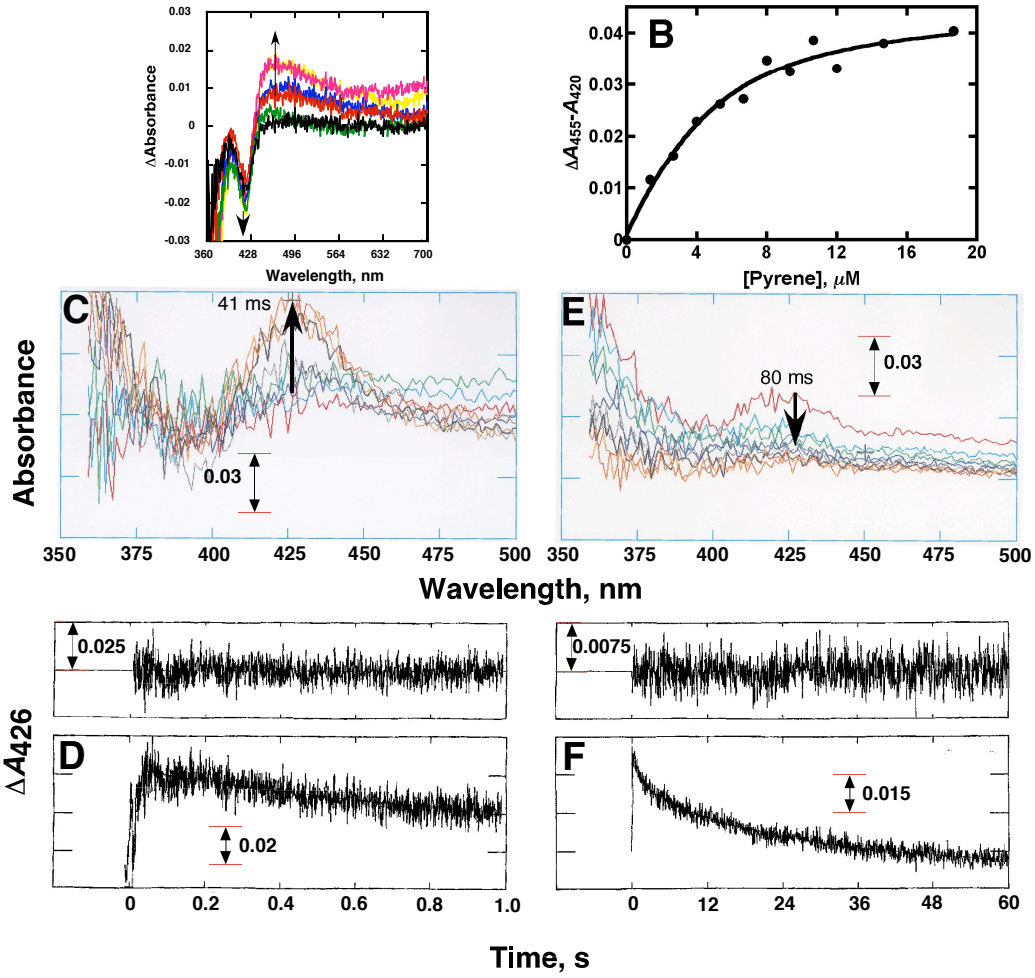

Figure 24. Binding of pyrene to ferrous P450 1A2. *A*, Changes in P450 1A2 UV-visible difference spectrum following addition of pyrene (2.3-10.7 μM) to ferrous P450 1A2. P450 1A2 (4 μM) was mixed with 1 μM NADPH-P450 reductase (and 75 μM L-α-dilauroyl-*sn*-glycero-3-phosphocholine) and reduced anaerobically, in the presence of a glucose oxidase/catalase/glucose scrubbing system (108), with an NADPH-generating system (101). The baseline was set to zero throughout the wavelength range with ferrous P450 1A2, and changes were set against this baseline. The arrows show the direction of changes with increasing pyrene concentration. *B*, Absorbance changes from part *A* fit to a quadratic equation with K_d = 2.3 ± 0.8 μM. *C*, P450 1A2 (5 μM) was mixed with 1 μM NADPH-P450 reductase (and 75 μM L-α-dilauroyl-*sn*-glycero-3-phosphocholine) and reduced anaerobically with an NADPH-generating system. In the experiments shown, the final concentration of pyrene (after mixing) was 20 μM. Difference spectra were collected every 1 ms and are shown for 5 ms intervals up to 41 ms. *D*, The ΔA_{426} data were fit to a biexponential expression (absorbance increase, then decrease) with k_1 = 106 ± 11 s^{-1} and k_2 = 1.0 ± 0.3 s^{-1}. *E*, Latter phases of reaction after mixing. The first spectrum shown was collected at 80 ms, and subsequent spectra were collected every 2.4 s. *F*, Data from Part *E* were fit to a biexponential decrease in A_{426} with k_2 (corresponding to second part in Part *B*) = 0.66 ± 0.11 s^{-1} and k_3 = 0.041 ± 0.002 s^{-1}.

The kinetic course of the reaction is of significance, in that it distinguishes between multiple populations of enzyme (in slow equilibrium or aggregational states) participating in the same reaction at different rates, in contrast to an apparent single population of enzyme undergoing a sequential series of reactions with a substrate. The pattern observed here with sequential trends in opposite directions is clearly more consonant with the latter view of multiple sequential reactions.

CD Measurements of Interaction of Ligands with Ferric P450 1A2—The addition of any of four ligands (pyrene, 1-OH pyrene, αNF, or $(CH_3)_2CH$-O-$PhNO_2$) to P450 1A2 produced a significant change (7-29%, depending on the ligand) in the CD spectra (UV region, ~ 220 nm). The change may be due in part to a decrease in the α-helicity of the protein, as judged by the changes at 220 nm although such changes proved too rapid to be measured by CD-stopped-flow techniques (126), (127) (data not presented).

Docking of Ligands in a Model of P450 1A2—The human P450 1A2 crystal structure (23) allowed a homology model of the rabbit enzyme to be generated using the Swiss Model program. The feasibility of binding of multiple ligands to the rabbit P450 1A2 model active site was assessed by manually docking the ligands and then performing simulated annealing of the protein-ligand complex. Superimposing the human P450 1A2 crystal structure (protein data bank code 2HI4) containing the heme group and αNF with the rabbit P450 1A2 model places the αNF moiety directly in the active site of the homology model (23) (Figures 25*A*). The homology model is almost identical to the experimentally derived structure (root mean square deviation 0.097), which is not

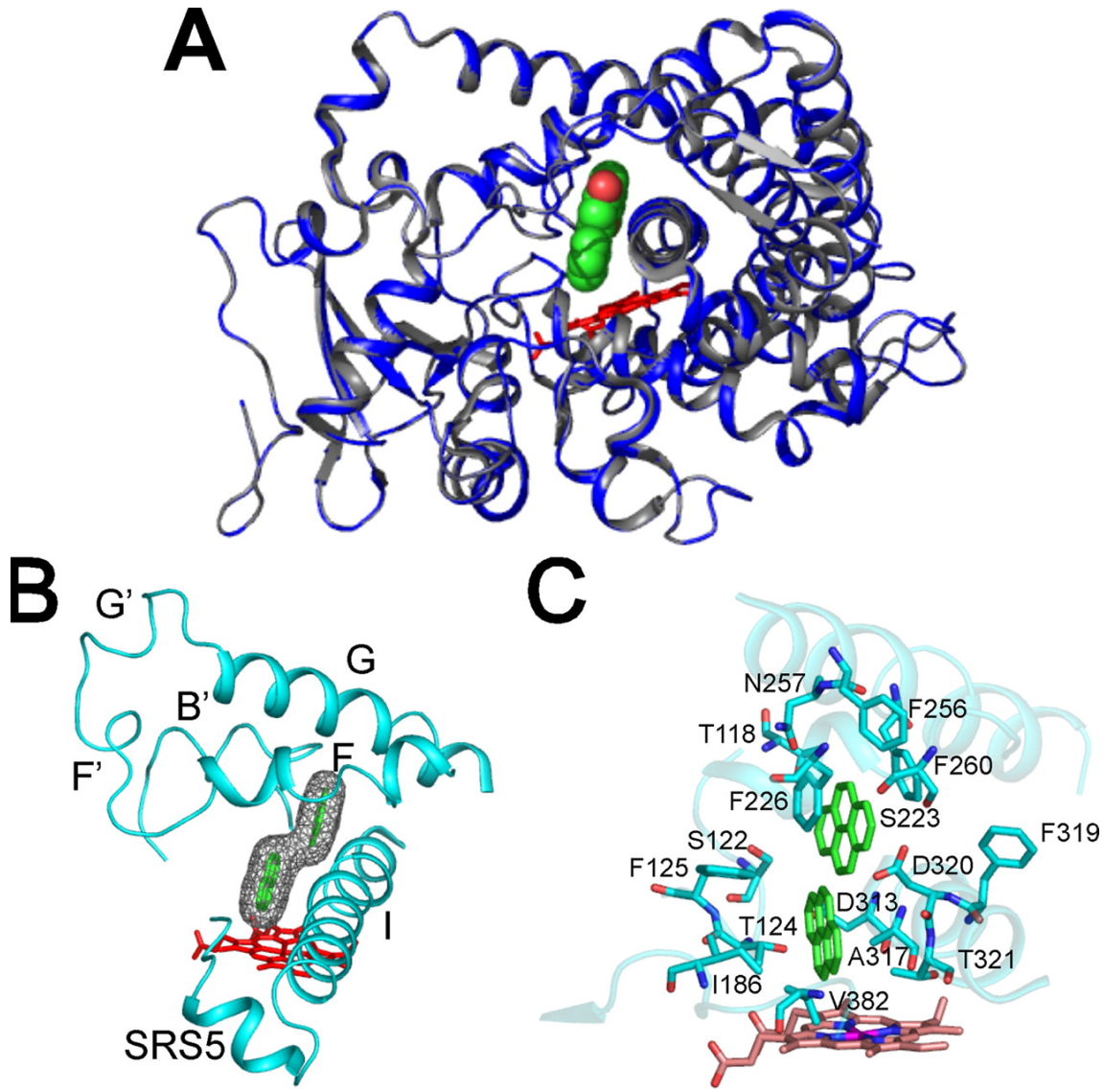

Figure 25. Docking of ligands into a homology model of rabbit P450 1A2. *A*, Human P450 1A2 (gray ribbon; protein data bank code 2HI4) in complex with heme group (red sticks) and αNF (space-filling) superimposed with rabbit P450 1A2 homology model (blue ribbon). *B*, Rabbit P450 1A2 homology model (cyan ribbon) with heme group (red sticks) and two pyrenes (green sticks with space-filling mesh). *C*, Active site of rabbit P450 1A2 homology model (cyan ribbon) containing heme group (red sticks) and two pyrenes (green sticks) with side-chains highlighted. SRS5, substrate recognition site 5 (129).

surprising given the sequence similarity of the two enzymes (75% sequence identity (128)). It is of interest to note that the only site of αNF that is oxidized (5,6 bond: Figures 15 and 16*A*) is positioned furthest from the heme iron in both the published human P450 1A2 structure (32) and the model shown here (Figure 25*A*) and thus presumably this is not a catalytically competent configuration.

Two pyrene molecules were docked in the active site of the rabbit homology model. While two pyrene molecules can clearly fit in the active site, direct stacking of the two molecules does not appear to be favorable. Rather, an end-on-end conformation—with some overlap, is less perturbing to the homology model used here (Figure 25*B*). By trying several different starting conformations, a model was obtained in which two pyrene molecules stack in excimer fashion (i.e. overlaid directly over one another), but this orientation causes some disruption of the I-helix and may not represent a viable complex. More likely, the formation of any fluorescent excimer may be transient in nature, which would be consistent with the relatively weak fluorescence signal (Figures 25*B* and 25*C*). The overall binding interactions observed in the human P450 1A2 -αNF co-crystal structure are largely maintained in the model containing two pyrene molecules, with van der Waals interactions comprising most of the enzyme-substrate contacts (Figure 25*C*). Other notable similarities include the potential for orthogonal and parallel aromatic interactions between the pyrenes and the phenylalanine side chains of residues 125 and 226, which are essentially identical to those reported previously with αNF (23).

The docking studies (Figures 25*B* and 25*C*) suggested that two benzo[*a*]pyrene molecules could readily be fit into the P450 1A2 active site. An assay of benzo[*a*]pyrene

hydroxylation, using a fluorimetric assay (which detects mainly 3-hydroxylation (100, 101, 130)) showed highly cooperative behavior (Figure 26). The low rate is similar to that reported previously with this enzyme at single benzo[*a*]pyrene concentrations (12, 130, 131).

Simulation of Binding and Steady-state Hydroxylation Kinetics—A variety of spectral methods were used to monitor interactions of P450 1A2 in this work. The interactions with pyrene are of particular interest, and a kinetic model that could explain the UV-visible changes that occur upon binding was developed (Figures 20*A* and 21*A*). Kinetic model building was also done with hydroxylation rates. While a Hill expression (*vide supra*) can be used to fit the steady-state kinetic data, it does not provide a mechanistic explanation for the behavior. The goal was a model, having a minimal number of steps, that could adequately fit three diverse sets of data: (i) pre-steady-state absorbance changes observed upon the binding of pyrene to P450 1A2 (Figure 21*A*), (ii) the sigmoidal *v vs*. substrate concentration plots observed for pyrene 1-hydroxylation (Figure 16*B*), and (iii) the temporal pattern of pyrene depletion, 1-OH pyrene formation and depletion, and formation of di-OH pyrenes (experiment of Figure 10*C* done with a higher concentration of pyrene). The model also requires a low K_d for the first pyrene binding event (Figure 20*A*) and a reasonably low K_d for 1-OH pyrene binding (Figure 20*B*).

All modeling was done with the program DynaFit (44). Initial modeling was done with the pyrene 1-hydroxylation *v vs*. substrate concentration data set (Figure 16*B*). The strongly sigmoidal nature of the points presented a challenge, and a reasonable solution

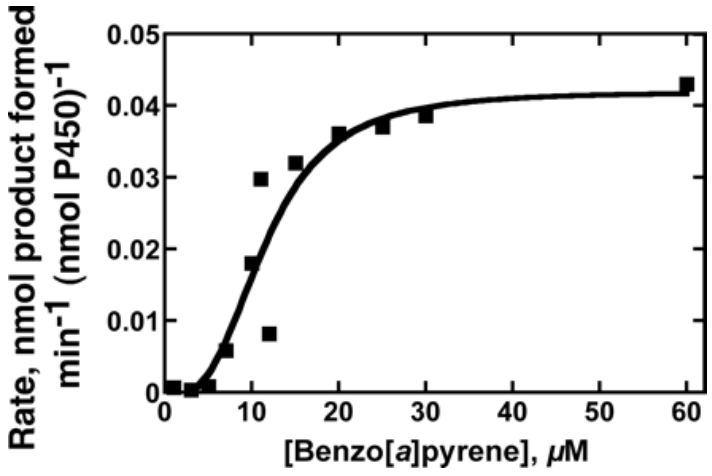

Figure 26. Steady-state kinetics of benzo[*a*]pyrene hydroxylation catalyzed by P450 1A2. Data points are set to the equation $v = k_{cat} \cdot S^n (S_{50}{}^n + S^n)^{-1}$, with $k_{cat} = 0.042 \pm 0.006$ min^{-1}, $n = 3.0 \pm 1.5$, and $S_{50} = 12 \pm 2$ μM. Under these conditions, the substrate concentration was not depleted, even at the low substrate concentrations.

was a model with two substrates in which only the dimeric complex (ESS) was catalytically active. The phenomena are reminiscent of the case of a bacterial NO reductase, which was concluded to only perform reductions when two (NO) molecules were in the active site (132). The behavior of the enzyme could be described by the equation

$$\mathrm{E + S \underset{}{\overset{K_1}{\leftrightarrows}} ES + S \overset{K_2}{\leftrightarrows} ESS \rightarrow E + P\ (+ ES)}$$

and a quadratic expression (63)

$$v = k_{cat}[(1 + K_1/[S])(1 + K_2/[S])]^{-1}$$

which reduces to

$$v = k_{cat}[1 + K_1(1/[S] + K_2/[S]^2)]^{-1}$$

when $K_1 >> K_2$ (132).

Thus, one solution to the modeling of the *v vs*. substrate concentration points is to use a high K_d (~ 8 μM) for binding of the first pyrene molecule, followed by a very low K_d for the addition of the second ligand, i.e. < 1 μM, to produce the sharp rise in the rate following the initial binding event. Such a model has elements of classical positive cooperativity (133). However, this model is inconsistent with the observed tight initial

binding of a single pyrene (Figures 20*A* and 20*B*). Another potential solution is the use of a three-pyrene model, with tight binding of the first pyrene, loose binding of a second, and a tight binding of a third pyrene, with only the trimer serving as substrate. Such a model gave reasonable sigmoidal fits (results not presented) but seems inconsistent with the spatial docking models (Figure 25), although conceivably the third pyrene could reside outside of the substrate region (i.e. on the periphery of the protein, *vide infra*). However, in the absence of any direct physical evidence in its favor, a three-pyrene model should be considered too speculative at this point.

A model could also be readily developed with two pyrenes, with the first pyrene binding tightly and the second more loosely, and this model generated sigmoidal plots (Figure 27). The model was considered for its ability to also fit the pre-steady-state binding data. A "k_{on}" rate constant of 4×10^6 M^{-1} s^{-1} was used, based upon the fluorescence quenching work (e.g., Figure 23*B*).[5] Using a typical extinction coefficient for the ΔA_{390}- A_{420} observed upon substrate binding to a P450 (6.5×10^4 M^{-1} cm^{-1}) (93), the absorbance trace could be fit, but only if an equilibration event was added following the binding of the second pyrene (this model fit even with equal initial concentrations (2 μM) of enzyme and pyrene, as well as with excess pyrene). The importance of adding an

[5] An apparent binding rate constant of 4×10^6 M^{-1} s^{-1} was used in the kinetic modeling and analysis, which is based on typical rates of interaction of P450s and small ligands measured by fluorescence quenching (Figure 22). Such rate constants have been used previously in analysis with P450 3A4 (91, 92). For further discussion of "on" rates for proteins, see Fersht (46). The rate constant is not intended to be a diffusion-controlled limit because, as discussed (46), only a fraction of initial hits between a protein and a ligand are productive even in the sense of quenching the fluorescence of a ligand, due to electrostatics and geometry. The rate constants of the order of ~ 5×10^6 M^{-1} s^{-1} are consistent not only with the P450 1A2 (Figure 22) and other P450 binding (91, 92) estimated by fluorescence interaction but also some heme Soret changes measured with P450s that appear to have simple binding phenomena (93, 94).

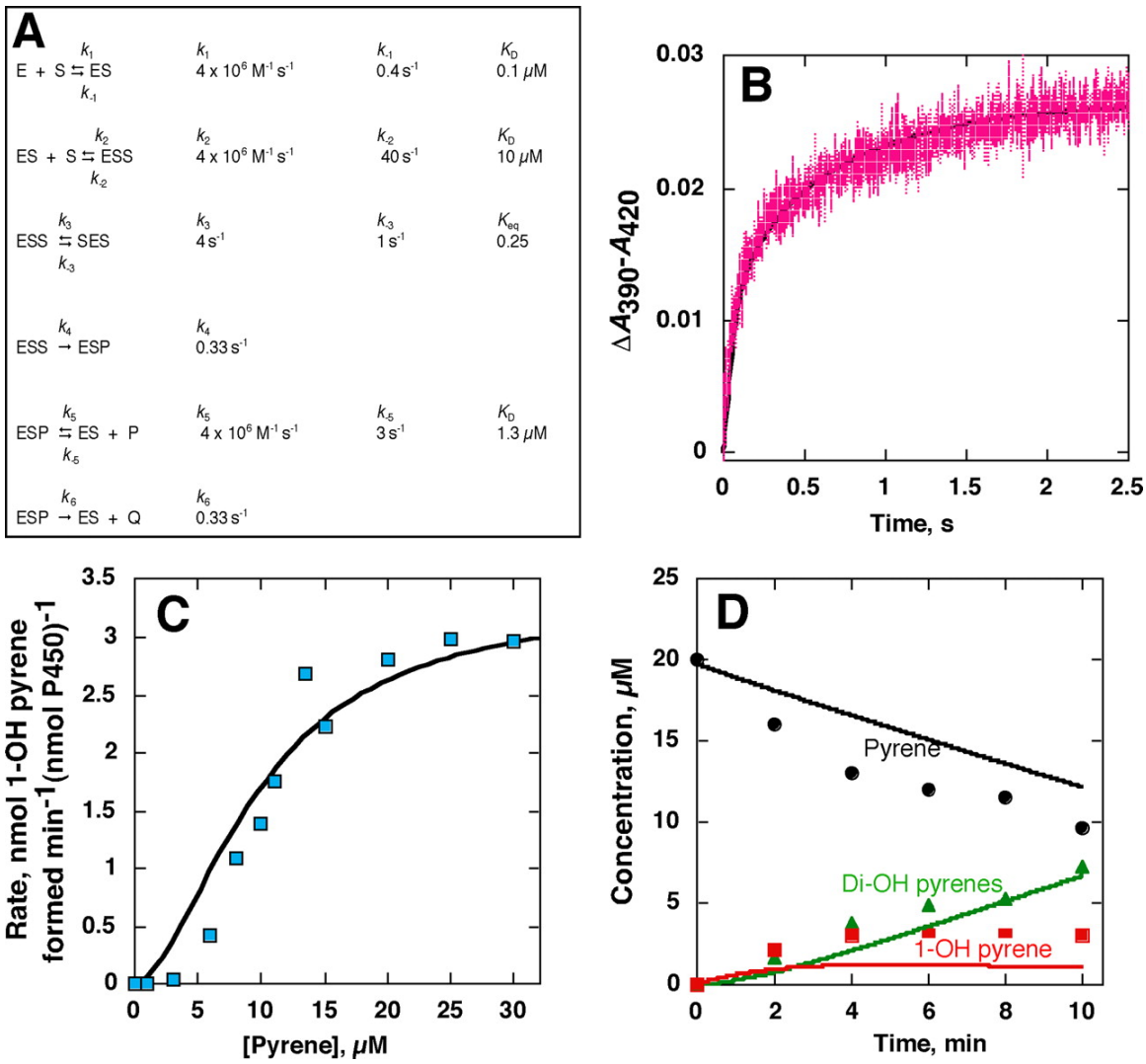

Figure 27. Fitting of pyrene binding (UV-visible absorbance data) and oxidation data to a kinetic model. *A*, Model and rate constants used in all fitting. E = P450 1A2, S = pyrene, P = 1-OH pyrene, Q = di-OH pyrenes (treated as a sum). *B*, Fitting of data of Figure 21*A* (absorbance changes (390 nm) seen for pre-steady-state binding of pyrene to P450 1A2) to the mechanism of Part *A*. *C*, Fitting of data of Figure 16*B* (*v vs*. substrate concentration plots for pyrene 1-hydroxylation) to the mechanism of Part *A*. *D*, Fitting of a temporal course of product formation and substrate (pyrene) disappearance to the mechanism of Part *A*.

equilibration event (Figure 27*A*) was seen in the comparison of Figure 27*B* with the same model without such a step (results not presented). In the model the initial complex produces no absorbance change but the ESS and SES (rearranged form) complexes do. When the ESS ⇆ SES equilibrium step was added to the initial mechanism developed for the *v vs*. substrate concentration data (*vide supra*), it did not change the character of the sigmoidal plot (Figure 27*C*), although the rate of the hydroxylation of 1-OH pyrene was reduced (k_6 in Figure 27*A*). Both the *v vs*. substrate concentration (Figure 27*C*) and ΔA_{390}-A_{420} *vs*. time (Figure 27*B*) fits showed some sensitivity to the rate of binding of pyrene in the models, although rates of 2 to 4 × 10^6 M^{-1} s^{-1} could be used. A model with only one substrate was unsatisfactory in that hyperbolic fits were always produced regardless of the rate constants (results not shown). Interestingly, the sigmoidal character of the plots required two distinct K_d values (k_{-1}/k_1 and k_{-2}/k_2) for pyrene (S) binding but was not dependent on the conversion of 1-OH pyrene (P) to di-OH pyrenes (Q).

The final set of boundaries to the model was fitting of the temporal pattern of changing pyrene, 1-OH pyrene, and di-OH pyrene concentrations in solution starting only with pyrene as substrate (Figure 10*C*). The fits were not unreasonable, although the steady-state level of 1-OH pyrene calculated from the model was only ~ one-half the measured concentration (Figure 27*D*). Raising k_4 in the model (Figure 27*A*) improved this difference but also produced a rate that was too fast in the *v vs*. substrate concentration plots (Figure 27*C*).

The final kinetic model for the oxidation of pyrene by rabbit P450 1A2 is presented in Figure 27*A*, along with the fits to each set of data (Figures 27*B*, 27*C*, and 27*D*). DynaFit scripts are presented in the Appendix, and the corresponding DynaFit

results are shown in Figures 28, 29, and 30. The low K_d values (spectroscopic binding) of pyrene (Figures 20*A* and 20*C*) and 1-OH pyrene (Figures 20*B* and 20*D*) are consistent with the model (Figure 27*A*), assuming that the presence of a pyrene does not affect the binding of 1-OH pyrene (ESP *vs*. EP complexes).

Discussion

Spectroscopy—Several spectroscopic methods were utilized in the kinetic studies, and these reveal different features of the system. CD spectroscopy provided some evidence for conformational changes, possibly in α-helicity, upon ligand binding and the time frame appeared too rapid to be captured by stopped-flow techniques (results not shown). The changes in the fluorescence of ligands (Figures 22 and 23) are valuable in that they provide evidence for an interaction of the ligands (pyrene, 1-OH pyrene, αNF) with P450 1A2 prior to the UV-visible changes associated with the heme iron spin-state transition, as in the case with P450 3A4 and its ligands (91, 92). The UV-visible changes are also useful regarding the multiphasic behavior and provide insight into the relative rates of individual steps, following the initial Soret-invisible kinetic event. The UV-visible spectral changes seen in the binding of pyrene with ferrous P450 1A2 (Figure 24) are of particular relevance in that the multiphasic changes are in a series of opposite directions and distinguish a sequential reaction sequence from parallel reactions of two slowly-interconverting enzyme populations.

This work leaves some uncertainty about the course of events related to pyrene excimers. The situation is complex because excimers form in solution (as well as

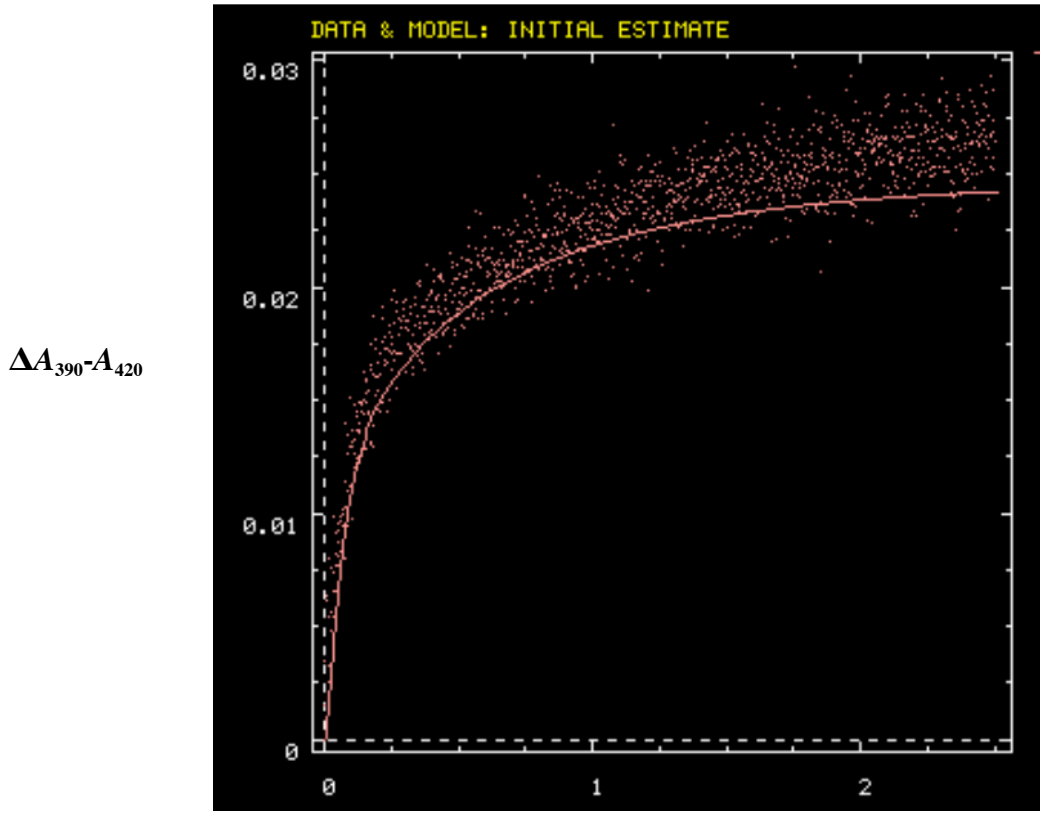

Figure 28. DynaFit files for fitting results of pyrene binding (UV-visible absorbance data). (See Appendix for corresponding DynaFit scripts.) The system was used for the final model (Figure 27*A* and 27*B*).

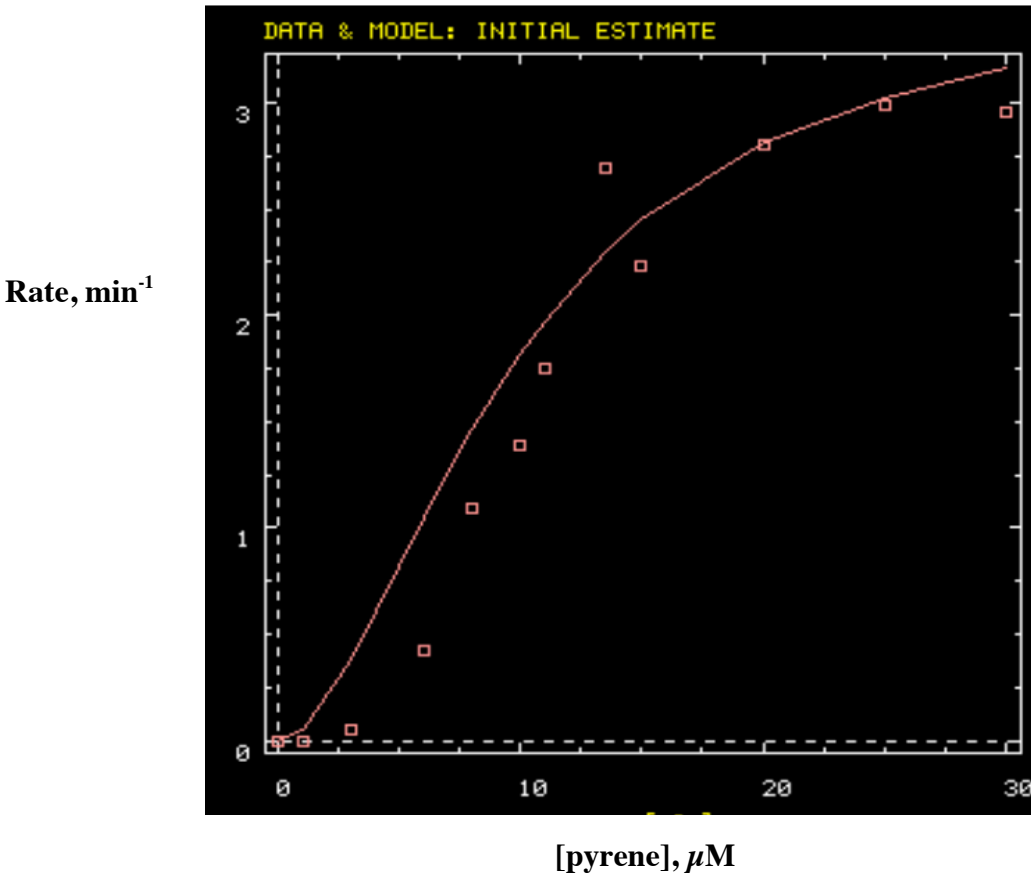

Figure 29. DynaFit results for fitting the *v vs.* substrate concentration plot for pyrene 1-hydroxylation data. (See Appendix for corresponding DynaFit scripts.) The system was used for the final model (Figures 27*A* and 27*C*).

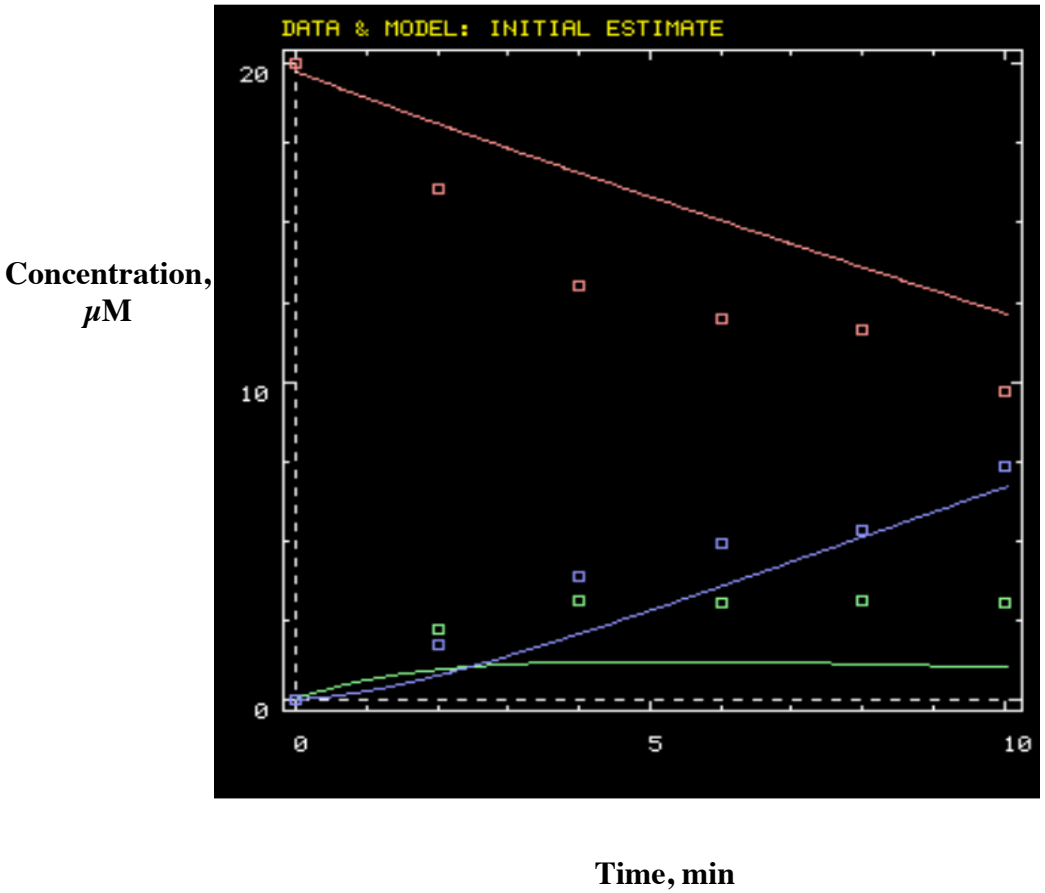

Figure 30. DynaFit results for fitting pyrene product formation data. (See Appendix for corresponding DynaFit scripts.) The red corresponds to pyrene, the green 1-OH pyrene, and the blue is the sum of the di-OH pyrenes. The system was used for the final model (Figures 27*A* and 27*D*).

proposed in the active site, which are difficult to distinguish spectroscopically) and binding to P450 1A2 could quench the fluorescence of monomers or excimers. The course of the titration in Figure 22*B* can be interpreted in the context of two pyrenes being inserted sequentially into the active site (Figures 25 and 31), partially overlapping (Figure 25*B*) to produce the transient excimer fluorescence (Figure 23*C*), and then moving (Figure 31) to decrease the excimer fluorescence. Alternatively, the kinetic course of events (Figures 23*B* and 23*C*) could be explained by binding of a dimer from solution, movement into the active site, and then changes in the fluorescence as a function of the interactions with individual amino acids. This scenario may not seem as consistent with the titration results (Figure 22). However, some other interpretations of the fluorescence data cannot be ruled out at this time because of the equilibria between monomer and excimer populations in both free solution and the protein (i.e., Figure 15) and the lack of knowledge about the fluorescent properties of the bound species in each form. One issue is the concentration dependence of the mechanism, i.e. at higher pyrene concentrations a preformed dimer may bind whereas at lower concentrations a dimer could form in the active site. These possibilities would yield similar results in most of the kinetic modeling.

Overall, the kinetic results clearly indicate a rapid ligand binding process revealed by the fluorescence studies (Figure 23) and at least a biphasic process following that, which is observable with UV-visible methods. The kinetics of the events appear to vary with individual ligands (Figure 23). The course of events in the interaction of pyrene with ferrous P450 (Figure 24) is indicative of a sequential process, which is proposed to be operative in the other systems.

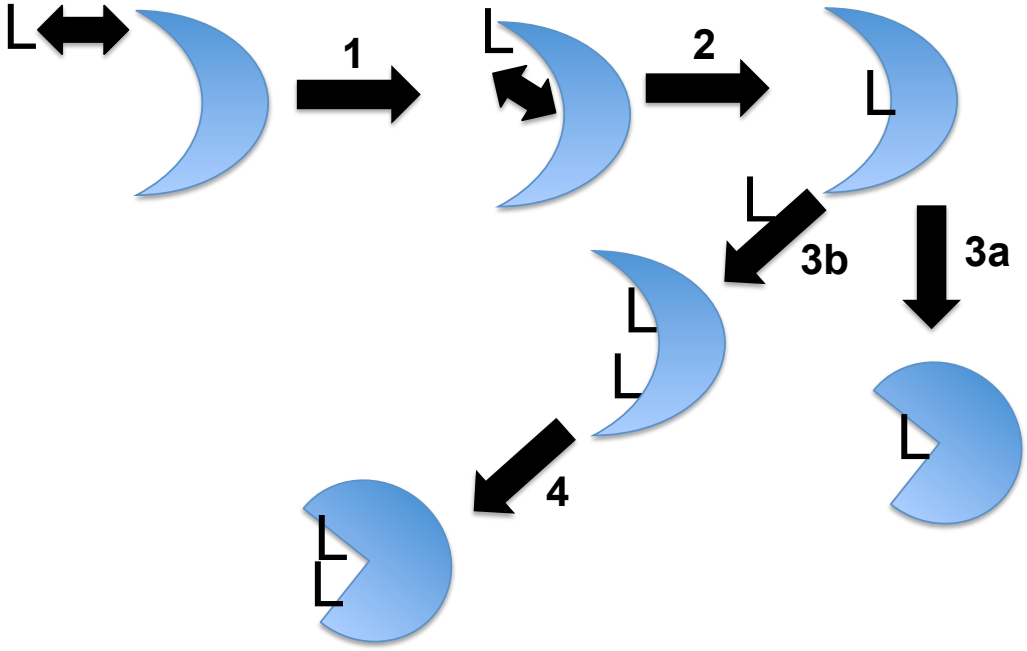

Figure 31. Proposed events in ligand binding to ferric P450 1A2. *Step 1:* The ligand L first interacts with P450 1A2 at a peripheral site, and the binding quenches the fluorescence of L (Figure 23). *Step 2*: L is translocated to the interior of the protein, where it can interact with the heme and produce the difference spectrum (Figure 21). *Step 3a*: If there is only space available for one molecule of L in the active site (e.g. αNF), a conformational change in the P450 occurs. *Step 3b*: If L is small enough for two molecules (of L) to occupy the active site (e.g. pyrene or 1-OH pyrene), a second molecule of L can enter the active site (via the same path as in Steps 1 and 2). *Step 4*: Conformational change of the P450 following occupancy with the second molecule of L.

Kinetics and Modeling—The kinetic fitting work (Figure 27) is consistent with the UV-visible results for pyrene binding (Figure 21*A*), the cooperative *v vs*. substrate concentration pattern for pyrene 1-hydroxylation (Figure 16*B*), and the time course of conversion of pyrene to 1-OH pyrene and di-OH pyrenes (Figures 10*C* and 10*D*). It should be emphasized that this is a minimum kinetic model, and the true course of the binding interaction may involve more steps, e.g. additional conformational changes or rapid steps following slow ones that may not be revealed. The scheme presented in Figure 27*A* is adequate to describe the course of the UV-visible changes seen in the Soret spectra (Figure 27*B*). Attempts to include a conformational change following binding of the first ligand were not successful, but if a step were fast enough this step would not be seen. A schematic model, presented in Figure 31, does have a step following initial binding, in which the ligand translocates into the active site. This step seems obvious but could either be fast or could be coupled with the binding of the second ligand. Following ligand binding, the two paths diverge in Figure 31. With a larger substrate, e.g. αNF, only one molecule fits, and conformational changes occur after site occupation (step *3a*). With the smaller substrate pyrene (or benzo[*a*]pyrene), a second molecule enters (step *3b*) and finally conformational changes occur with this dimer-occupied P450 (step *4*).

The kinetic model presented in Figure 27*A* is intended to be a minimal model, i.e. the simplest model that can be used to rationalize a set of data (134). The condition was used that a single model had to be capable of explaining (i) the biphasic kinetics of pyrene binding to P450 1A2 (Figure 21*C*), (ii) the sigmoidal *v vs*. substrate concentration plot for 1-hydroxylation of pyrene (Figure 16*B*), and (iii) the steady-state time course of oxidation of pyrene to 1-OH pyrene and then the di-OH pyrenes (Figures 10*C* and 10*D*),

plus be consistent with (iv) the rate of interaction of pyrene with P450 (~ 4×10^6 M^{-1} s^{-1}, Figure 23*A*), (v) the tight unimolecular binding of pyrene to P450 (Figures 20*A* and 20*C*), and (vi) tight binding of 1-OH pyrene to P450 (Figures 20*B* and 20*D*). The 6-step model presented in Figure 27*A* satisfies these criteria reasonably well. The model may contain additional steps, and a kinetic model cannot necessarily exclude all alternative possibilities. The sigmoidal nature of the fit to the *v vs*. substrate concentration data in Figure 27*C* is not ideal but nevertheless the fitted line (from DynaFit) gives a Hill plot with an *n* value of 1.81 (± 0.01) and S_{50} value of 9.9 (± 0.01) μM. A shortcoming of the modeling is the prediction of the experimentally measured steady-state level of 1-OH pyrene (Figure 27*D*). The latter could be adjusted by increasing k_4 but this change rendered *v* too fast in Figure 27*C* (*v vs*. substrate concentration). In the modeling, the ESS complex was used as the catalytically competent one, instead of SES (Figure 27*A*). In principle, either or both of these complexes could be catalytic and the mathematical solutions should be equivalent, although k_3, k_{-3}, and possibly other rate constants would need adjustment.

One deficiency of knowledge is that there is no information to discern whether a pyrene is still present in the P450 1A2•1-OH pyrene complex that forms di-OH pyrenes (Q in the modeling, Figure 27*A*). The modeling was done with the pyrene (S) still present, although a model with the pyrene removed should give similar results though having one more step (also, in the model of Figure 27*A*, the dissociation of di-OH pyrene (Q) was ignored in that Q and ESQ were considered together in Part *D*). In additional modeling (not shown), the mechanism of Figure 27*A* could be readily adapted to fit the hydroxylation of 1-OH pyrene (*v vs*. substrate concentration data, Figure 16*C*) by setting

S to represent 1-OH pyrene, P to represent di-OH pyrenes, and eliminating k_6. The issue was approached of whether a heteromeric P450•pyrene•1-OH pyrene complex could explain the observed kinetics or if a P450 1A2•1-OH pyrene complex was required. Modeling showed that a P450•pyrene•1-OH pyrene complex is catalytically competent to form di-OH pyrenes and a dimeric (1-OH pyrene)$_2$•P450 complex yielded fits to di-OH pyrene formation (Figure 27*D*) that were far too slow (> 20-fold, results not shown).

In summarizing the kinetic modeling, the major features that were cited for this model are (i) two pyrene molecules bound, (ii) catalytic activity only with two bound pyrenes, (iii) $K_{d,2} >> K_{d,1}$ and (iv) an equilibration step occurring after binding of the second pyrene. Other features are probably less critical. As mentioned earlier, the sigmoidal *v vs*. substrate concentration data could be fit with mathematical equations either having $K_{d,1} > K_{d,2}$ (132) or $K_{d,1} < K_{d,2}$ (Figure 27*A*). Only the latter is consistent with the spectral binding results (Figures 20*A* and 20*C*), and the kinetics of the change in absorbance (Figure 27*B*) fit well even at a low pyrene concentration. The same conclusion about the relative affinities of P450 3A4 for binding two testosterone molecules ($K_{d,1} < K_{d,2}$) was reached by Roberts et al. (135) using different approaches.

Structural Models—Analysis of the structural models indicated that the active site of rabbit or human P450 1A2 was only large enough for a single αNF molecule but two pyrenes could be readily accommodated (Figure 25). The αNF configuration was clearly a non-catalytic one, in that the only site of oxidation (5,6 bond) was the most distant from the iron atom (23). With pyrene, the exact orientations of the two molecules docked in the active site were uncertain. In Figure 25 (parts *B* and *C*), a slight overlap could easily be accommodated without distortion of any side chains. With some movement of the I-

helix, a complete pyrene-pyrene stack could be achieved in the models. Whether the fluorescence spectra represented a slightly overlapped pyrene pair or a low population of highly overlapped pyrenes was not known in the absence of more data.

At this point I am unable to explain the site of hydroxylation (C-1) of pyrene (as opposed to C-2 or -4), in that docking in the model is uncertain. Another point to be made is that the information available was not sufficient to make predictions of sites of oxidation of other substrates for P450 1A2. As pointed out above, even when a crystal structure is available the site most likely to be oxidized may not be predicted, e.g. (23).

The hyperbolic nature of the kinetics of oxidation of αNF and the cooperativity of pyrene and 1-OH pyrene oxidations may be rationalized in terms of the size of the P450 1A2 active site, which holds only one αNF but two of the other molecules (Figure 25). However, the ability to predict the cooperative behavior of other ligands is still limited. One can ask the question of why phenacetin *O*-deethylation is apparently not cooperative (at least for human P450 1A2) (136). Why are the homotropic cooperativity patterns of pyrene and the 1-alkoxy-4-nitrobenzenes rather opposite in their appearance (Figure 16*B* of this work and (47))? One possible explanation may be that the results are related to the flat, planar character of the polycyclic aromatic hydrocarbons, in that pyrene and benzo[*a*]pyrene both showed homotropic cooperativity (Figures 10*B* and 26).

Cooperativity—Although pyrene 1-hydroxylation is highly cooperative with rabbit (Figure 16*B*) and human P450 1A2 (Figure 17), the related enzymes (human) P450 1A1 and 1B1 have been reported to exhibit classical hyperbolic behavior (102). P450 3A4-catalyzed pyrene 1-hydroxylation has been reported to show cooperative behavior of

a type opposite to that shown here (Figure 16*B*), i.e. described with a low K_m/high K_m fit (not sigmoidal) (87), and the patterns were altered in the presence of cytochrome b_5. Benzo[*a*]pyrene, which contains one more aromatic ring than pyrene, has been studied extensively in the context of chemical carcinogenesis (137). The docking studies (Figure 25*B* and 25*C*) suggested that two benzo[*a*]pyrene molecules could readily fit into the P450 1A2 active site. A study of benzo[*a*]pyrene hydroxylation, using a fluorimetric assay (which detects mainly 3-hydroxylation (101)) also showed cooperative behavior (Figure 26). Surprisingly, examination of the literature did not yield any plots of the rate of benzo[*a*]pyrene oxidation as a function of substrate concentration by rabbit or other P450 1A2 enzymes.

The question can be raised as to how much the results of this cooperativity work with P450 1A2 extend to other P450s that have been shown to have weaker cooperative behavior (e.g., P450s 3A4, 2C9, and 2B6). Interestingly, the active site of P450 3A4 is known to be very large (79, 80, 88). Interactions among multiple ligands have been invoked as a mechanism for cooperativity with P450 3A4 (69), and stronger fluorescence evidence for the presence of pyrene excimers in the protein has been presented (125). However, in the 1-hydroxylation of pyrene by P450 3A4 only weak homotropic cooperativity was observed, with an apparent Hill coefficient (n) of ~1.7 in some cases, i.e. with cytochrome b_5 (87, 138). One possibility is that some cases of positive and negative cooperativity in the P450s can be explained by models such as that described in Figure 27*A* and the variation in the degree of cooperativity can be understood in terms of the extent of the differences between the k_{cat} and K_d (or at least K_m) values for activity

with substrate monomer and dimer, e.g. in this case a 100-fold difference between $K_{d,1}$ and $K_{d,2}$ in the model yielded an apparent n value of 1.8 in the Hill plot (*vide supra*).

Another point to be made is that reports of weak cooperativity must be viewed cautiously. In cases of weak cooperativity, the results are heavily dependent upon the accurate measurement of experiments that use low concentrations of substrate (or ligand). These measurements are the most sensitive to error. Another issue is that points obtained with low substrate concentrations are sensitive to depletion of substrate, product inhibition, etc. and, in this laboratory's own experience, artifactual plots can easily be obtained under conditions of too prolonged incubation. In the literature in this field it is not uncommon to find plots with few or even no points at less than one-half maximal activity (or signal) and subsequent deconvolution of limited data to complex models with three ligands etc.

Conclusions—In this chapter, what appears to be the most cooperative of P450 reactions characterized to date is reported. The hypothesis that cooperative behavior in P450 1A2 catalysis was not limited to a small class of substrates (1-alkoxy-4-nitrobenzenes) and that such behavior might have a structural basis was proved in the pyrene studies. Oxidation of an important pollutant was shown to be cooperative, and structural modeling indicated this was related to the ability to dock two pyrene molecules in to the P450 1A2 active site allowing one to exert cooperative behavior on the oxidation of the other. A two-step sequential reaction catalyzed by P450 1A2 to generate 1-OH pyrene and subsequent di-OH pyrenes is described. The results are consistent with a kinetic model for selective catalytic activity for two substrate molecules. Structural

models support the hypothesis that hyperbolic oxidation of αNF is related to single occupancy of the active site as opposed to the highly cooperative kinetics seen with two substrate molecules in the active site. The kinetics of interactions of the enzyme with several ligands are multiphasic, with slow steps, and the kinetics of interaction with pyrene can be fit to a two-ligand kinetic model. Some of the findings with this highly cooperative P450 system may extend, with modification, to other cooperative P450s.

CHAPTER III

COOPERATIVITY OF CYTOCHROME P450 1A2: INTERACTIONS OF 1,4-PHENYLENE DIISOCYANIDE AND 1-ISOPROPOXY-4-NITROBENZENE[6]

Introduction

The P450s involved in drug metabolism have been studied extensively. One of the phenomena that is still not understood well is ligand cooperativity. Heterotropic cooperativity (63, 133), in which one ligand stimulates catalysis involving another ligand (substrate), was first observed > 35 years ago (65, 70, 139). Homotropic cooperativity, recognized more recently (68, 69), refers to several types of non-hyperbolic plots of *v vs.* substrate concentration for a single substrate.

Much of the research on P450 cooperativity has been directed towards several P450s now known to have large substrate binding sites, i.e. P450s 3A4, 2C8, and 2C9 (79, 80, 140-142). P450 1A2, however, has a smaller active site (23) and cooperativity associated with this enzyme was described in Chapter II (32) and in previous work in this laboratory (47). Homotropic cooperativity was seen in the *O*-dealkylation of 1-alkoxy-4-nitrobenzenes, with biphasic *v vs.* substrate concentration plots which were characterized with two sets of k_{cat} and K_m values, with $K_{m,1} < K_{m,2}$ (47). In that study, heterotropic cooperativity for ligand binding was observed in the interaction between 1-alkoxy-4-nitrobenzenes and an isocyanide, $Ph(NC)_2$.

---

[6] This project, including manuscript writing, was done in collaboration with Drs. Emre M. Isin, Robert L. Eoff, and F. Peter Guengerich.

Isocyanides have a long history in the study of hemoproteins, going back to work in 1929 with hemoglobin and methyl isocyanide (143). Isocyanides were also used extensively in some of the early research on P450 (144-146); the carbon atom is liganded directly to either ferric or ferrous iron in the P450 [33] and yields a Type II Soret difference spectrum distinctly different than that often generated by the addition of substrates (low- to high-spin iron transition, Type I). Titrations of rabbit P450 1A2 with 1-alkoxy-4-nitrobenzenes and $Ph(NC)_2$ led to the conclusion that one ligand could enhance the binding of the other, indicative of multiple ligand occupancy as opposed to competition of the two ligands for a single site (47).

In this chapter, several aspects of the interaction of $Ph(NC)_2$ with rabbit P4540 1A2 were studied, including kinetics of binding, conformational changes of the enzyme (as detected by CD spectroscopy), and effects on rates of P450 reduction and catalysis of P450 1A2 reactions. Modeling of the ligands was done using the published crystal structure of the human P450 1A2-αNF complex (23), which is now available as a template. The cooperative interactions of the 1-alkoxy-4-nitrobenzenes and $Ph(NC)_2$ are rather different that those recently described for P450 1A2 and some polycyclic hydrocarbons, as discussed in Chapter II (32).

Experimental Procedures

Chemicals—$Ph(NC)_2$ was purchased from Aldrich Chemical Co. (Milwaukee, WI) and recrystallized from hexanes. $(CH_3)_2CH$-O-$PhNO_2$ was synthesized as previously described (47) and recrystallized from a mixture of C_2H_5OH and H_2O.

Enzymes—Rabbit P450 1A2 and recombinant rat NADPH-P450 reductase were obtained as described in Chapter II.

Assays of Product Formation—Incubations were performed under the same conditions described in Chapter II, except either αNF (14 or 35 μM), $(CH_3)_2CH$-O-$PhNO_2$ (50 or 700 μM), or pyrene (35 or 140 μM) were used as substrates. In the case of aniline, slight modifications in concentrations were made (3.3 μM P450 1A2, 6.6 μM NADPH-P450 reductase, 200 μM L-α-dilauroyl-*sn*-glycero-3-phosphocholine, and 8 mM aniline (144)). Incubations were done for 20 min in the case of the αNF, aniline, and $(CH_3)_2CH$-O-$PhNO_2$ experiments. αNF 5,6-epoxidation was analyzed by HPLC as described in Chapter II (32, 104). $(CH_3)_2CH$-O-$PhNO_2$ *O*-dealkylation was monitored spectrophotometrically immediately after adding the NADPH-regenerating system (release of 4-nitrophenol, ΔA_{400}) using the extinction coefficient of 4-nitrophenol, ε_{400} = 12 mM^{-1} cm^{-1} (47). Rates of aniline 4-hydroxylation were estimated using a colorimetric procedure (147), utilizing an extinction coefficient for 4-aminophenol (generated with a standard curve), ε_{630} = 10 mM^{-1} cm^{-1} (148). Pyrene 1-hydroxylation was analyzed by HPLC/fluorescence by slight modification of a procedure described elsewhere and in Chapter II (32, 105).

Spectroscopic Measurements—Steady-state UV-visible spectroscopy, steady-state fluorescence, steady-state CD measurements, and stopped-flow UV-visible and fluorescent measurements were done using instruments described in Chapter II. Stopped-flow CD measurements were made with a modified Applied Photophysics SX-17MV

instrument (Applied Photophysics, Leatherhead, UK), kindly made available by R. N. Armstrong (Vanderbilt University). Anaerobic studies were done as described in Chapter II.

Homology Model Building—As in Chapter II, a crystal structure of a human P450 1A2-αNF complex (23) was used as the template to develop a homology model of rabbit P450 1A2 utilizing the automated homology modeling tool SWISS-MODEL (110). Coordinate files for molecules of $(CH_3)_2CH$-O-$PhNO_2$ and $Ph(NC)_2$ were generated using the Dundee PRODRG2 server (111) and manually docked into the binding cavity (replacing αNF) using Turbo Frodo (112). Simulated annealing was then performed with the program CNS Solve 1.1 using the input file model Anneal (113, 114). The heme group was fixed during simulated annealing (energy-minimized models were not adjusted following annealing).

Results

Kinetics of Ligand Binding to Ferric P450 1A2—Binding of the Type II ligand $Ph(NC)_2$ to ferric P450 1A2 was slow (Figure 32), with estimated rates of 0.07 and 0.01 s^{-1} using a bi-exponential fit, at a final ligand concentration of 100 μM. Binding of the substrate $(CH_3)_2CH$-O-$PhNO_2$ (data not presented) was also biphasic and relatively slow, with rates of 2.9 and 0.08 s^{-1} measured at a substrate concentration of 10 μM (32).

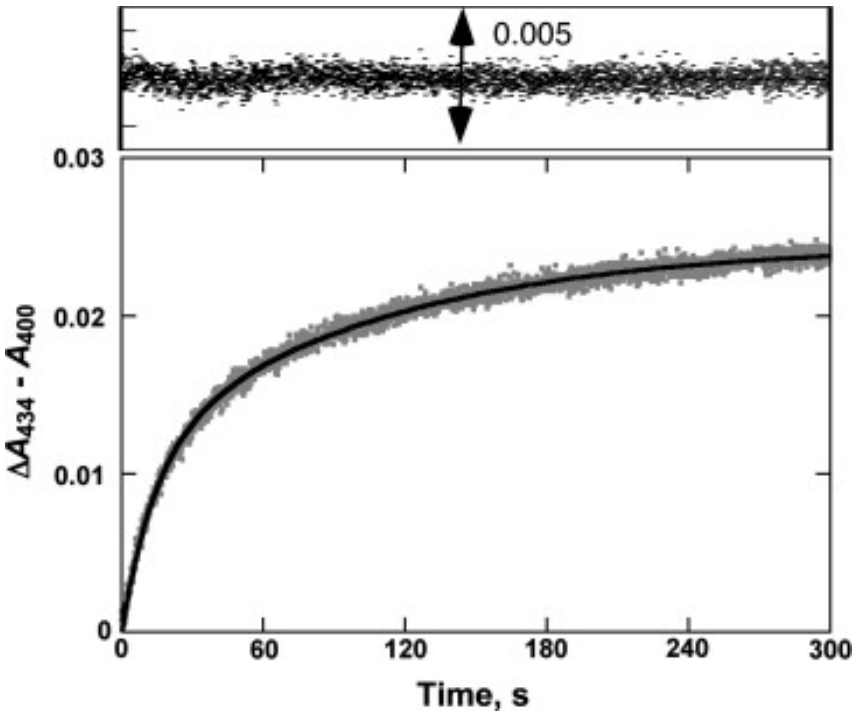

Figure 32. Pre-steady-state kinetics of $Ph(NC)_2$ binding to ferric P450 1A2. The kinetic trace ($\Delta A_{434}–A_{400}$) obtained for $Ph(NC)_2$ (100 μM) binding to P450 1A2 (1 μM) was fit to a bi-exponential plot with rates of 0.07 and 0.01 s^{-1}.

Kinetics of Binding of $Ph(NC)_2$ to Ferrous P450 1A2—The ferrous P450-$Ph(NC)_2$ complex had a strong absorption maximum at 455 nm, typical of isocyanide complexes (146), which can be used for kinetic analysis of binding. The binding of $Ph(NC)_2$ to ferrous P450 was triphasic, with a rapid burst followed by a biphasic change that accounted for most of the absorbance increase (Figures 33*A* and 33*B*). When the rates were measured as a function of $Ph(NC)_2$ concentration, the fast phase yielded an apparent rate constant of 1.4×10^6 M^{-1} s^{-1} (Figure 33*C*) but the rates of the latter two steps were rather invariant with the concentration (Figure 33*D*).

CD and Fluorescence Spectra—The binding of either $(CH_3)_2CH$-O-$PhNO_2$ or $Ph(NC)_2$ to P450 1A2 induced changes in the CD spectrum (Figure 34). The far-UV changes are indicative of a change in the conformation of the protein and consistent with a decrease (based on $[\theta]_{220}$) in α-helicity (126).

Changes in the tryptophan fluorescence of P450 1A2 have been observed upon binding of 1-alkoxy-4-acetanilides (149). An attempt was made to monitor the binding of $Ph(NC)_2$ to P450 1A2 using changes in P450 tryptophan fluorescence, but no changes were observed (for tryptophan or tyrosine).

Effect of $Ph(NC)_2$ on Catalytic Activity of P450 1A2—In the early literature on P450, diethylisocyanide was reported to stimulate the oxidation of aniline in rabbit liver microsomes (144, 146). The enhanced spectral changes in substrate binding with the presence of $Ph(NC)_2$ (47) raised the possibility of stimulation of P450 1A2 activity.

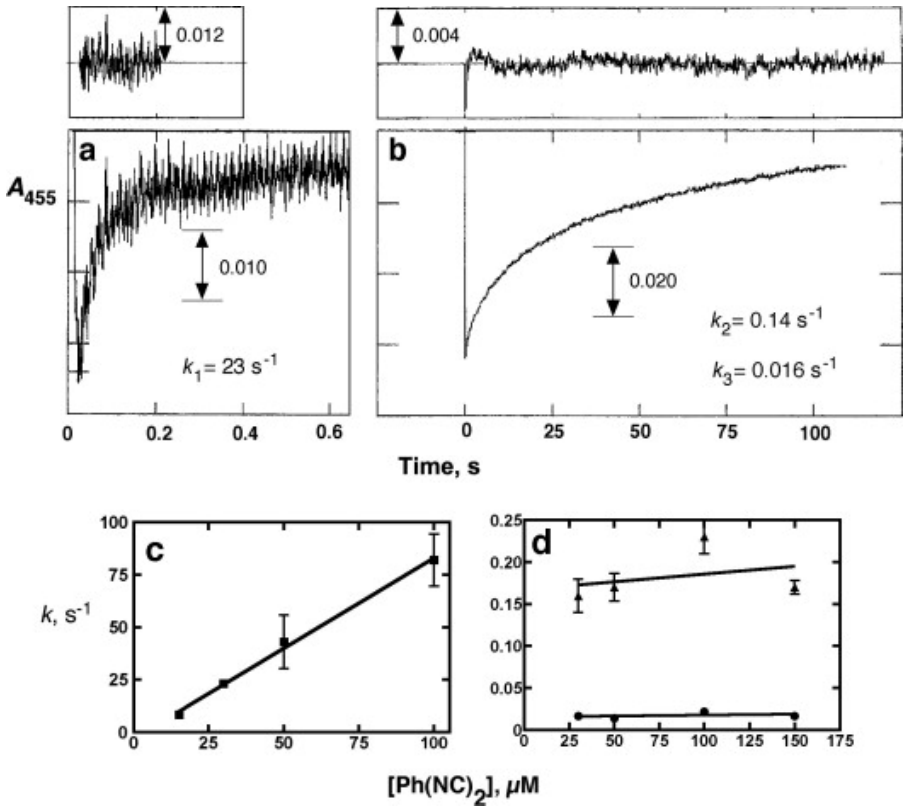

Figure 33. Pre-steady-state kinetics of ligand binding to ferrous P450 1A2. P450 1A2 (1.0 μM final concentration following mixing) was reduced anaerobically in the presence of 0.25 μM NADPH-P450 reductase (and 75 μM L-α-dilauroyl-*sn*-glycero-3-phophocholine and an NADPH-generating system (101). *A*, First portion of reaction with 30 μM (final concentration) of anaerobic $Ph(NC)_2$. The initial part of the trace was fit to a single exponential of $k_1 = 23 \pm 0.2$ s^{-1}. *B*, Latter phases of the reaction were fit to a bi-exponential plot with $k_2 = 0.14 \pm 0.01$ s^{-1} and $k_3 = 0.016 \pm 0.003$ s^{-1}. *C*, Rates of k_1 were determined at varying concentration of $Ph(NC)_2$ and fit to a plot, with an intercept near 0 and a calculated second-order rate of 1.4 ($\pm$ 0.1) $\times$ 10^6 M^{-1} s^{-1}. *D*, Values of k_2 and k_3 as a function of $Ph(NC)_2$ concentration.

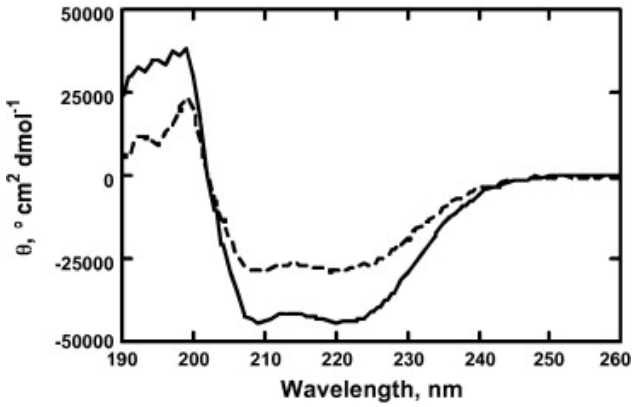

Figure 34. CD spectra of $Ph(NC)_2$ binding to rabbit P450 1A2. The solid line (—) is a scan with 0.41 μM P450 1A2 alone and the dotted line (----) is the scan following the addition of $Ph(NC)_2$ (40 μM), followed by a 15 min incubation. The cuvette pathlength was 1 mm and A_{220} was < 0.2 in both cases.

However, $Ph(NC)_2$ inhibited $(CH_3)_2CH$-O-$PhNO_2$ *O*-dealkylation and aniline 4-hydroxylation (Figure 35), as well as αNF 5,6-epoxidation and pyrene 1-hydroxylation (results not shown).

$Ph(NC)_2$ was not converted to any products detected by general HPLC profiling by rabbit P450 1A2 (< 0.01 nmol of any product min^{-1} (nmol P450)$^{-1}$, assuming a similar extinction coefficient).

Effect of $Ph(NC)_2$ on Rate of P450 1A2 Reduction—One of the interesting features of isocyanides is that, in contrast to other Type II P450 ligands, they bind to both ferric and ferrous P450 heme and the complexes can be discerned spectrally (Figure 36). It was possible to examine the effect of $Ph(NC)_2$ on the rate of reduction of P450 1A2, which was a 10-fold attenuation (Figure 36). However, even the attenuated rate (of heme reduction) is considerably faster than rates of substrate oxidation, and the inhibition of catalytic activity (Figure 35) is not the result of only the decreased reduction rate. To my knowledge, a direct examination of the rates of electron transfer from NADPH-P450 reductase to a P450 with its heme iron liganded to a Type II ligand has not been determined previously, mainly because many ligands have similar spectra in the ferric and ferrous states (e.g., cyanide or azoles) and use of CO as a trap would require a dissociation step.

Fitting of Ligands in a Homology Model of P450 1A2—The possibility of simultaneous binding of $(CH_3)_2CH$-O-$PhNO_2$ and $Ph(NC)_2$ in the active site of rabbit

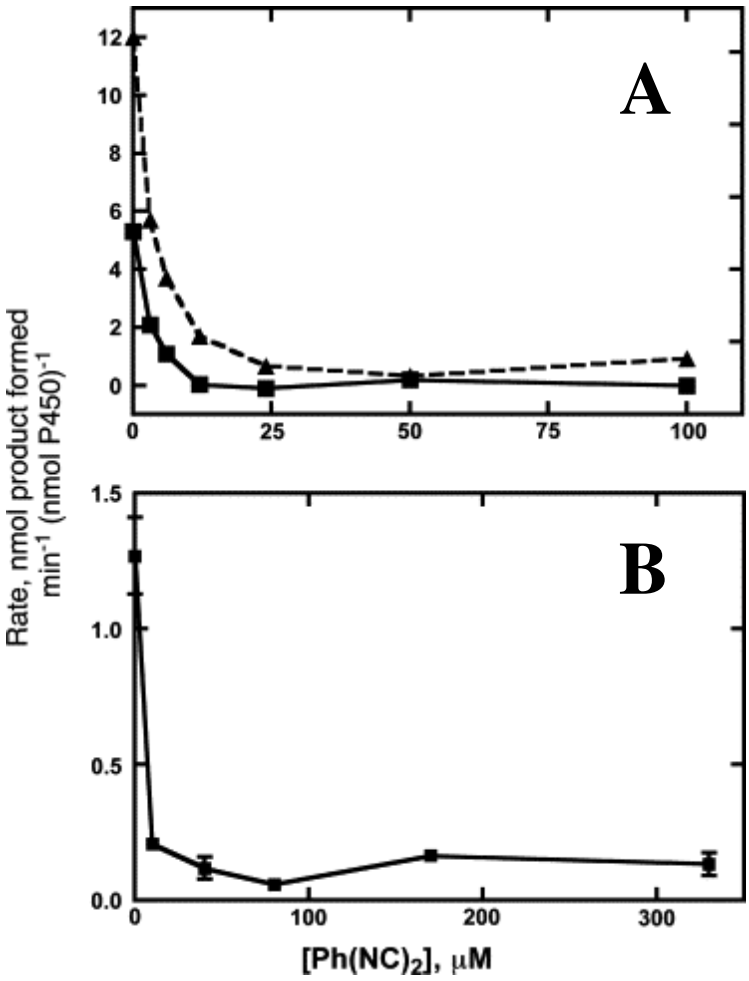

Figure 35. Inhibition of P450 1A2 catalytic activity. *A*, $(CH_3)_2CH$-O-$PhNO_2$ *O*-dealkylation, as measured by absorbance at 400 nm. The data were fit to a straight line to determine the amount of 4-nitrophenol formed per min. The dotted line (----) shows the rate of *O*-dealkylation of 700 μM $(CH_3)_2CH$-O-$PhNO_2$ and the solid line (—) line shows the rates measured with 50 μM $(CH_3)_2CH$-O-$PhNO_2$. *B*, Aniline 4-hydroxylation. Formation of *p*-aminophenol (substrate concentration of 8 mM aniline) was monitored by measuring absorbance at 630 nm after derivatization.

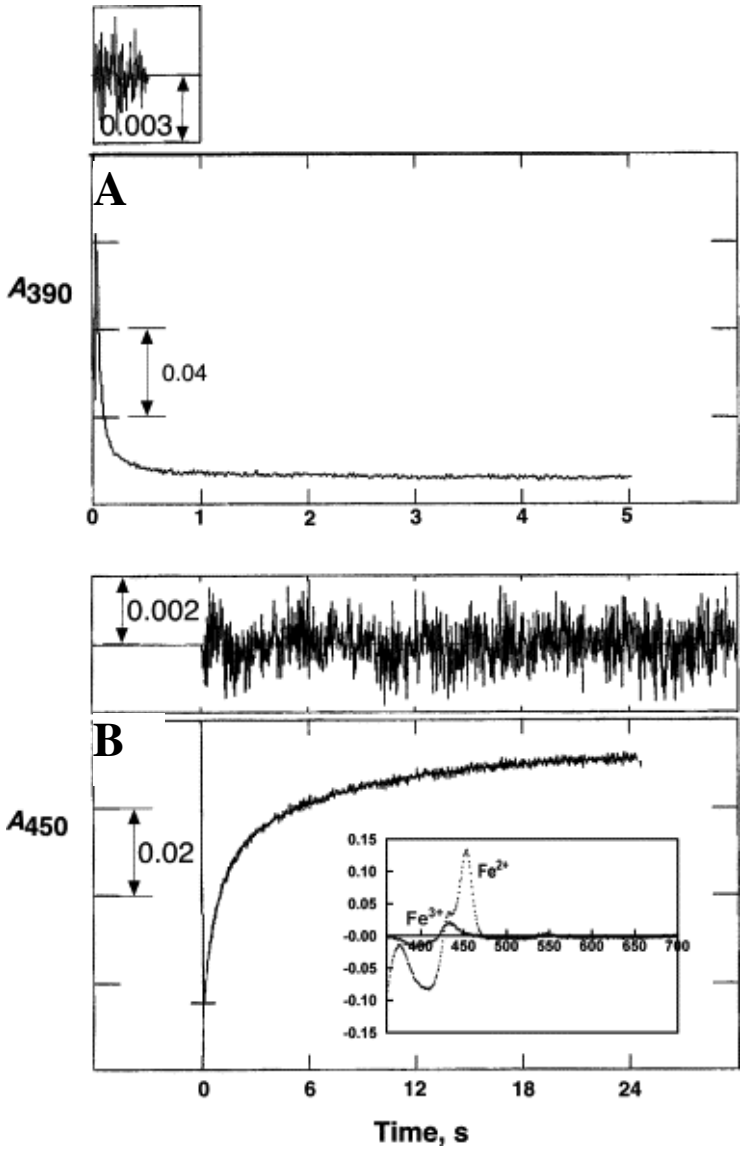

Figure 36. Effect of $Ph(NC)_2$ on the rate of enzymatic reduction of P450 1A2. All experiments included 2.0 μM P450 1A2, 4.0 μM NADPH-P450 reductase, and 75 μM L-α-dilauroyl-*sn*-glycero-3-phosphocholine, with the reaction initiated by the addition of 100 μM NADPH (23 °C). *A*, Reduction in absence of ligands, measured at 390 nm. The first part of the trace was fit to a single exponential with a rate of 25 (± 1) s^{-1}. *B*, Reduction in the presence of 100 μM $Ph(NC)_2$, measured at 455 nm. The data were fit to a bi-exponential plot with $k_1 = 1.3 \pm 0.02$ s^{-1} and $k_2 = 0.14 \pm 0.002$ s^{-1}. Residuals traces for the fits are shown in both parts *A* and *B*. The inset in Part *B* shows the difference spectra generated by the addition of 100 μM $Ph(NC)_2$ to ferric (peak near 430 nm, trough at 395 nm) and ferrous (peak at 455 nm, trough at 405 nm) P450 1A2 (2.0 μM).

P450 1A2, hypothesized earlier (47), was examined by docking the ligands into the active site of a homology model based on a human P450 1A2-αNF complex (23) (Figure 37*A*). As with pyrene in Chapter II (32), both molecules can easily fit into the active site of the model, regardless of which ligand is bound closest to the heme group (Figure 37*B* and 37*C*). Except for the disruption of the F-helix, which was observed in the human P450 1A2-αNF structure (23), none of the α-helices that comprise the active-site pocket were disrupted by the simultaneous presence of $(CH_3)_2CH$-O-$PhNO_2$ and $Ph(NC)_2$.

Discussion

The previous conclusion that both a 1-alkoxy-4-nitrobenzene and a $Ph(NC)_2$ molecule could co-occupy the active site of P450 1A2 (47) is consistent with the protein model (Figure 37). The model is considered reliable in that the rabbit P450 1A2 sequence has high identity (75%) with the human P450 1A2 sequence (128) and the two proteins have many similar functional characteristics (96). Although the protein used in these studies was isolated from rabbit liver microsomes, there was no evidence of another P450 or other impurity (i.e., SDS-PAGE), and previous work with recombinant rabbit P450 1A2 showed the major cooperative features of the protein purified from liver (47). The kinetics of binding of $Ph(NC)_2$ were different for ferric and ferrous P450 (Figures 32 and 33). Binding to ferrous P450 1A2 showed a fast phase (Figure 33*A*), followed by what appear to be two much slower phases (Figure 33*B*). The rate of the fast phase increased with ligand concentration (Figure 33*C*), while the two slower steps were rather invariant with the concentration (Figure 33D). With ferric P450 (Figure 32), only a slow biphasic change was seen, and the rates are similar to those of the second two steps with the

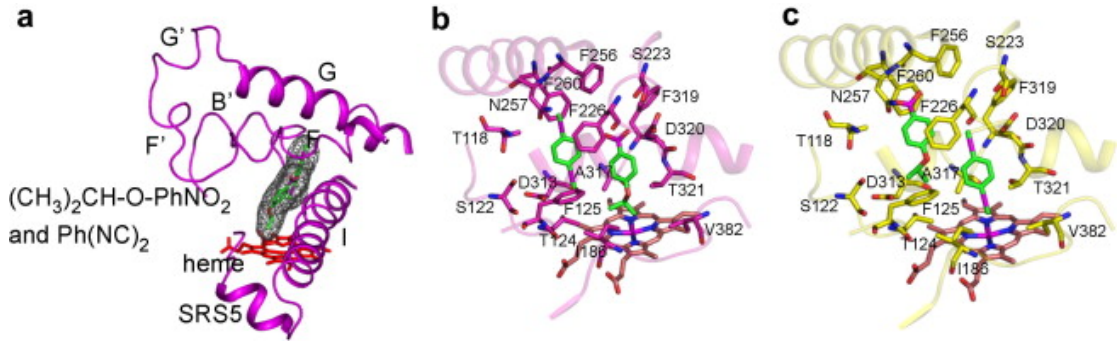

Figure 37. Docking of ligands into a homology model of rabbit P450 1A2. *A*, Rabbit P450 1A2 homology model (magenta ribbon) with heme group (red sticks) and $(CH_3)_2CH$-O-$PhNO_2$ plus $Ph(NC)_2$ (sticks with space-filling mesh). SRS5: Substrate recognition sequence 5 (129). *B*, Active-site of rabbit P450 1A2 homology model (magenta ribbon) with heme group (sticks) and $(CH_3)_2CH$-O-$PhNO_2$ plus $Ph(NC)_2$ (sticks), with $(CH_3)_2CH$-O-$PhNO_2$ modeled close to heme iron in the most productive mode and side-chains highlighted. *C*, Active-site of rabbit P450 1A2 homology model (yellow ribbon) with heme group (sticks) and $Ph(NC)_2$ plus $(CH_3)_2CH$-O-$PhNO_2$ (sticks), with $Ph(NC)_2$ liganded to heme iron and side chains highlighted.

studies with the reduced enzyme (Figures 33*B* and 33*D*). The concentration dependence of the rates of the two steps in Figure 32 was not examined. The similarity of the rates of the two slow steps in the ferrous and ferric reactions is not due to oxidation of the ferrous to the ferric state because the absorbance wavelength used (455 nm) is only indicative of binding to the ferrous iron (Figure 36*B*). The conclusion is that the fast rate constant with the ferrous enzyme (1.4×10^6 M^{-1} s^{-1}) might represent the second-order "on" rate (although this is somewhat slow (46)) and the slower rates observed with both ferric and ferrous P450 represent conformational events in changing the protein to achieve the final spectrum. It should be emphasized that the multiphasic kinetics of ligand binding do not constitute any evidence for multiple ligand occupancy, in the absence of other data.

The homology model (Figure 37) is considered reliable, at least for a ground state P450 1A2-substrate complex (23). The active site (estimated size 375 $Å^3$ (23)) is large enough to fit only one αNF molecule (23) or two pyrenes as described in Chapter II (32) but either two molecules of $(CH_3)_2CH$-O-$PhNO_2$, two molecules of $Ph(NC)_2$, or one of each ($(CH_3)_2CH$-O-$PhNO_2$, $Ph(NC)_2$) (Figure 37) can be accommodated in the active site. It is proposed that the co-occupancy by two molecules of $(CH_3)_2CH$-O-$PhNO_2$ may be responsible for the two-k_{cat}, two-K_m behavior ("negative cooperativity") observed for $(CH_3)_2CH$-O-$PhNO_2$ *O*-dealkylation (47). Fitting of one molecule each of $(CH_3)_2CH$-O-$PhNO_2$ and $Ph(NC)_2$ into the model of the active site (Figure 37) is consistent with the previous conclusions based on comparisons of spectral interactions of the ligands (47). This interaction leads to apparently enhanced binding of $(CH_3)_2CH$-O-$PhNO_2$ in the presence of $Ph(NC)_2$ (and vice-versa) (47) but results in inhibition of catalytic activity (Figure 35), even when the substrate is $(CH_3)_2CH$-O-$PhNO_2$ (Figure 35*A*). It is proposed

that co-occupancy of the P450 1A2 active site is a common feature of numerous small substrates (and other ligands) but the nature of cooperative behavior is highly ligand dependent (32, 47). Apparently loading the active site with two molecules of $(CH_3)_2CH$-O-$PhNO_2$ moves the substrate into a less favorable conformation for oxidation, explaining the attenuated catalytic efficiency at higher substrate concentrations (47). The interaction of P450 1A2 with $Ph(NC)_2$ increases the spectrally detectable binding of $(CH_3)_2CH$-O-$PhNO_2$ to P450 1A2 (47) but apparently does so in a way that attenuates catalytic activity (Figure 35). In this laboratory's earlier work (47) with this isocyanide and substrate, the titration results provided evidence that each compound could enhance the binding of the other. It is postulated that one factor in binding of $Ph(NC)_2$ is the interaction of the phenyl ring somewhere in the active site. One option for binding is that shown in Figure 37*B*, in which the substrate ($(CH_3)_2CH$-O-$PhNO_2$) is bound near the iron atom, in juxtaposition for oxidation at the CH position. This configuration may be possible but apparently a scheme such as that shown in Figure 37*C* is more dominant, as reflected in the inhibition (Figure 35). A major point of the paper is that one can get cooperativity in binding of ligands but that this does not necessarily translate to catalytic activity, e.g. (150).

In summary, I have been able to extend earlier observations on the heterotropic cooperativity of rabbit P450 1A2 (47). The modeling is clearly consistent with the previously presented proposal that one molecule each of $Ph(NC)_2$ and $(CH_3)_2CH$-O-$PhNO_2$ can co-occupy the active site. However, the heterotropic cooperativity yields enhancement of substrate binding but not an increase in catalytic activity. Apparently the juxtaposition of the 1-alkoxy-4-nitrobenzene imposed by the $Ph(NC)_2$ ligand is

unfavorable for catalysis in this case, although the nature of such an interaction was not revealed in the modeling.

CHAPTER IV

KINETIC ANALYSIS OF THE THREE-STEP STEROID AROMATASE REACTION OF HUMAN CYTOCHROME P450 19A1

Introduction

P450 19A1 is responsible for the conversion of androgens (andro, testosterone, and 16α-hydroxytestosterone) to estrogens (estrone, 17β-estradiol, and estriol, respectively) in a sequential, three-step reaction (Figure 7). This conversion, first identified in 1959 (151), requires three molecules each of NADPH and O_2 and proceeds through two relatively stable intermediates, 19-hydroxy and 19-aldehyde compounds, before the final aromatization step. There has been considerable debate over the chemistry of the third step, and two mechanisms are currently favored. In the first model, the ferric peroxide form of the P450 ($FeOO^{-}$, Figure 4) attacks the aldehyde, followed by heterolytic cleavage of the peroxide bond and the transfer of the 1β proton of the steroid to the heme to generate a ferrous hydroxy intermediate, with the loss of formic acid (152, 153). In a second postulated mechanism, a nonenzymatic conversion of the 19=O andro intermediate to a *gem*-diol (or direct hydroxylation of the alcohol intermediate to form the *gem*-diol) is followed by an aromatization catalyzed by the "Compound I" form of P450 (formally FeO^{3+}), which removes a hydrogen at the 1β position on the steroid (154). Following a transfer of an electron from the steroid A ring to the iron, the ferric hydroxy intermediate ($FeOH^{3+}$) removes a hydrogen from the *gem*-diol, facilitating the loss of this carbon as formic acid (154).

Controversy exists regarding the processive or distributive characteristic of the sequential steps catalyzed by P450 19A1, as summarized by Bednarski and Nelson (155). Steady-state time course reactions of the turnover of andro by microsomes suggested linear formation of estrone sequentially from the two intermediates that freely dissociate (39, 40). It has also been proposed that the third step proceeds at a different active site than the first two oxidations, which would perhaps support intermediate dissociation (156). Further studies with inhibitors that mimic both the 19-OH andro and 19=O andro intermediates suggested P450 19A1 is processive (41) and indicated that only one active site exists (155). While there is now agreement that catalysis occurs at one active site and must proceed through the 19-OH andro and 19=O andro intermediates (157), it remains unclear whether these intermediates dissociate over the course of the reaction.

A crystal structure of P450 19A1 (bound to andro) has recently been solved, revealing a relatively small active site that is well suited to accommodate andro and arguing against the existence of multiple active sites (24). P450 19A1 has wide tissue distribution (including placenta, ovaries, testes, and adipose tissue), and expression is associated with estrogen-dependent breast cancer (~ 75% of breast cancer diagnoses) (158). Aromatase inhibitors, available since the 1970s, have been successful in treating post-menopausal women with this type of cancer (159). While much of the focus has been on characterizing the kinetics of P450 19A1 in the context of aromatase inhibitors, fewer studies have probed native substrates. Although many steady-state parameters for the conversion of andro to estrone have been published (51, 52, 55, 58, 61), similar steady-state studies on the intermediates are limited (55). Further, to my knowledge, no

transient-state kinetic studies are available that determine the individual rate constants of the three-step sequential reaction catalyzed by P450 19A1.

One of the greatest obstacles in the study of P450 19A1 has been heterologous expression and purification. Almost all kinetic and structural work (24, 50-53) has utilized P450 19A1 purified from human placenta, which requires access to tissue and precludes mutagenesis approaches. Heterologous expression has been primarily limited to baculovirus-infected insect cells (58, 59), although P450 19A1 expression in *E. coli* has been reported (60-62).

In this chapter, a reasonably straightforward and robust protocol for the heterologous expression and purification of P450 19A1 in *E. coli* is given. Using global fitting of a variety of both steady-state and pre-steady-state kinetic data, I developed a minimal kinetic model of P450 19A1 turnover, which includes individual rate constants for the three-step reaction and indicates a distributive mechanism.

Experimental Procedures

Chemicals—Andro, 19-OH andro, 19=O andro, and estrone were purchased from Steraloids (Newport, RI), and all radiolabeled steroids were purchased from PerkinElmer (Waltham, MA). Protocatechuate and protocatechuate dioxygenase were purchased from Sigma (St. Louis, MO).

P450 19A1 cDNA Manipulation—The P450 19A1 cDNA was optimized for *E. coli* translation and formatted into overlapping oligonucleotides using the program

DNAWorks (160) (Figure 38). Oligonucleotides were purchased from Invitrogen (Carlsbad, CA) and underwent polymerase cycling assembly to generate two synthons that could be joined through a unique BsrGI restriction enzyme cut site. After ligation of the synthons, the cDNA was inserted into a TOPO vector (Invitrogen) and sequence errors were corrected using a QuikChange Multi Site-Directed Mutagenesis Kit (Stratagene, Cedar Creek, TX). PCR was used to generate the modified *N*-terminal sequence (Figure 39) and to add a *C*-terminal hexa-histidine tag in the P450 19A1 cDNA. Finally the cDNA was inserted into the pCW expression vector.

P450 19A1 Expression—TOP 10 competent cells (Invitrogen) were transformed with the P450 19A1 cDNA, and colonies were used to inoculate 50 ml of TB media (supplemented with ampicillin (100 μg/ml)). After overnight shaking in an incubator at 37 °C (ATR Multitron, Laurel, MD), 2.8-l Fernbach flasks containing 1.0 l of TB media (supplemented with ampicillin (100 μg/ml), thiamine (340 μg/ml), and a trace element solution) (161) were inoculated with 10 ml of culture. After an OD_{600} of 1-1.2 was reached (about 3.5 h, 37 °C, 250 rpm), IPTG (1 mM) and δ-aminolevulinic acid (1 mM) were added, and the cultures were incubated for 42 h at 28° C (150 rpm).

P450 19A1 Purification—The cells from the 1.0-l cultures were pelleted (5000 × *g*, 20 min), decanted, and then resuspended in Buffer A (100 mM Tris chloride buffer (pH 7.6 at 4 °C) containing 500 mM sucrose and 0.5 mM EDTA) (15 ml/g cells). All subsequent steps were at 0-4 °C. Following lysozyme treatment, a volume of H_2O (equal to the volume of Buffer A) was added, and the preparation was incubated on ice

A

```
ATGGCCAAAAAAACCTCTTCTAAAGGTCGTAACTACGAAGGTACTTCATC -50-
TATCCCGGGTCCTGGTTACTGCATGGGCATCGGTCCGCTGATCTCTCACG -100-
GTCGTTTCCTGTGGATGGGTATTGGTTCTGCGTGCAACTACTACAACCGT -150-
GTTTACGGCGAATTCATGCGTGTTTGGATCTCTGGCGAAGAAACCCTGAT -200-
TATCTCTAAGTCCAGCTCTATGTTCCACATCATGAAACACAACCATTACT -250-
CCTCTCGTTTCGGCTCTAAACTGGGTCTGCAGTGCATTGGTATGCACGAA -300-
AAAGGTATCATCTTCAATAACAACCCGGAGCTGTGGAAAACCACCCGTCC -350-
GTTCTTTATGAAAGCGCTGTCTGGTCCGGGTCTGGTTCGTATGGTTACCG -400-
TTTGCGCTGAATCTCTGAAAACCCACCTGGACCGTCTGGAAGAAGTCACC -450-
AATGAGTCCGGTTATGTTGACGTTCTGACCCTGCTGCGTCGTGTTATGCT -500-
GGACACCTCCAACACCCTGTTCCTGCGTATCCCGCTGGACGAATCTGCTA -550-
TCGTTGTTAAAATCCAGGGTTATTTCGACGCGTGGCAGGCGCTGCTGATC -600-
AAGCCGGACATTTTCTTCAAAATTTCCTGGCTGTACAAAAAGTACGAAAA -650-
GTCTGTTAAAGACCTGAAGGACGCGATTGAAGTTCTGATTGCGGAGAAGC -700-
GTCGTCGTATCAGCACCGAAGAAAAACTCGAAGAGTGCATGGACTTTGCG -750-
ACCGAGCTGATCCTGGCGGAAAAACGTGGTGACCTGACCCGTGAAAACGT -800-
TAACCAGTGTATCCTCGAAATGCTGATCGCGGCACCGGACACCATGAGCG -850-
TTTCTCTGTTCTTCATGCTGTTCCTCATCGCGAAACACCCGAACGTTGAG -900-
GAAGCGATCATCAAAGAAATCCAGACTGTTATTGGTGAACGTGACATCAA -950-
AATTGACGACATCCAGAAACTGAAAGTTATGGAAAACTTCATCTACGAGT -1000-
CTATGCGTTACCAGCCGGTTGTTGACCTGGTCATGCGTAAGGCGCTGGAG -1050-
GACGACGTTATTGACGGTTACCCGGTCAAAAAAGGTACCAATATCATCCT -1100-
GAACATCGGTCGTATGCACCGTCTCGAATTCTTCCCGAAACCGAACGAAT -1150-
TCACCCTCGAGAATTTTGCGAAGAATGTTCCGTACCGTTACTTCCAGCCG -1200-
TTCGGCTTCGGTCCGCGTGGTTGCGCGGGTAAATACATCGCAATGGTTAT -1250-
GATGAAGGCCATCCTGGTTACTCTGCTGCGTCGTTTCCACGTTAAAACTC -1300-
TGCAGGGTCAGTGCGTTGAATCTATTCAGAAAATCCACGACCTCTCTCTG -1350-
CACCCGGACGAAACCAAGAATATGCTGGAGATGATCTTCACCCCGCGTAA -1400-
TTCTGACCGTTGTCTGGAACACCATCATCACCACCACTAACGAAGCTTAT -1450-
```

Figure 38. cDNA optimization for P450 19A1 expression in *E. coli.* *A,* cDNA sequence after optimization (note: a stop codon was inserted during the sequence corrections, *vide infra*). *B*, Oligonucleotides used for synthons generation in polymerase cycling assembly.

B

Primer	PCA primer sequence
1	GGTGGTCATATGGCCAAAAAAACCTCTTCTAAAGGTCGTAACTAC
2	ACCAGGACCCGGGATAGAGGAAGTACCTTCGTAGTTACGACCTTTAGAAGAGGT
3	TCTATCCCGGGTCCTGGTTACTGCATGGGCATCGGTCCGCTGATCTCTCACGGT
4	GTTGCACGCAGAACCAATACCCATCCACAGGAAACGACCGTGAGAGATCAGCGG
5	GTATTGGTTCTGCGTGCAACTACTACAACCGTGTTTACGGCGAATTCATGCGTG
6	TAGAGATAATCAGGGTTTCTTCGCCAGAGATCCAAACACGCATGAATTCGCCGT
7	GCGAAGAAACCCTGATTATCTCTAAGTCCAGCTCTATGTTCCACATCATGAAGC
8	TTAGAGCCGAAACGAGAGGAGTAATGGTTGTGCTTCATGATGTGGAACATAGAG
9	TCCTCTCGTTTCGGCTCTAAACTGGGTCTGCAGTGCATTGGTATGCACGAAAAA
10	CCACAGCTCCGGGTTGTTATTGAAGATGATACCTTTTTCGTGCATACCAATGCA
11	ACAACCCGGAGCTGTGGAAAACCACCCGTCCGTTCTTTATGAAAGCGCTGTCTG
12	GCAAACGGTAACCATACGAACCAGACCCGGACCAGACAGCGCTTTCATAAAGAA
13	GTTCGTATGGTTACCGTTTGCGCTGAATCTCTGAAAACCCACCTGGACCGTCTG
14	GAACGTCAACATAACCGGACTCATTGGTGACTTCTTCCAGACGGTCCAGGTGGG
15	AGTCCGGTTATGTTGACGTTCTGACCCTGCTGCGTCGTGTTATGCTGGACACCT
16	TTCGTCCAGCGGGATACGCAGGAACAGGGTGTTGGAGGTGTCCAGCATAACACG
17	CGTATCCCGCTGGACGAATCTGCTATCGTTGTTAAAATCCAGGGTTATTTCGAC
18	GTCCGGCTTGATCAGCAGCGCCTGCCACGCGTCGAAATAACCCTGGATTTTAAC
19	CTGCTGATCAAGCCGGACATTTTCTTCAAAATTTCCTGGCTGTACAAGAAGTAT
20	CTTCTCATACTTCTTGTACAGCCAGGAAA
21	TCTTGGCTGTACAAAAAGTACGAAAAGTCTGTTAAAGACCTGAAGGACGCGATTG
22	GGTGCTGATACGACGACGCTTCTCCGCAATCAGAACTTCAATCGCGTCCTTCAGGTC
23	CGTCGTCGTATCAGCACCGAAGAAAAACTCGAAGAGTGCATGGACTTTGCGACCGAG
24	TCACGGGTCAGGTCACCACGTTTTTCCGCCAGGATCAGCTCGGTCGCAAAGTCCATG
25	GGTGACCTGACCCGTGAAAACGTTAACCAGCGTATCCTCGAAATGCTGATCGCGGCA
26	GGAACAGCATGAAGAACAGAGAAACGCTCATGGTGTCCGGTGCCGCGATCAGCATTT
27	CTCTGTTCTTCATGCTGTTCCTCATCGCGAAACACCCGAACGTTGAGGAAGCGATCA
28	ATGTCACGTTCACCAATAACAGTCTGGATTTCTTTGATGATCGCTTCCTCAACGTTC
29	CTGTTATTGGTGAACGTGACATCAAAATTGACGACATCCAGAAACTGAAAGTTATGG
30	GCTGGTAACGCATAGACTCGTAGATGAAGTTTTCCATAACTTTCAGTTTCTGGATGT
31	CGAGTCTATGCGTTACCAGCCGGTTGTTGACCTGGTCATGCGTAAGGCGCTGGAGGA
32	ATTGGTACCTTTTTTGACCGGGTAACCGTCAATAACGTCGTCCTCCAGCGCCTTACG
33	CCGGTCAAAAAAGGTACCAATATCATCCTGAACATCGGTCGTATGCACCGTCTCGAA
34	AAATTCTCGAGGGTGAATTCGTTCGGTTTCGGGAAGAATTCGAGACGGTGCATACGA
35	ACGAATTCACCCTCGAGAATTTTGCGAAGAATGTTCCGTACCGTTACTTCCAGCCGT
36	CGATGTATTTACCCGCGCAACCACGCGGACCGAAGCCGAACGGCTGGAAGTAACGGT
37	TGCGCGGGTAAATACATCGCAATGGTTATGATGAAGGCCATCCTGGTTACTCTGCTG
38	CGCACTGACCCTGCAGAGTTTTAACGTGGAAACGACGCAGCAGAGTAACCAGGATGG
39	TCTGCAGGGTCAGTGCGTTGAATCTATTCAGAAAATCCACGACCTCTCTCTGCACCC
40	GGGGTGAAGATCATCTCCAGCATATTCTTGGTTTCGTCCGGGTGCAGAGAGAGGTCG
41	CTGGAGATGATCTTCACCCCGCGTTCTTCTGACCGTTGTCTGGAACACCATCATCAC
42	TTTGTCATCAATAAGCTTGTGGTGGTGATGATGGTGTTCCAGACA

A

```
MVLEMLNPIHYNITSIVPEAMPAATMPVLLLTGLFLLVWN

MAKKTSSKGR----------------------------N
```

B

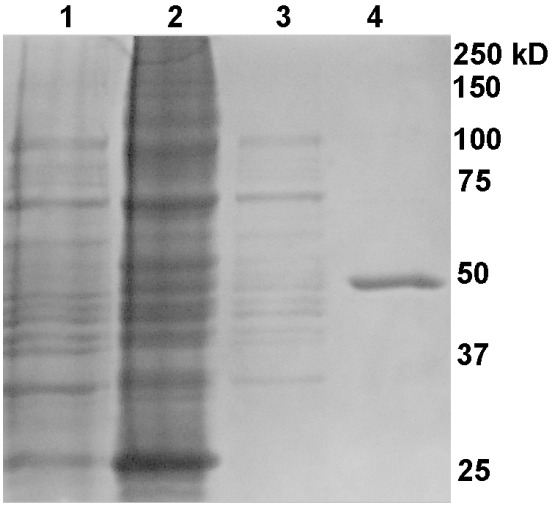

Figure 39. *N*-Terminal sequence and purification of P450 19A1 protein. *A, N*-terminal sequence of native mammalian P450 19A1 (top) and the modification used for heterologous expression (bottom). *B*, SDS-PAGE (10% gel, stained with Coomassie Brilliant Blue G250). Lane 1, whole cells; lane 2, membrane-bound fraction; lane 3, solubilized membrane fraction; lane 4, purified P450 19A1. Nominal protein concentrations loaded in lanes 1-4 were 70, 55, 7, and 1.7 μg, respectively.

for 30 min. After separation by centrifugation at 5000 × *g* (20 min), the resulting spheroplast pellet was resuspended in Buffer B (100 mM potassium phosphate buffer (pH 7.4), containing 20% glycerol (v/v), 6 mM magnesium acetate, and 0.1 mM DTT). To this were added the protease inhibitors leupeptin (2 μM), aprotinin (0.04 U/ml), bestatin (1 μM), and phenylmethylsulfonyl fluoride (1 mM final, from a 100 mM stock solution in 1-propanol). The spheroplasts were sonicated and separated by centrifugation at 12,000 × *g* (20 min). The supernatant was harvested and separated by ultracentrifugation at 142,000 × *g* (60 min), and the pellet was resuspended in minimal Buffer B. The membranes were diluted with Buffer C (100 mM potassium phosphate buffer (pH 7.4) containing 20% glycerol (v/v), 1% CHAPS detergent (w/v), and 0.1 mM DTT) to a concentration of ~ 2.5 mg/ml total protein (as determined by a bicinchoninic acid assay) and were solubilized overnight with gentle stirring. The solubilized membrane-bound proteins were separated from the membranes by ultracentrifugation at 142,000 × *g* (60 min).

Two 8-ml nickel-NTA resin (Qiagen, Valencia, CA) columns were poured and equilibrated with Buffer D (100 mM potassium phosphate buffer (pH 7.4) containing 20% glycerol (v/v), 1% CHAPS detergent (w/v), 0.1 mM DTT, and 0.5 M NaCl). The solubilized protein supernatant (~ 1.2 l) was fortified with 0.5 M NaCl and loaded onto the two nickel-NTA columns (operated in parallel) using a pump (flow rate ~ 1.8 ml/min). The columns were then washed with 200 ml of Buffer E (Buffer D containing 30 mM imidazole). P450 19A1 was eluted with a linear gradient of 30 to 300 mM imidazole in Buffer D (140 ml total, elution began ~ 100 mM imidazole). The most concentrated fractions (A_{417}) were combined and dialyzed in Buffer F (100 mM potassium

phosphate buffer (pH 7.4) containing 1 mM EDTA and 20% glycerol (v/v)). The purified P450 19A1 was stored at -70 ° C. Purity and concentration of P450 19A1 was assessed by a variety of methods (see Figures 39 and 40, Table 2)

Other Enzyme Preparations—The same protocols were used as described in Chapter II (*vide supra*).

Spectroscopy—UV-visible spectra were recorded with either an Aminco DW2/OLIS or a Cary14/OLIS spectrophotometer as in previous chapters. In steady-state titrations, P450 19A1 (1 μM) was titrated with increasing amounts of ligand dissolved in CH_3OH, with a reference cuvette containing only P450 19A1 (final organic solvent concentration ≤ 2%, v/v). Scans were made from 350-500 nm, in duplicate, and averaged. The inherent absorbance of estrone required the use of a tandem (Yankeelov) cuvette in these titrations, as described in Chapter II (32).

Stopped-flow absorbance and fluorescence experiments were performed on an OLIS RSM-1000 instrument as described (*vide supra*). In this case, fluorescence measurements were made using excitation at 325 nm and a > 385 nm long pass filter, with 3.16 nm slits. Stopped-flow experiments shorter than 15 s were reported as averages of four individual experiments and longer time point studies were an average of two.

Anaerobic experiments were performed as described in Chapter II, although in this case a protocatechuate/protocatechuate dioxygenase oxygen scrubbing system was used (162). P450 19A1 (1 μM) preincubated with andro, 19-OH andro, 19=O andro, or estrone (all with CO) was reduced upon the addition of NADPH (150 μM), and

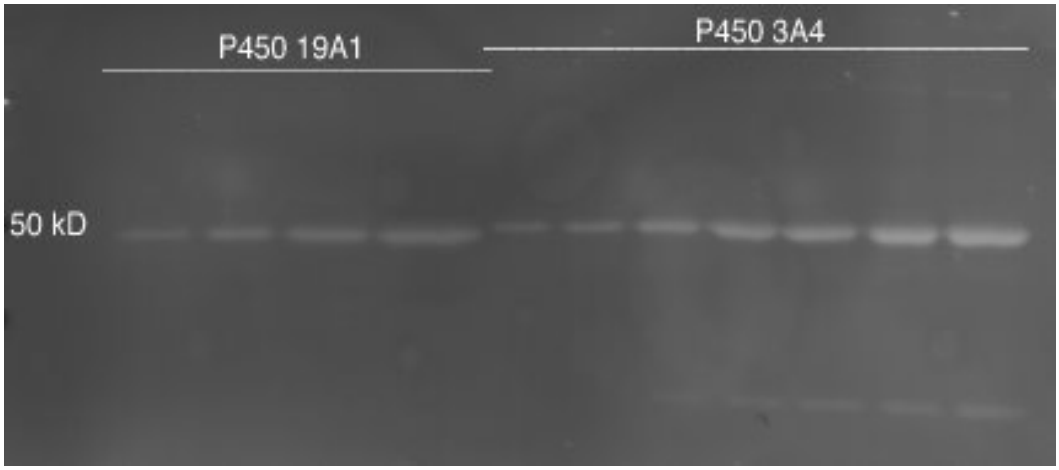

Figure 40. Immunoblot of P450 19A1. Four dilutions of purified P450 19A1 were loaded for SDS-PAGE (10%, w/v), along with seven dilutions of a P450 3A4 standard that also contained a hexa-histidine tag. The proteins were transferred to a polyvinylidene fluoride membrane (BioRad, Hercules, CA). A primary mouse anti-his_6-peroxidase antibody was used (Roche, San Francisco, CA) to detect the presence of protein containing a hexa-histidine tag. The secondary antibody was goat anti-mouse IRD800CW, which emits infrared light at 800 nm, and was detected using an Odyssey Li-Cor instrument (Li-Cor, Lincoln, NE). Shown in the first four lanes are various dilutions of purified P450 19A1. The final seven lanes contain P450 3A4 with a hexa-histidine tag as a standard for quantitation (shown are 1, 2, 4, 8, 10, 12, and 16 pmol P450 3A4). The output from the channel detecting the infrared signal at 800 nm is shown.

Table 2. Quantitation of P450 19A1 expression and purification.

Purification stage	P450, nmol[a]	P450 plus cytochrome P420, nmol[b]	Heme, nmol[c]	P450 protein, nmol[d]	Total protein, mg[e]	Specific content, nmol P450/mg protein
Whole cells	2700[f]	--	--	2500	84,000	0.032
Membranes	370[f]	--	--	260	2,200	0.17
Solubilized protein	370[f]	1700[f]	--	950	1,700	0.22
Purified P450 19A1	120[f]	170[f]	180	420	19	6.3

[a]Fe^{2+}•CO *vs*. Fe^{2+} difference spectrum.
[b]Fe^{2+}•CO *vs*. Fe^{2+} difference spectrum in which the absorbance change at 420 nm is added to the absorbance change at 450 nm to calculate total P450.
[c]Pyridine hemochrome assay.
[d]Immunoblot analysis, quantified based on the Fe^{2+}•CO *vs*. Fe^{2+} difference spectrum of P450 3A4.
[e]Bicinchoninic acid (BCA) analysis.
[f]Safranin dye included (2 μM).

measurements were made by averaging results from four shots.

Measurement of Enzyme Activity—In steady-state studies, the reconstituted enzyme system contained 0.10 μM P450 19A1, 0.20 μM NADPH-P450 reductase, and 9 μM L-α-1,2-dilauroyl-*sn*-glycero-3-phosphocholine (*vide supra*), followed by the addition of substrate dissolved in CH_3OH (final organic solvent content $\leq$ 1% v/v). Volumes of incubations were 1.0 ml and contained 100 mM potassium phosphate buffer because the P450 19A1 was unstable in buffers of lower ionic strength.

In addition to Fe^{2+}•CO *vs*. Fe^{2+} difference spectral analysis, P450 19A1 activity was measured using slight modifications of a tritiated water release assay (163). Briefly, a reconstituted enzyme system containing 20 nM P450 19A1, 600 nM NADPH-P450 reductase, and 28 μM L-α-1,2-dilauroyl-*sn*-glycero-3-phosphocholine (*vide supra*) was incubated with 4.9 μM [1β-^{3}H]-andro (2 μCi) for 5 min (1.0 ml volume). Following quenching with 3 ml of $CHCl_3$, 0.75 ml of the (upper) aqueous layer was removed and mixed with a vortex device after adding charcoal-dextran (5% (w/v) charcoal, 0.5% (w/v) dextran). This mixture was added to a centrifugal filter device (Fisher, Fair Lawn, NJ) filled with Celite® and the charcoal-dextran was separated by centrifugation (2,000 × *g*, 5 min). The radioactivity in an aliquot of H_2O was then quantified using a scintillation counter (Beckman LS6500, Beckman, Brea, CA).

For steady-state kinetic analyses, reactions were run in duplicate for 5 min, quenched with 1.0 ml of CH_2Cl_2, and mixed with a vortex device. Following centrifugation, 0.75 ml of the organic layer was transferred, dried under a N_2 stream, and then dissolved in 30 μl of CH_3OH prior to HPLC analysis. Due to the very low K_m for

conversion of andro to estrone, radiolabeled starting material ([1,2,6,7-^{3}H]-andro) was required (a range of 0.02-1.2 μCi/incubation was used) and the reconstituted enzyme system contained 2.0 nM P450 19A1, 60 nM NADPH-P450 reductase, and 1.8 μM L-α-1,2-dilauroyl-*sn*-glycero-3-phosphocholine. For all reactions, HPLC (20 μl injections) was used to separate the compounds using the C_{18} column described in Chapter II.

HPLC separation strategies were modified based on work by Zhou et al. (164). Separations were achieved (flow rate of 1.0 ml/min) with solvent A (83% H_2O, 17% tetrahydrofuran, v/v) and solvent B (83% CH_3OH, 17% tetrahydrofuran, v/v), using a linear gradient from 40% to 100% B from 0 to 6 min (v/v), held isocratic from 6-8 min at 100% B. For the studies with radiolabeled andro, HPLC was used with a liquid scintillation flow counter (In/Us β-Ram, Brandon, FL). A second, larger-scale incubation was performed in order to relate peak area in the radiochromatograms to A_{280}, using a Spectra Series UV100 spectrophotometer for the quantitation of estrone. In the cases of the incubations with 19-OH andro and 19=O andro, separations were monitored at 240 and 285 nm (the 285 nm trace and external standards were used for quantitation) using a ThermoFinnigan UV3000 rapid-scanning UV detector. A sample chromatogram is shown in Figure 41.

The same conditions for incubations and HPLC analysis described for the andro activity assay (*vide supra*) were used for pulse-chase experiments (with 400 nM [1,2,6,7-^{3}H]-andro), except that either 210 μM 19-OH andro or 180 μM 19=O andro was added at time points of 30 or 60 s (the total incubation time was 5 min).

Pre-steady-state kinetics were performed under single turnover conditions in a quench flow apparatus (model RFQ-3, Kintek Corp, Austin, TX). Specifically, 2.0 μM

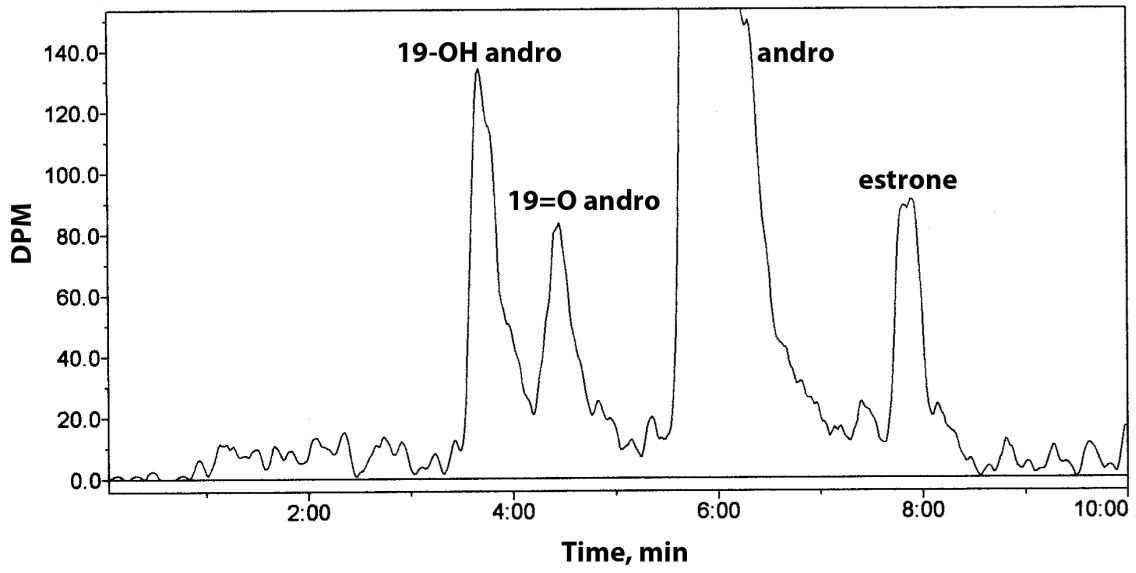

Figure 41. Sample HPLC radiochromatogram following incubation of P450 19A1 with radiolabeled andro. Shown are 19-OH andro at t_R = 3.6 min, 19=O andro at t_R = 4.5 min, andro at t_R = 5.8 min, and estrone at t_R = 7.8 min.

[4-^{14}C]-androstenedione was added to a reconstituted enzyme system containing 2.0 μM P450 19A1, 4.0 μM NADPH-P450 reductase, and 250 μM L-α-1,2-dilauroyl-*sn*-glycero-3-phosphocholine. Reactions (in duplicate) were initiated by the addition of 500 μM NADPH and were quenched by the addition of 2% $ZnSO_4$ (w/v) after a time period of 100 ms to 28 s. Sample workup and HPLC analysis were performed as described (*vide supra*), although the dried samples were dissolved in 25 μl of CH_3OH for injection. As the specific activity of the radiolabeled substrate was low (4.8 nCi present at each time point), five individual reactions (at each time point) were combined for HPLC analysis.

Rates of NADPH oxidation were measured as described previously (165). Briefly, reconstituted enzyme systems were prepared (*vide supra*) with 0.40 μM P450 19A1 and 125 μM substrate except in the case of estrone, where 20 μM substrate was used. The sample was preincubated at 37 °C using a water bath attached to the Aminco DW2/OLIS spectrophotometer, and the reaction was initiated by adding 180 μM of NADPH and monitored at 340 nm. OLIS software was used to calculate the linear rates of NADPH oxidation, using $\varepsilon_{340} = 6.22\ mM^{-1}\ cm^{-1}$ for NADPH oxidation.

Analysis of Kinetic and Binding Data—In the anaerobic studies, the OLIS fitting software was used to fit the traces to single- or double-exponential equations. In the cases of the pre-steady-state binding experiments, DynaFit software (44) was used for double-exponential fits. Kintek Explorer® software (45) was employed for fitting the single turnover experimental data, and this fit was constrained in part by fitting *v vs*. substrate concentration plots using DynaFit software.

Results

P450 19A1 Expression and Purification—A method was developed that routinely achieved ~ 400-500 nmol/l expression of P450 19A1 and involved the use of a single column for purification, without the need for non-ionic detergents. In order to enhance expression in *E. coli*, the native mammalian P450 19A1 cDNA sequence was modified. Polymerase cycling assembly was used to optimize the cDNA codons for *E. coli* (Figure 38). The *N*-terminus was replaced with a sequence developed for improving heterologous expression of rabbit P450s (166) (Figure 39*A*) and a hexa-histidine tag was added to the *C*-terminus. Finally, optimization of the strain of *E. coli* used (TOP 10) yielded some of the greatest improvement in expression levels.

Many difficulties in purification of P450 19A1 have been cited in the literature, typically related to loss of Fe^{2+}•CO *vs*. Fe^{2+} difference spectra due either to protein instability or suspected masking of signal by detergents or ligands used in purification (50, 51). I found that one successful method of stabilizing P450 19A1 during purification was the addition of the 19A1 inhibitor αNF (167) during the solubilization and chromatography steps (51), an approach used previously with P450s 1A1 and 1A2 (96). However, I subsequently found that removal of this ligand was virtually impossible despite extensive column washing steps and dialysis (with αNF quantified by fluorescence spectroscopy after extraction from P450 19A1 with organic solvent). Unsurprisingly, the measured K_d for αNF was very low (0.09 ± 0.02 μM, estimated by monitoring the fluorescence quenching of αNF upon titration with P450 19A1). Alternatively, stability could be improved by limiting the exposure time of the P450 19A1 to the nickel-NTA resin during the chromatography step and using high ionic

strength (100 mM potassium phosphate buffer) throughout. Nickel-NTA nickel chromatography was sufficient to achieve > 95% electrophoretic purity (Figure 39*B*). Overall yields of P450 19A1 were not particularly high (Table 2 and Figure 40) but sufficient for kinetic analysis.

Spectral analysis of purified P450 19A1 yielded rather typical Fe^{2+}•CO *vs*. Fe^{2+} reduced difference (Figure 42*A*) and absolute (Figure 42*B*) spectra. Fe^{2+}•CO *vs*. Fe^{2+} reduced difference spectra were improved by the addition of safranin T (2 μM) as an electron mediator in the assays (96). P450 19A1 displayed "Type I" changes (increase at 390 nm and decrease at 420 nm as binding of the ligand caused displacement of H_2O as the sixth axial ligand) (43) upon binding andro (Figure 42*C*), although only about 18% maximal conversion to the high-spin iron state was observed (Figure 42*C* inset). The heme content, measured by the pyridine hemochrome assay (168), was similar to the sum of P450 plus cytochrome P420 (Table 2).

Steady-State Kinetics of Ligand Binding to P450 19A1—Andro, 19-OH andro, 19=O andro, and estrone all behaved as Type I ligands (Figure 43). These titrations displayed tight ligand binding with dissociation constants in the low μM range (Table 3), and fitting such plots (Figure 43) required quadratic equations. Andro showed the strongest affinity for P450 19A1 with a K_d value of 0.13 μM, while 19-OH andro, 19=O andro, and estrone yielded K_d values of 1.5, 3.6, and 4.0 μM, respectively.

Pre-Steady-State Kinetics of Ligand Binding to P450 19A1—Stopped-flow absorbance or fluorescence spectroscopy was used to measure pre-steady-state rates of

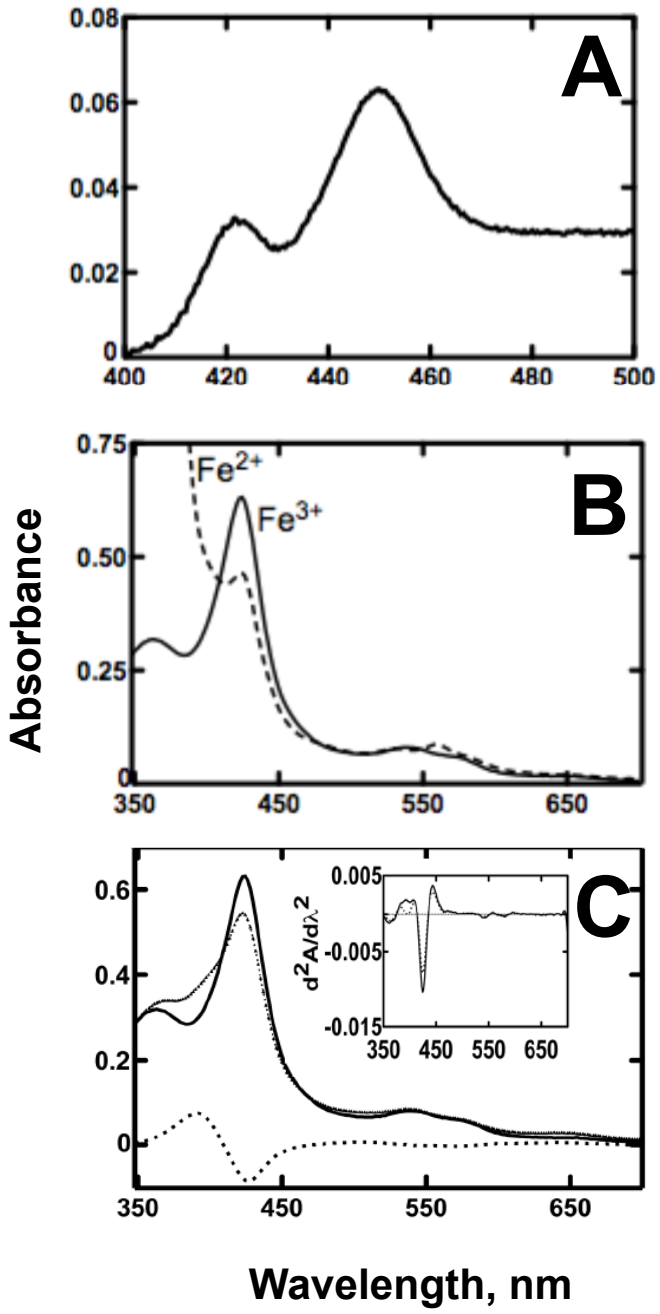

Figure 42. Spectra of purified P450 19A1. *A*, Fe^{2+}•CO *vs*. Fe^{2+} difference spectrum (using 2 μM safranin T dye as an electron mediator). *B*, Absolute spectrum showing ferric and ferrous forms. *C*, Absolute spectrum of 2 μM P450 19A1 in the absence (—) or presence (·····) of 10 μM andro and the difference between the two spectra (■ ■ ■). Also shown (inset) are the second derivative of the spectra recorded in the absence (—) or presence (■ ■ ■) of 10 μM andro, showing about 18% conversion from low- to high-spin iron upon ligand binding.

Table 3. Steady-state parameters of P450 19A1 turnover and dissociation constants.

Substrate	k_{cat}, s^{-1}	K_m, μM	k_{cat}/K_m, $M^{-1} s^{-1}$	K_d, μM
andro	0.060 ± 0.003	0.044 ± 0.006	1.4×10^6	0.13 ± 0.07
19-OH andro	0.13 ± 0.01	21 ± 6	6.2×10^3	1.5 ± 0.4
19=O andro	0.42 ± 0.03	18 ± 5	2.3×10^4	3.6 ± 0.6
estrone	--	--	--	4.0 ± 1.0

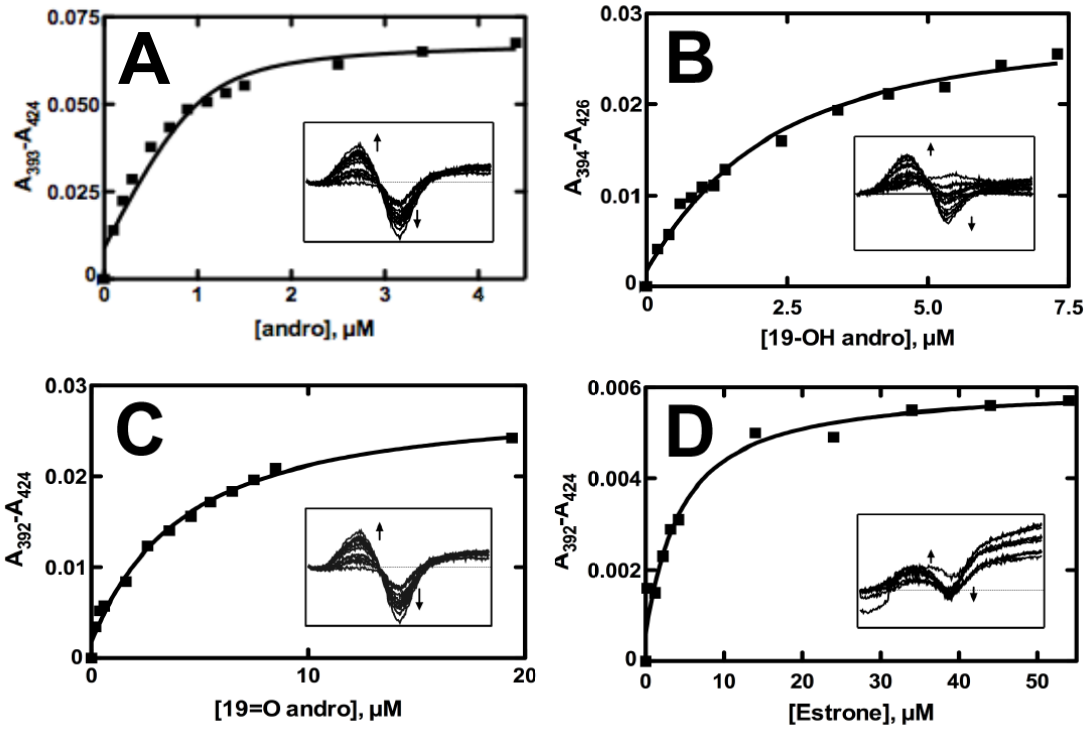

Figure 43. Steady-state binding of ligands to P450 19A1. Titration of P450 19A1 (1 μM) with varying concentrations of ligand. Insets show the spectral changes, and the plots are quadratic fits of the changes in absorbance. *A,* Andro, K_d = 0.13 ± 0.07 μM; *B,* 19-OH andro, K_d = 1.5 ± 0.4 μM; *C,* 19=O andro, K_d = 3.6 ± 0.6 μM; *D,* Estrone, K_d = 4.0 ± 1.0 μM.

binding of andro, 19-OH andro, 19=O andro, and αNF to P450 19A1 (Figure 44). When the changes in absorbance upon ligand binding were fit to a single-exponential equation (i.e. a simple one-step binding mechanism, E + L ⇆ EL), a second-order rate constant (k_{on}) of ~ 5.6 × 10^4 M^{-1} s^{-1} resulted, which is probably 100-1000 times too slow for a diffusion-limited interaction (46). Instead a two-step binding mechanism was used: E + L ⇆ EL ⇆ LE, with a fast, spectroscopically-silent initial step followed by a slower change that affected the heme Soret region. This initial fast, absorbance-silent step theoretically could be captured if a fluorescent ligand was used, as previously shown in studies with P450s 3A4 (92) and 1A2 (Chapter II and (32)). In this case, quenching of the native fluorescence of the ligand occurs upon the first interaction with the enzyme and does not depend on heme Soret region changes proposed to occur following an initial binding step. By using the fluorescent P450 19A1 inhibitor αNF (*vide supra*), a very fast initial interaction with the protein was observed (~ 10^3 × faster than changes seen in absorbance) (Figure 44*D*).

Double-exponential equations provided good fits to the biphasic curves observed for andro, 19-OH andro, and 19=O andro binding, with initial binding rates that ranged from 2.5 × 10^6 to 2.0 × 10^7 M^{-1} s^{-1} (Figure 44, using DynaFit software). The andro, 19-OH andro, and 19=O andro fits were constrained using both the raw data and the K_d values (from the steady-state titration data) (Figure 45). In support of this two-step binding mechanism, the fluorescence quenching of αNF upon binding P450 19A1 was significantly faster than the observed absorbance changes, and the data were fit to a double-exponential equation with an initial rate (k_1) of 1.0 × 10^7 M^{-1} s^{-1}, which is realistic

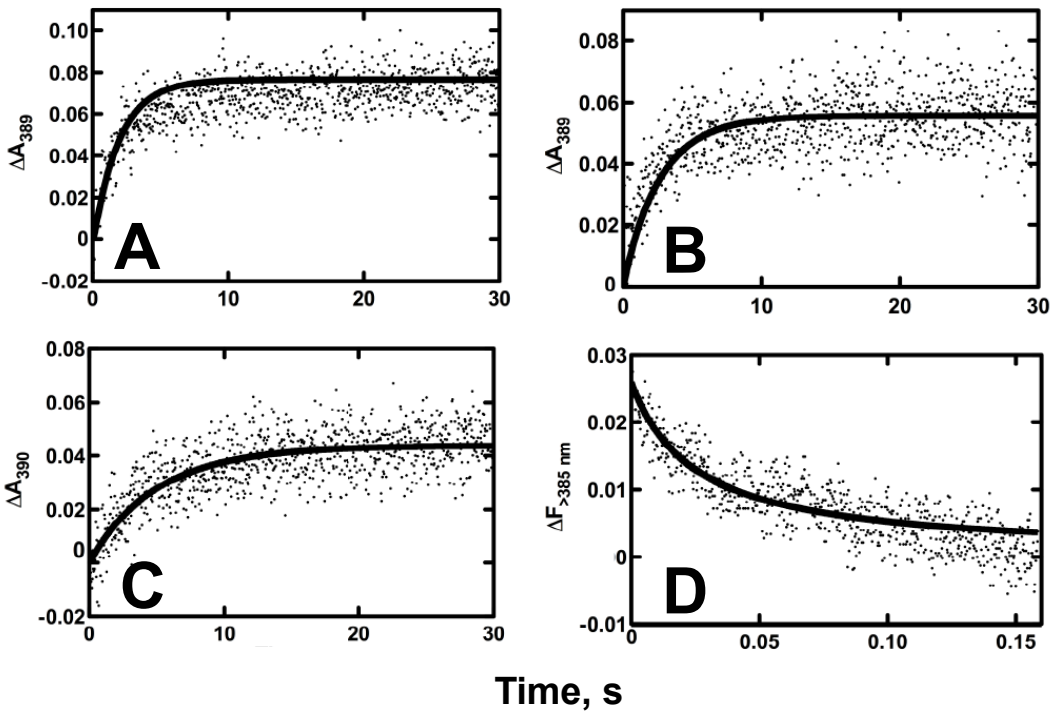

Figure 44. Pre-steady-state binding kinetics of ligands to P450 19A1. Stopped-flow absorbance (*A-C*) and fluorescence (*D*) changes for binding of various ligands (2 μM) to P450 19A1 (2 μM). Raw data are presented as scatter plots and the overlaid lines are fits using DynaFit software. *A*, Andro (ΔA_{390}), $k_1 = 2.5 \times 10^6$ M^{-1} s^{-1}, $k_{-1} = 1.4$ s^{-1}, $k_2 = 0.42$ s^{-1}, $k_{-2} = 0.20$ s^{-1}; *B*, 19-OH andro (ΔA_{390}), $k_1 = 2.0 \times 10^7$ M^{-1} s^{-1}, $k_{-1} = 240$ s^{-1}, $k_2 = 0.80$ s^{-1}, $k_{-2} = 0.15$ s^{-1}; *C*, 19=O andro (ΔA_{390}), $k_1 = 2.5 \times 10^6$ M^{-1} s^{-1}, $k_{-1} = 300$ s^{-1}, $k_2 = 2.4$ s^{-1}, $k_{-2} = 0.13$ s^{-1}; *D*, αNF ($\Delta F_{>385}$), $k_1 = 1.0 \times 10^7$ M^{-1} s^{-1}, $k_{-1} = 0.1$ s^{-1}, $k_2 = 0.01$ s^{-1}, $k_{-2} = 0.18$ s^{-1}.

A

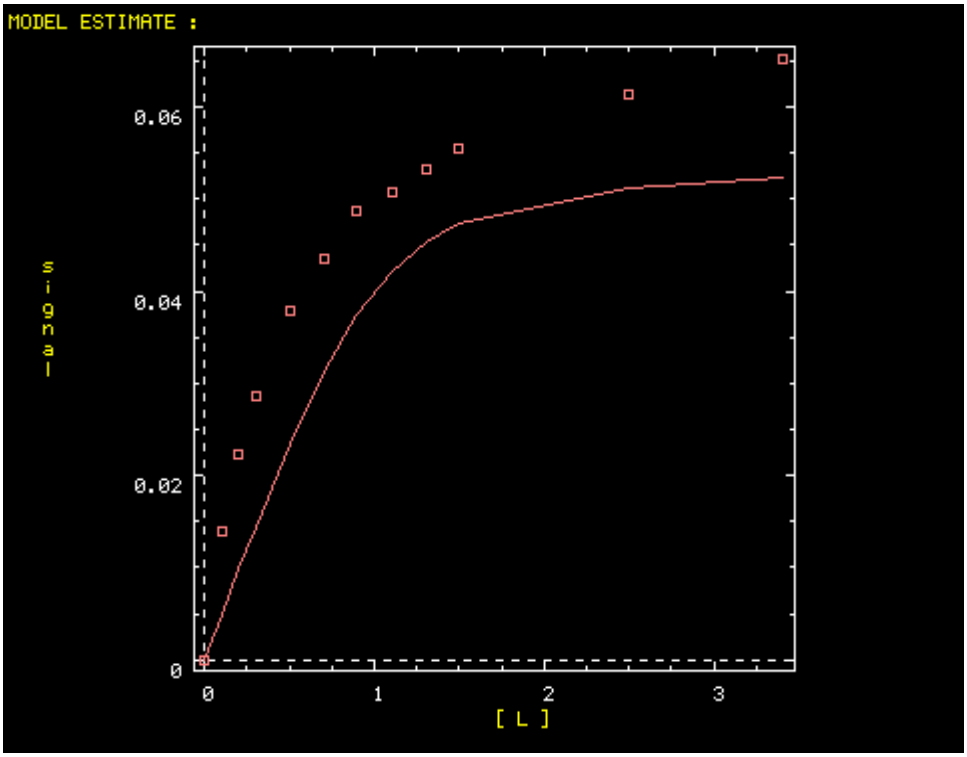

Figure 45. DynaFit iterations for fitting stopped-flow spectroscopy binding data and steady-state titration data. See Appendix for corresponding scripts. For all plots, the y axis is ΔA_{390} and the x axis is the ligand concentration in μM. *A*, DynaFit results from fitting the steady-state titration data of andro binding to P450 19A1 (Figure 43) *B*, DynaFit results from fitting the steady-state titration data of 19-OH andro binding to P450 19A1 (Figure 43). *C*, DynaFit results from fitting the steady-state titration data of 19=O andro binding to P450 19A1 (Figure 43).

B

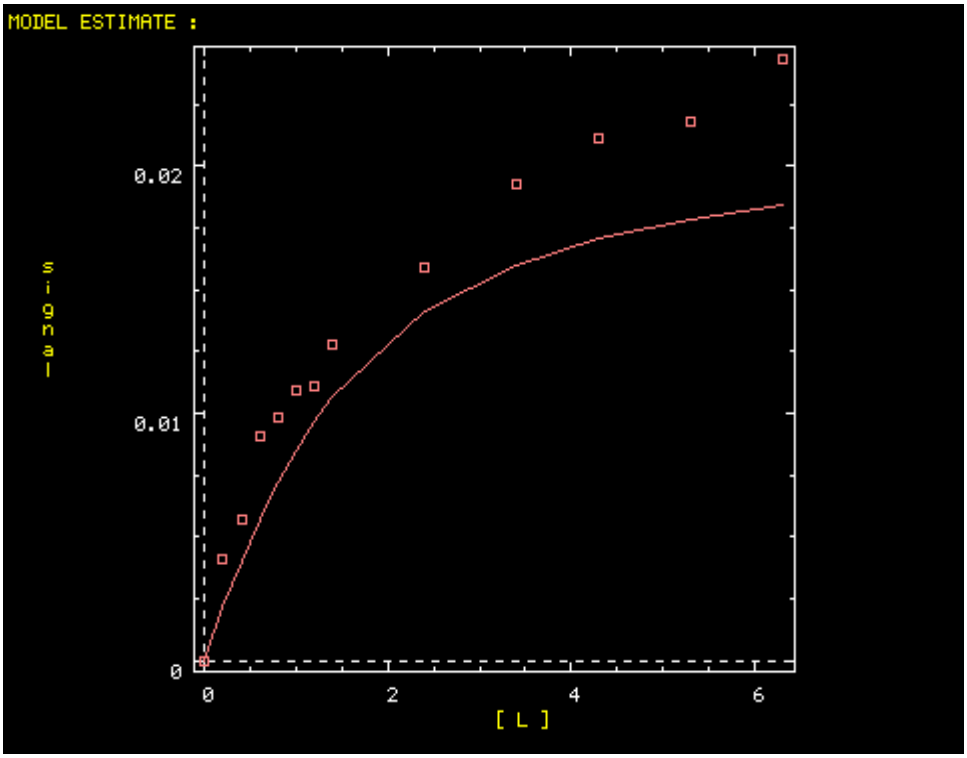
MODEL ESTIMATE :
0.02
0.01
0
signal
0
2
4
6
[L]

C

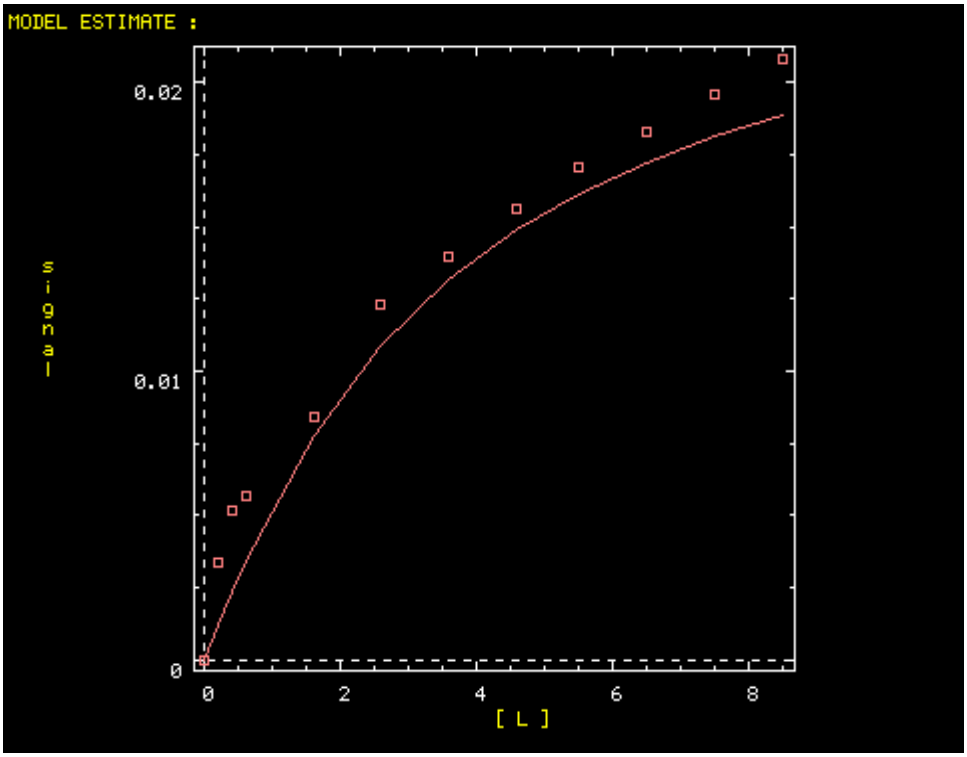
MODEL ESTIMATE :
0.02
0.01
0
signal
0
2
4
6
8
[L]

for a second-order encounter phenomenon (46) (Figure 44*D*). The faster rate seen for fluorescence compared to absorbance strongly supports the E + L ⇆ EL ⇆ LE mechanism, where E + L ⇆ EL is the initial fast binding step that can be captured for observation by fluorescence quenching of the ligand, and EL ⇆ LE is a slower binding step related to interaction with the heme.

Rates of Reduction of P450 19A1—The rates of reduction of ferric P450 19A1 in the absence of any ligand were extremely slow (~ 0.03 s^{-1}, data not shown). However, much higher rates were observed in the presence of ligands, particularly in the case of 19-OH andro and 19=O andro (Figure 46). It is typically assumed in such reduction studies that CO interacts rapidly with P450s with high affinity, regardless of other ligands present, and thus absorbance changes at 450 nm indicate rates of reduction and are not complicated by the kinetics of CO binding. However, this was not the case in measuring rates of reduction of P450 19A1 in the presence of 19-OH andro and estrone. A Fe^{2+}•CO *vs*. Fe^{2+} difference spectrum (Figure 47) indicated that iron reduction occurred but the addition of 19-OH andro precluded CO from binding, preventing the Soret absorbance increase at 450 nm. A similar phenomenon was observed for estrone binding, although the signal at 450 nm was high, but the apparent rate of reduction (0.098 ± 0.002 s^{-1}) was slower than the k_{cat} (data not shown). In both cases, the change in absorbance at 390 nm (rather than 450 nm) was extracted and used to determine rates of reduction. While the reduction of P450 19A1 in the presence of andro could be fit to a single-exponential equation (k = 1.7 ± 0.1 s^{-1}), the reduction data for P450 19A1 in the presence of 19-OH andro, 19=O andro, and estrone were better fit to double-exponential equations with fast

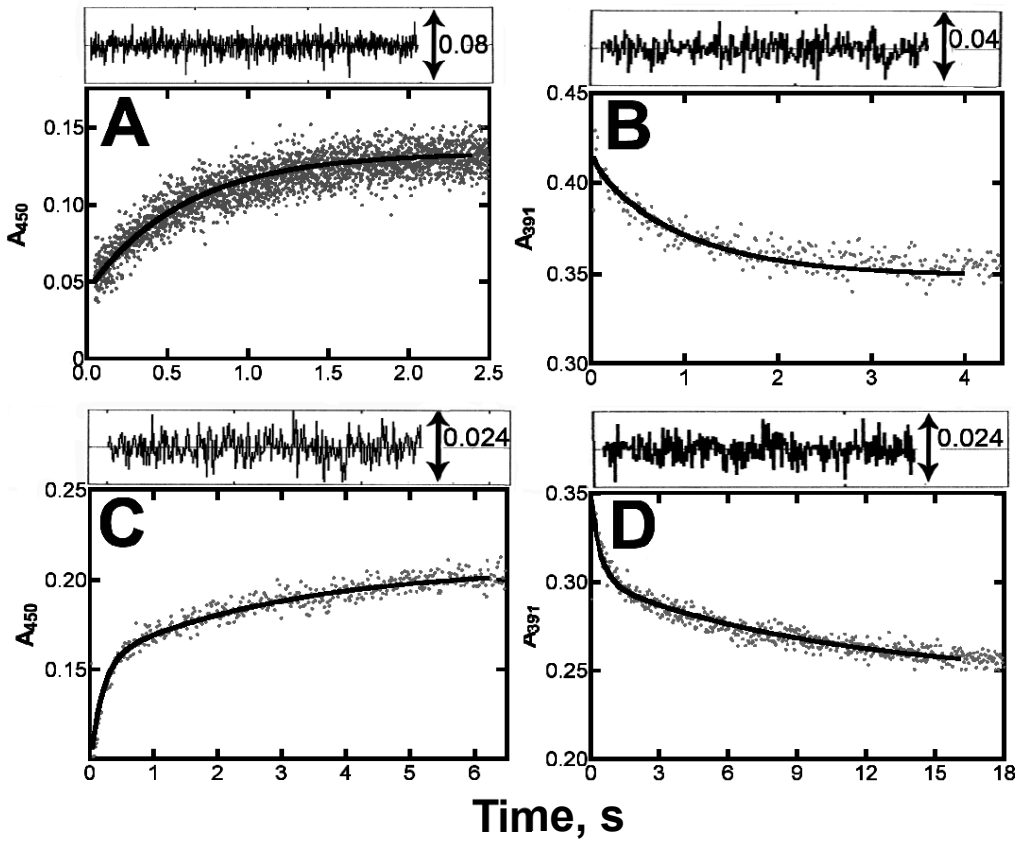

Figure 46. Reduction kinetics of P450 19A1. Stopped-flow absorbance traces of the reduction of P450 19A1 (1 μM) by NADPH-P450 reductase (2 μM) in the presence of L-α-1,2-dilauroyl-*sn*-glycero-3-phosphocholine (95 μM) and various ligands (5 μM) upon the addition of NADPH (150 μM). *A,* Andro (ΔA_{450}), k = 1.7 ± 0.1 s^{-1}; *B,* 19-OH andro (ΔA_{391}), k_{fast} = 10 ± 4 s^{-1}, k_{slow} = 0.97 ± 0.12 s^{-1}; *C,* 19=O andro (ΔA_{450}), k_{fast} = 5.4 ± 0.5 s^{-1}, k_{slow} = 0.34 ± 0.06 s^{-1}; *D,* Estrone (ΔA_{391}), k_{fast} = 2.2 ± 0.4 s^{-1}, k_{slow} = 0.098 ± 0.02 s^{-1}. The analysis of residuals is shown at the top of each plot.

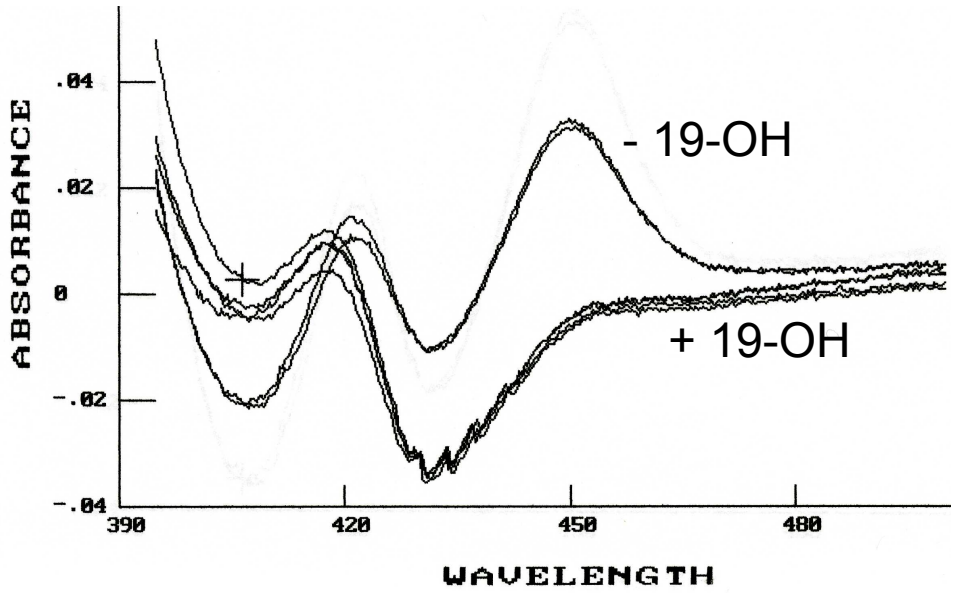

Figure 47. Fe^{2+}•CO *vs.* Fe^{2+} difference spectra in the absence and presence of 19-OH andro. P450 19A1 (1 μM) in the absence and presence of 19-OH andro (20 μM).

initial rate constants (k_{fast}) of 10, 5.4, and 2.2 s^{-1}, respectively. In all cases, the rates of iron reduction were much faster than the measured rates of substrate oxidation (*vide infra*).

The steady-state rates of oxidation of NADPH by P450 19A1 in the presence of NADPH-P450 reductase were also measured. In the absence of ligands, rates of 0.40 ± 0.02 nmol NADPH oxidized (nmol P450)$^{-1}$ s^{-1} were measured, while faster rates of 1.23 (± 0.07), 1.03 (± 0.08), 0.90 (± 0.02), and 0.45 (± 0.03) nmol NADPH oxidized (nmol P450)$^{-1}$ s^{-1} were observed in the presence of andro, 19-OH andro, 19=O andro, and estrone, respectively.

Steady-State Kinetics of P450 19A1 Activity—Although in range of previously reported k_{cat} values (Figure 48 and Table 3) (51, 55, 61), the turnover of andro by P450 19A1 was relatively slow (0.06 s^{-1}), particularly when compared to cholesterol 7α-hydroxylation by P450 7A1, which has been reported to be two orders of magnitude faster (169). (A sample chromatogram used for quantitation of estrone is shown in Figure 41). While the k_{cat} was somewhat low (0.06 s^{-1}), the low K_m contributed to a relatively high catalytic efficiency (1.4 × 10^6 M^{-1} s^{-1}). 19-OH andro and 19=O andro displayed higher k_{cat} values (0.13 and 0.42 s^{-1}, respectively), although lower K_m values caused the resulting catalytic efficiencies to be lower than that of andro conversion to estrone (Table 3). Thus coupling of NADPH oxidation (*vide supra*) to k_{cat} was not very efficient, with 5%, 34%, and 33% coupling for andro, 19-OH andro, and 19=O andro, respectively.

When excess 19-OH andro or 19=O andro was added at 30 or 60 s to an incubation containing P450 19A1 and tritiated andro in a pulse-chase experiment, a ~ 75% loss of the radiolabel in the estrone product was observed (Figure 49). Loss of the

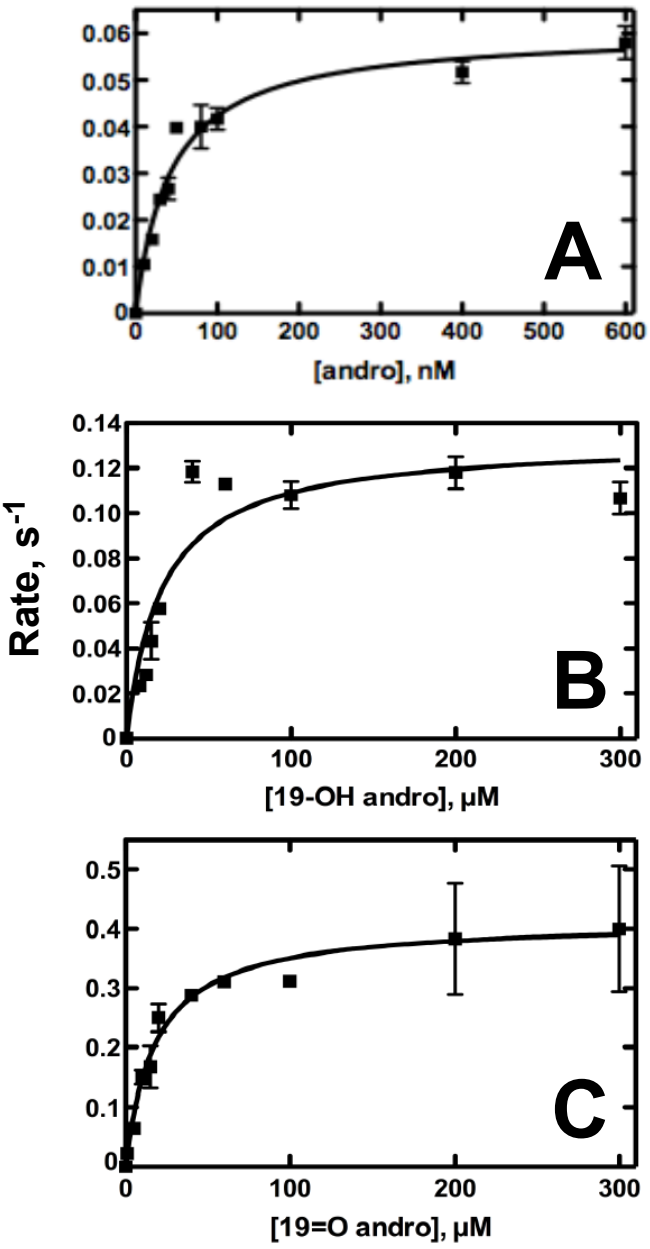

Figure 48. Steady-state kinetics of P450 19A1 activity. Hyperbolic fitting of the formation of estrone by P450 19A1. *A*, Andro as substrate; *B*, 19-OH andro as substrate; *C*, 19=O andro as substrate.

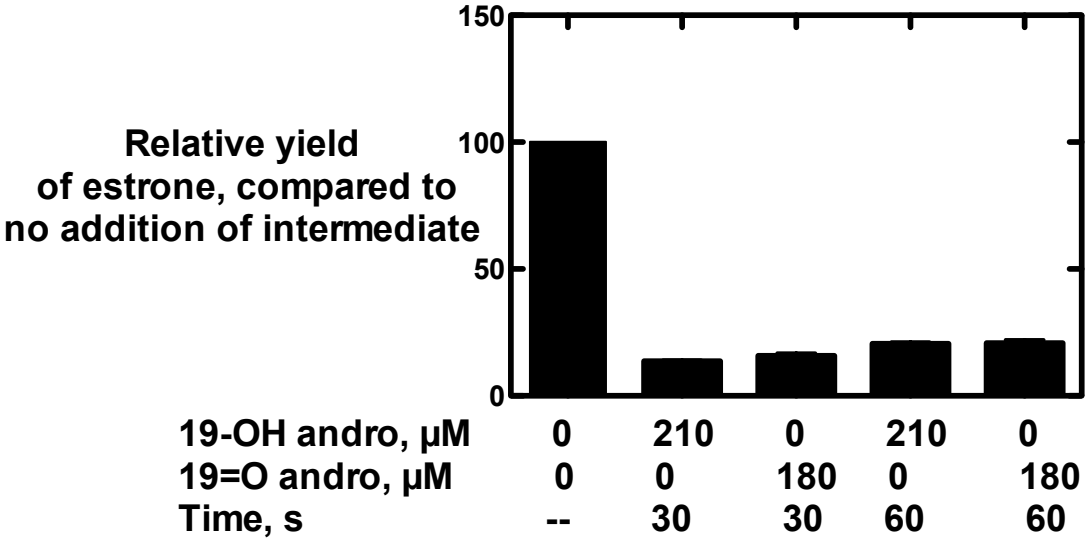

Figure 49. Pulse-chase assays. P450 19A1 (2 nM) was incubated with 400 nM [1,2,6,7-^{3}H]-andro, followed by a pulse of 19-OH andro (210 μM) or 19=O andro (180 μM) at 30 or 60 s. In this case, 100% activity was 0.087 s^{-1}. The total reaction time was 5 min.

radiolabel in the product (estrone) upon addition of either intermediate indicated that both intermediates exchange freely during the course of the sequential reaction.

Kinetics of P450 19A1 Under Single Turnover Conditions—Pre-steady-state kinetic analysis was done under single turnover conditions to generate a progress curve showing the loss of substrate, the subsequent formation and loss of 19-OH andro and 19=O andro, and the generation of estrone (Figure 50). 19-OH andro (which accumulated to higher concentrations than 19=O andro) was seen already at 100 ms, with 19=O andro and estrone formed later. The reaction was essentially complete within 10 s.

P450 19A1 Kinetic Modeling—Global fitting was employed to generate a minimal mechanism for the three-step reaction catalyzed by P450 19A1 (Figure 50 and Table 4). The single turnover time course could be fit using Kintek Explorer® software (Figure 50, fitting settings are shown in the Appendix) and the resulting individual rate constants were constrained in part by concurrently fitting (using DynaFit software) the *v vs.* substrate concentration steady-state plots (Figure 48) for the conversion of 19-OH andro and 19=O andro to estrone (Figure 51). Further, K_d values resulting from the fits for andro and 19=O andro binding were within range of those derived experimentally (Figure 43 and Table 3). The rates of P450 19A1 reduction (Figure 46) were used to set approximate upper limits of substrate oxidation (i.e. k_3, k_6, k_9, Table 4). The inclusion of a conformational change following ligand binding (Table 4) was based upon evidence for a spectroscopically-silent initial binding step in the pre-steady-state binding experiments (Figure 44), and the insertion of intermediate dissociation steps was included based on

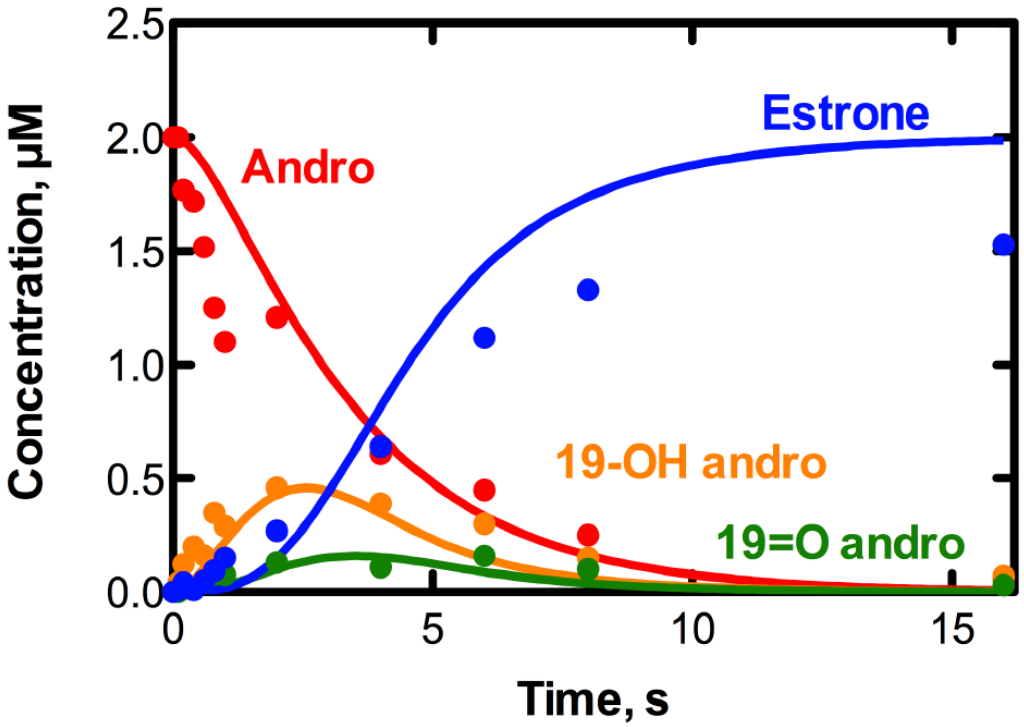

Figure 50. Kinetics of P450 19A1 catalysis under single turnover conditions. Loss and/or formation of andro (red), 19-OH andro (orange), 19=O andro (green), and estrone (blue) were monitored in a reaction of P450 19A1 (2 μM) and [4-^{14}C]-andro (2 μM). Global fitting (using Kintek Explorer® software) is shown. See the Appendix for software parameters.

Table 4. Individual rate constants for P450 19A1 turnover.

Mechanism step[a]	Forward rate constant	Reverse rate constant
$E + A \rightleftarrows EA$	$k_1 = 4.5 \times 10^7\ M^{-1}\ s^{-1}$	$k_{-1} = 15\ s^{-1}$
$EA \rightleftarrows AE$	$k_2 = 0.63\ s^{-1}$	$k_{-2} = 0.35\ s^{-1}$
$AE \rightarrow EB$	$k_3 = 1.0\ s^{-1}$	
$EB \rightleftarrows E + B$	$k_4 = 3.9 \times 10^4\ s^{-1}$	$k_{-4} = 3.5 \times 10^7\ M^{-1}\ s^{-1}$
$EB \rightleftarrows BE$	$k_5 = 2.4 \times 10^4\ s^{-1}$	$k_{-5} = 320\ s^{-1}$
$BE \rightarrow EC$	$k_6 = 7.5\ s^{-1}$	
$EC \rightleftarrows E + C$	$k_7 = 50\ s^{-1}$	$k_{-7} = 4.0 \times 10^7\ M^{-1}\ s^{-1}$
$EC \rightleftarrows CE$	$k_8 = 3.2 \times 10^4\ s^{-1}$	$k_{-8} = 3.0 \times 10^4\ s^{-1}$
$CE \rightarrow ED$	$k_9 = 5.9\ s^{-1}$	
$ED \rightleftarrows E + D$	$k_{10} = 1.3 \times 10^4$	$k_{-10} = 4.5 \times 10^7\ M^{-1}\ s^{-1}$

[a]A: andro, B: 19-OH andro, C: 19=O andro, D: estrone, E: enzyme (P450 19A1).

A

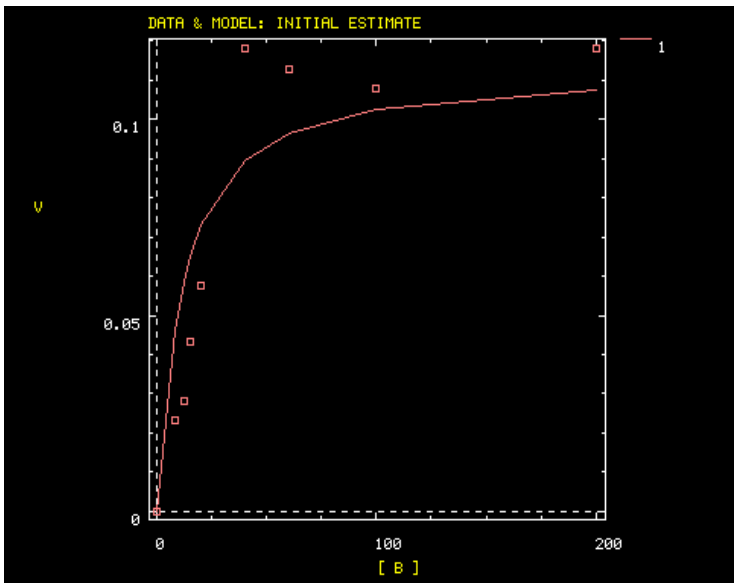

B

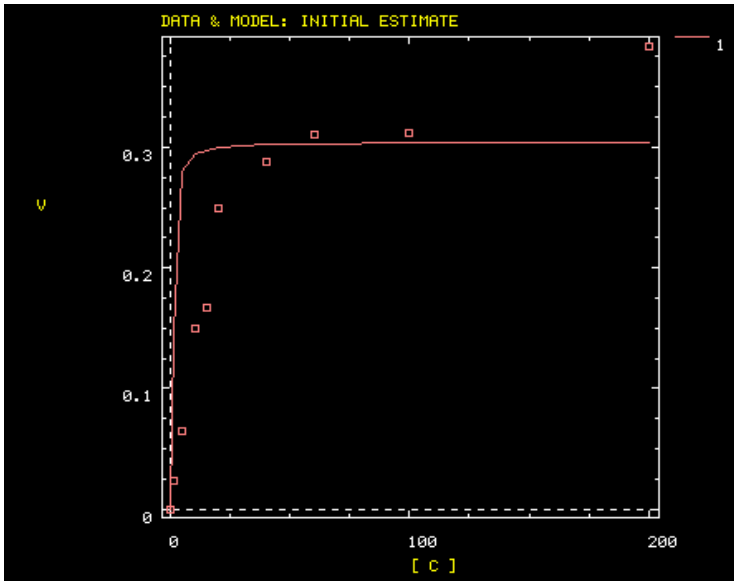

Figure 51. DynaFit iterations for global fitting. Corresponding scripts can be found in the Appendix. For all plots, the y axis is rate in s^{-1} and the x axis is the ligand concentration in μM. *A*, Resulting fit for the conversion of 19-OH andro to estrone using rate constants from the single turnover experiment fit (Figure 50 and Table 4). *B*, Resulting fit for the conversion of 19=O andro to estrone, using rate constants from the single turnover experiment fit (Figure 50 and Table 4).

the results of the pulse-chase experiments (Figure 49).

Discussion

P450 19A1, which converts androgens to estrogens, is a member of the class of P450s capable of catalyzing sequential reactions. Many of these multi-step enzymes are involved in steroid processing, i.e. P450s 11A1, 11B2, 17A1, and 51A1, as well as P450 19A1. The reported kinetic studies of three-step reactions catalyzed by P450 19A1 are limited to a small collection of steady-state parameters associated with the turnover of andro and testosterone plus a multitude of studies examining aromatase inhibitors, which have proved to be therapeutically effective for some breast cancers. Both steady-state and pre-steady-state kinetic techniques were used to characterize the binding of the substrate, intermediates, and product, revealing low μM binding that occurs in a two-step process. Over the course of the reaction, the intermediates freely dissociate. Globally fitting a progress curve generated under single turnover conditions, as well as many other data, yielded a kinetic model with individual rate constants for each step of catalysis.

Reported in this chapter is the heterologous P450 19A1 expression of 400-500 nmol/l in *E. coli* and purification that requires only one chromatography step. Most other methods involve purification of P450 19A1 from placenta, which prohibits mutagenesis experiments and requires access to human tissues. Further, these purification protocols require the use of two (54), three (51, 55), or four (56) columns, decreasing the overall yield, and some utilize non-ionic detergents, which can be difficult to remove (57). The specific content (6.3 nmol P450/mg protein, Table 2) was lower than expected for a pure P450 holoenzyme, i.e. ~ 20 nmol P450/mg for a 50 kDa protein. Because SDS-PAGE analysis indicated > 95% purity (Figure 39*B*), I presume that the deviation from the

theoretical value resulted from a contribution of apo-P450 19A1 to the measured concentration. P450 19A1 was sensitive to exposure to the nickel-NTA resin and although the chromatography step was abbreviated, the absorbance spectrum of the purified protein at 420 nm (demonstrating a loss of heme) suggested the presence of some apo-protein (Table 2).

Two other purification strategies required the use of either andro (55) or αNF (51) to stabilize the P450 during purification. Although the Fe^{2+}•CO *vs*. Fe^{2+} difference spectra improved upon the addition of αNF during solubilization and chromatography steps, I was unable to remove αNF from the preparation despite extensive column washing, adding a second column for further washing, and using additional dialysis steps. As andro has a K_d nearly as low as αNF (0.13 *vs*. 0.09 μM, respectively), it is likely that similar problems plague purification strategies that utilize andro. Limiting exposure to the nickel-NTA resin generated Fe^{2+}•CO *vs*. Fe^{2+} difference spectra of as high quality as those recorded with αNF-containing preparations (minimum A_{420} in the Fe^{2+}•CO *vs*. Fe^{2+} difference spectra) and, importantly, did not complicate kinetics by having an inhibitor or substrate present.

Another protocol for expression and purification of P450 19A1 in *E. coli* involved the removal of a larger portion of the *N*-terminus, produced slightly lower levels of expression (350-400 nmol/l), and required three columns and the presence of andro (60, 61). While Zhang et al. (62) used only a single column for purification, the native sequence was more highly modified in that histidine tags were present at both the *N*- and *C*-termini, and expression levels were not reported.

One steady-state time course assay involving aromatization of andro (by placental microsomes) showed accumulation of both intermediates before the formation of estrone (39), but another study extended this time course to show subsequent loss of the intermediates (40). The presence of both intermediates, the lag of formation of estrone, and the subsequent loss of the intermediates was taken as evidence that each step of the sequential reaction was required and that the intermediates were free to dissociate. Conversely, the high specific activity of estrone and low specific activity of 19-OH andro after incubation of radiolabeled andro and non-labeled 19-OH andro (with placental microsomes) suggested little dissociation of the intermediates (41). However, this type of assay does not directly probe dissociation of both intermediates, unlike pulse-chase experiments (Figure 49). The amount of 19A1 present was not defined (microsomal fractions were used), which could prove problematic. If substrate concentrations approximate the concentration of P450 19A1, conditions would be similar to those in the single turnover experiment described here, and a 5-min incubation would be too long for this type of assay. In the time course experiment reported here (Figure 50) this relatively late time point would show more radioactive estrone than radioactive 19-OH andro, as indicated in the study by Hollander (41), but this observation should not be used to infer processivity. My more direct assay of measuring dissociation using pulse-chase experiments (with defined concentrations), which shows dissociation of both intermediates, is considered more reliable.

Characterization of P450 19A1 as being more distributive than processive contrasts with similar studies on sequential reactions catalyzed by P450s 2A6 (processive conversion of nitrosamines to aldehydes and then carboxylic acids (33)) and 2E1

(processive conversion of ethanol to acetic acid through acetaldehyde (34)). Intuitively one might expect a reaction course with a physiological substrate to be more processive, but this is not necessarily the case. Why these P450s show such differences in the ability of the intermediates to freely exchange remains unknown and is the object of further investigation.

Distinction between the ferric peroxide and the Compound I mechanisms (*vide supra*) was not addressed in this work. Because the former mechanism (152, 153) dictates that the ferric peroxide intermediate attacks the 19=O andro intermediate rather than the 19-*gem*-diol compound, it is possible that buildup of the 19-*gem*-diol might occur (if dehydration is slow). However no unidentified peaks in the radiochromatogram were observed to indicate a distinct 19-*gem*-diol compound in the single turnover studies. The sensitivity of the assay may have prevented observation of the 19-*gem*-diol (the specific activity of the [4-^{14}C]-andro was very low), because 19=O andro levels were just above the limit of detection. It is also possible that the rate of non-enzymatic conversion might favor the 19=O andro compound, preventing buildup of the 19-*gem*-diol. Another possibility is that the 19-*gem*-diol is immediately attacked by Compound I, as in the case of the second proposed mechanism (154), and the enzymatically non-preferred conformation, the 19=O andro, accumulates (as seen in Figure 50). Further experiments are necessary to distinguish between these two models.

Steady-state titrations (Figure 43) showed low μM dissociation constants for all four ligands. The highest affinity was seen for andro (0.13 μM), a value that is still much higher than the circulating concentration of andro (~ 9 nM in men (170)). Titrations with testosterone (data not shown) indicated a K_d value of 1.5 μM, which is considerably

higher than that of andro, although circulating levels of testosterone are also higher (~ 19 nM in men (170)). Pre-steady-state binding of andro, 19-OH andro, and 19=O andro to P450 19A1 was a two-step process. Thus multi-step binding to P450s is not limited to xenobiotics (i.e. P450s 1A2, 3A4) (32, 91), as this was also seen with an endobiotic in a P450 with a small active site (24).

In order to generate a minimum kinetic model to describe P450 19A1 turnover, multiple types of data were fit globally using both Kintek Explorer® (Figure 50 and Appendix) and DynaFit software (Figure 51 and Appendix). The greatest challenge of global fitting was constraining the individual rate constants to fit the steady-state turnover data (Figures 48 and 51). For the steady-state 19-OH andro to estrone conversion data, all of the rate constants from the EB ⇆ E + B step (Table 4) through the final step (estrone release) were used. The resulting fit (Figure 51*A*) describes the turnover of 19-OH andro relatively well. Similarly, 19=O to estrone turnover data were fit using rate constants from the EC ⇆ E + C step (Table 4) through estrone release. While the initial rate is slightly faster than observed experimentally, these steady-state data were also fit well (Figure 51*B*).

There are some weaknesses of this kinetic model. While concentrations of the two intermediates were well described by the model of the single turnover experiment, a lag phase in the formation of estrone was overemphasized and the rate of andro loss was slow (Figure 50). Laws of mass balance dictate that 2 μM estrone should be formed as indicated by the model because levels of andro, 19-OH andro, and 19=O andro fall to zero, and no further reaction with estrone could be identified. However, slow conversion of estrone to 2-hydroxyestrone by P450 19A1 has been reported (171-173), and it is

possible that some estrone 2-hydroxylation occurred, albeit at undetectable levels in these assays. It is unlikely that significant intermediate decomposition occurred during the course of the single turnover experiment because no additional peaks (^{14}C) were identified to indicate novel compounds (resulting from decomposition). Additional "conformational change" steps could be added following binding each of the ligands, or at other steps of the catalytic cycles, which may improve the overall fit, but have no experimental basis. The convention of global kinetic simulation is to develop the best possible minimal mechanism that can fit several types of experimental data, without adding additional steps unless necessary and justified (174). Analysis using substrate with higher specific radioactivity might reveal contributions from other products (of andro, the intermediates, or estrone), although I have used the highest specific radioactivity ^{14}C-labeled andro available. The use of tritium-labeled materials have the disadvantages of potential loss of labels resulting from exchange or isotope effects (depending on the site of labeling).

These rate constants (Table 4) could not be used to fit the steady-state andro to estrone conversion (Figure 48*A*) using DynaFit software, and K_d values for 19-OH andro and estrone were under predicted. In the case of estrone, the K_d problem may be solved by the addition of an ED ⇆ DE rearrangement step prior to estrone dissociation, as seen in the cases of the other ligands, but stopped-flow spectroscopy data would need to support this approach.

In summary, the first kinetic mechanism for P450 19A1 is reported resulting from the global fitting of K_d values, pre-steady-state ligand binding experiments, iron reduction rates, steady-state turnover experiments, pulse chase assays, and a single turnover time

course. The P450 19A1 mechanism, which includes rate constants for each of the three steps in the sequential reaction, may be useful for modeling other sequential P450s and may aid in the characterization of aromatase inhibitors.

CHAPTER V

SUMMARY AND CONCLUSIONS

The characterization of the kinetics of turnover by P450s 1A2 and 19A1 is described in Chapters II-IV. Rabbit liver cytochrome P450 (P450) 1A2 was found to be capable of catalyzing sequential reactions. In addition to the one-step 5,6-epoxidation of αNF, P450 1A2 catalyzes the 1-hydroxylation of pyrene and the subsequent 6-, 8-, and other hydroxylations of 1-hydroxy (OH) pyrene. While plots of rates of *v vs*. substrate concentration were hyperbolic for αNF epoxidation, pyrene and 1-OH pyrene hydroxylation proved to be highly sigmoidal, indicative of positive cooperativity (Hill *n* coefficients of 2-4). Pre-steady state binding of αNF, pyrene, or 1-OH pyrene to ferric P450 1A2 yielded changes in the heme Soret spectra that were relatively slow and multiphasic, while changes in fluorescence were much faster, consistent with rapid initial binding to P450 1A2 in a way that does not affect the heme spectrum. Sequential changes in opposite directions were seen for binding of pyrene to ferrous P450 1A2, indicative of the enzyme being involved in a series of transitions resulting in the observed multiphasic spectra (as opposed to multiple, slowly interconverting populations of enzyme undergoing the same event at different rates). An available crystal structure of a human P450 1A2-αNF (23) was used to generate a model of rabbit P450 1A2, which showed that one αNF or two pyrenes could be docked into the active site. The spectral changes observed for binding and hydroxylation of pyrene and 1-OH pyrene could be fit to a

kinetic model in which hydroxylation occurs only when two substrates are bound. Elements of this mechanism may be relevant to other cases of P450 cooperativity.

Cooperativity studies on rabbit P450 1A2 were extended to clarify previous findings of homotropic cooperativity with $(CH_3)_2CH$-O-$PhNO_2$ and heterotropic cooperative binding interactions with $Ph(NC)_2$ (47). Binding of $Ph(NC)_2$ to ferric and ferrous forms of P450 1A2 revealed multiphasic kinetics with relatively slow steps. $Ph(NC)_2$ induced an apparently rapid change in the CD spectrum, consistent with a structural change, but no effect was seen in tryptophan fluorescence. While ferric P450 1A2 was rapidly reduced in the absence of ligands, the rate was attenuated in the presence of $Ph(NC)_2$. $Ph(NC)_2$ did not prove to be a substrate for P450 1A2. Similar docking studies (*vide supra*) with P450 1A2 indicated adequate space for a complex with either two $(CH_3)_2CH$-O-$PhNO_2$ molecules or a combination of one $(CH_3)_2CH$-O-$PhNO_2$and one $Ph(NC)_2$ molecule. The homotropic cooperativity seen with $(CH_3)_2CH$-O-$PhNO_2$ dealkylation (biphasic plots of *v vs*. substrate concentration) differed from those seen with pyrene oxidation (positive cooperativity), suggesting that only with the latter does the ligand interaction result in improved catalysis. $Ph(NC)_2$ inhibited the oxidation of $(CH_3)_2CH$-O-$PhNO_2$ and other substrates.

Cytochrome P450 19A1 (P450 19A1), the aromatase, catalyzes the conversion of androgens to estrogens through a sequential three-step reaction, generating 19-hydroxy and 19-aldehyde intermediates en route to the product estrogen. A procedure for the heterologous expression and purification of active P450 19A1 in *E. coli* was developed. Binding of the substrate and intermediates showed low μM dissociation constants and were at least two-step processes. Rates of reduction of the iron were fast in the presence

of substrate, either intermediate, or product. P450 19A1 is a distributive rather than a processive enzyme, with the sequential reaction allowing free dissociation of the intermediates as revealed by pulse-chase experiments. Conversion of androstenedione to estrone (under single turnover conditions) generated a progress curve showing changes in the concentrations of the substrate, intermediates, and product. A minimal kinetic model containing the individual rate constants for the steps in P450 19A1 catalysis was developed to globally fit the time course of the overall reaction, the dissociation constants, the two-step ligand binding, the distributive character, the iron reduction rates, and the steady-state conversion of the 19-OH andro and 19=O andro intermediates to estrone.

Several questions remain in the P450 19A1 studies. The chemical mechanism of the third step of P450 19A1 remains unknown; as discussed in Chapter IV, the proper experiments were not performed to distinguish between the two mechanisms. Several experiments are planned or underway to elucidate this final step in the sequential reaction. A solution of 19=O andro in buffered $H_2{}^{18}O$ will be analyzed using MS at various timepoints. This will allow the measurement of the rate of exchange of 19=O andro and the 19-*gem*-diol andro forms. Comparison of the rates with and without P450 19A1 will discern whether the enzyme can accelerate these exchange rates. Similar studies will be undertaken using $H_2{}^{17}O$ and ^{1}H-NMR to determine rates of exchange (although only in the absence of enzyme). A preliminary experiment using ^{1}H-NMR showed that 19=O andro in buffered D_2O ($\leq$ 5% organic solvent v/v) is entirely in the aldehyde form (no 19-*gem*-diol formation).

A key difference of the two mechanisms currently favored is the source of the oxygen in the formic acid that is released in the third step (see Chapter IV for more detail). The specifics of the two mechanisms are shown in Figure 52. As shown in the first proposed mechanism (Figure 52*A*, (152, 153)) the 19=O andro rather than the 19-*gem*-diol is required for the reaction to occur, and there is incorporation of one labeled oxygen in the formic acid. In the second proposed mechanism (154) (Figure 52*B*), there is instead a requirement for the 19-*gem*-diol rather than the 19=O andro intermediate for the reaction to take place. In this case, there is no incorporation of a labeled oxygen in the released formic acid. The use of $^{18}O_2$ in an incubation of P450 19A1 with andro followed by LC-MS analysis will be used to determine if ^{18}O is incorporated into formic acid during the sequential reaction.

The slow 2-hydroxylation of estrone by P450 19A1 has been known for many years, although little detail is available on the kinetics of this reaction (171-173). No evidence of additional products were identified in the single turnover experiments (Chapter IV), perhaps due to sensitivity problems. Studies with P450 19A1 have since been expanded to characterize estrone as a substrate for P450 19A1. Shown in Figure 53 is a *v vs*. substrate concentration plot for this reaction, with k_{cat} = 0.046 min^{-1}, K_m = 2.7 μM, and $k_{cat}/K_m = 1.7 \times 10^4$ min^{-1} M^{-1}. Both the reaction rate and the efficiency are much lower than those measured for andro, 19-OH andro, and 19=O andro.

Several studies have noted the ability of P450 19A1 to convert 19-nor-androstenedione to estrone (53, 175-179). Most studies cite much slower rates of conversion compared to andro turnover (~60-fold slower), although pig (178) and horse

A

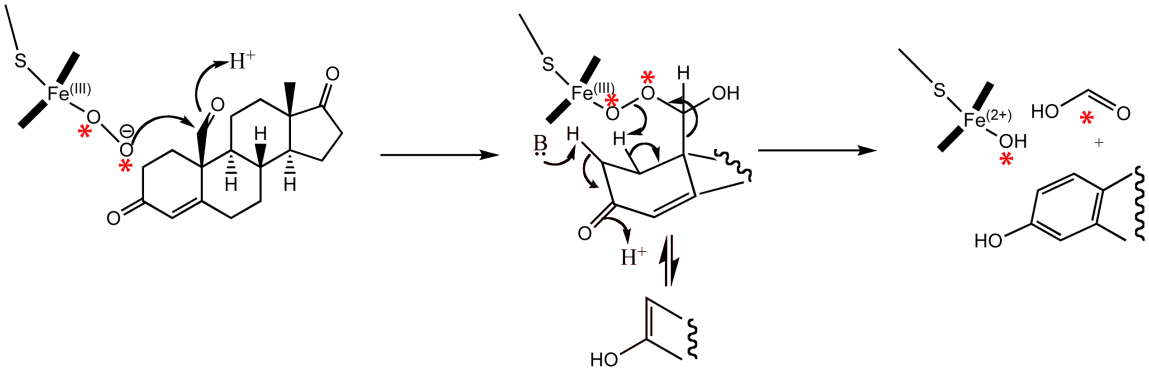

B

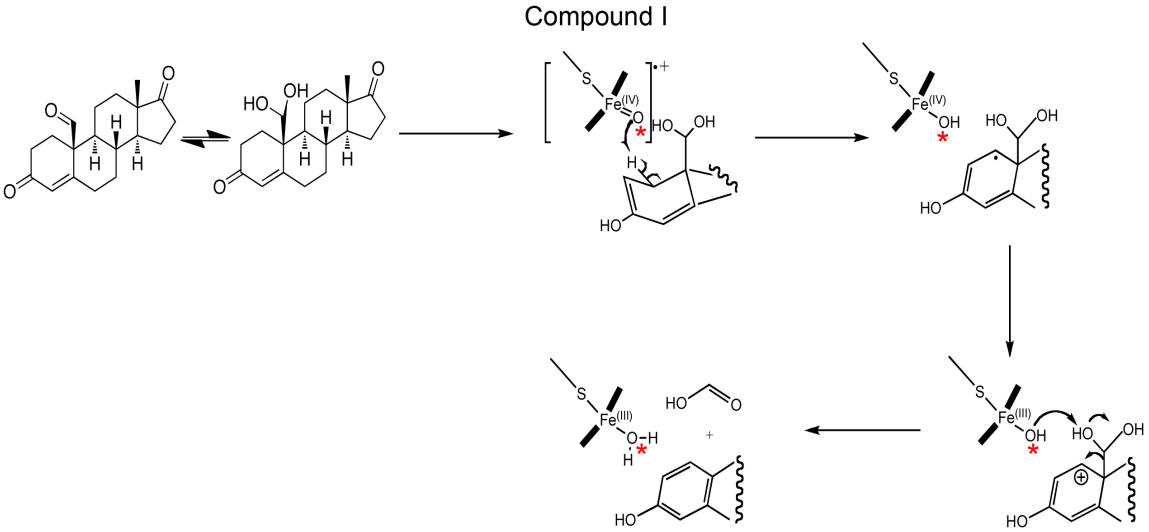

Figure 52. Details of the proposed third step of P450 19A1 turnover. *A*, Proposed mechanism in (152, 153). In this case, the 19=O andro form is required, and there is incorporation of one labeled oxygen (denoted with a red star) into the formic acid. *B*, Proposed mechanism in (154). Here the 19-*gem*-diol andro is required, and there is no incorporation of labeled oxygen.

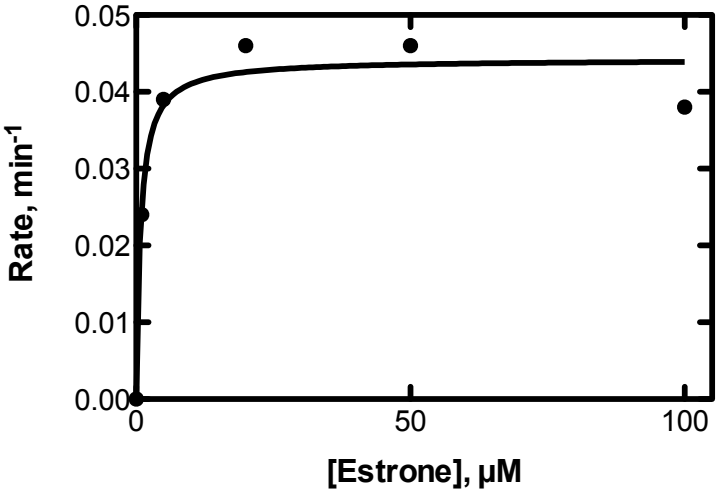

Figure 53. Conversion of estrone to 2-hydroxyestrone by P450 19A1. k_{cat} = 0.046 min^{-1}, K_m = 2.7 μM, and $k_{cat}/K_m = 1.7 \times 10^4$ min^{-1} M^{-1}.

(176, 177, 179) P450 19A1 show no substrate preference. Steady-state parameters in standard units (i.e. nmol product/nmol P450/time, rather than nmol product/mg protein/time) had not been determined for human P450 19A1. The results of a (steady-state) incubation of P450 19A1 and varying concentrations of 19-nor-androstenedione are shown in Figure 54, with k_{cat} = 0.145 min^{-1}, K_m = 1.1 μM, and k_{cat}/K_m = 1.3 × 10^5 min^{-1} M^{-1}. As in the case with 2-hydroxylation of estrone, the overall rate and efficiency is low.

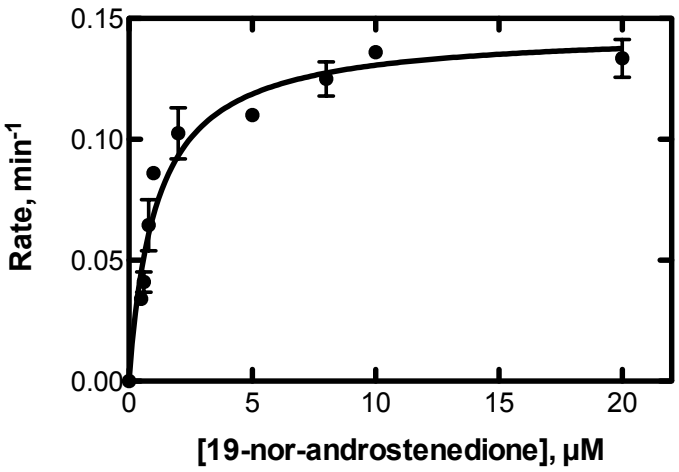

Figure 54. Conversion of 19-norandrostenedione to estrone by P450 19A1. k_{cat} = 0.145 min^{-1}, K_m = 1.1 μM, and k_{cat}/K_m = 1.3 × 10^5 min^{-1} M^{-1}.

In addition to characterizing the third step of P450 19A1 catalysis and identifying new substrates, many important topics remain for understanding P450 19A1. There is much interest in developing tissue-specific aromatase inhibitors to diminish side effects including loss of bone mass. Polymorphisms in this enzyme may be related to several diseases including breast cancer, Alzheimer's disease, and prostate cancer. Now that P450 19A1 can be easily expressed, such polymorphisms can be examined in detail in an *in vitro* setting.

The development of mechanisms of multi-step turnover by globally fitting many types of data for both P450s 1A2 and 19A1 are the key elements of the prior chapters. Few such kinetic studies exist for P450s that catalyze sequential reactions, which typically involve steroids as substrates. These types of mechanisms can serve as models for novel studies on these important P450s (which include 51A1, which is the key enzyme in cholesterol biosynthesis). An in-depth kinetic analysis of P450 19A1 is also important for the development of new therapeutics (aromatase inhibitors) for estrogen-dependent breast cancer. Because P450 1A2 plays an important role in the clearance of pollutants and drugs, finding significant cooperative behavior with this enzyme can affect both the setting of proper exposure limits and dosing of drugs. This works shows that the proper use of steady-state and pre-steady-state kinetics can help clarify the complexities of multi-turnover cytochrome P450s.

PUBLICATIONS

Refereed Publications

1. Wu, Z-L., Sohl, C. D., Shimada, T., and Guengerich, F. P. (2006) Recombinant enzymes over-expressed in bacteria show broad catalytic specificity of human cytochrome P450 2W1 and limited activity of human cytochrome P450 2S1. *Mol Pharmacol,* **69**, 2007-2014.

2. Isin, E. M., [*]Sohl, C. D., Eoff, R. L., and Guengerich, F. P. (2008) Cooperativity of cytochrome P450 1A2: interaction of 1,4-phenylene diisocyanide and 1-alkoxy-4-nitrobenzenes. *Arch Biochem Biophys,* **473**, 69-75. ([*]co-first author)

3. Sohl, C. D., Isin, E. M., Eoff, R. L., Marsch, G. A., Stec, D. F., and Guengerich, F. P. (2008) Cooperativity in oxidation reactions catalyzed by cytochrome P450 1A2. Highly cooperative pyrene hydroxylation and multiphasic kinetics of ligand binding. *J Biol Chem,* **283**, 7293-7308.

4. Sohl, C. D., and Guengerich, F. P. (2010) Kinetic analysis of the three-step steroid aromatase reaction of human cytochrome P450 19A1. *J Biol Chem,* **285**, 17734-17743.

Invited Reviews

1. Guengerich, F. P., Sohl, C. D., and Cheng, Q. (2009) Measurement of cytochrome P450 and NADPH-cytochrome P450 reductase. *Nat Protoc,* **4**, 1245-51.

2. Sohl, C. D., Cheng, Q., and Guengerich, F. P. (2009) Chromatographic assays of drug oxidation by human cytochrome P450 3A4. *Nat Protoc,* **4**, 1252-7.

3. Cheng, Q., Sohl, C. D., and Guengerich, F. P., (2009) High-throughput fluorescence assay of cytochrome P450 3A4. *Nat Protoc,* **4**, 1258-61.

4. Guengerich, F. P., Sohl, C. D., and Chowdhury, G. (2010, in preparation) Multi-step oxidations catalyzed by cytochrome P450 enzymes: Processive *vs.* distributive kinetics and the issue of carbonyl oxidation in chemical mechanisms. *Arch Biochem Biophys*.

REFERENCES

1. Nelson, D. R. (2003) Comparison of P450s from human and fugu: 420 million years of vertebrate P450 evolution. *Arch Biochem Biophys,* **409**, 18-24.

2. Garfinkel, D. (1958) Studies on pig liver microsomes. I. Enzymatic and pigment composition of different microsomal fractions. *Arch Biochem Biophys,* **77**, 493-509.

3. Klingenberg, M. (1958) Pigments of rat liver microsomes. *Arch Biochem Biophys,* **75**, 376-386.

4. Omura, T. and Sato, R. (1962) A new cytochrome in liver microsomes. *J Biol Chem,* **237**, 1375-1376.

5. Omura, T. and Sato, R. (1964) The carbon monoxide-binding pigment of liver microsomes. I. Evidence for its hemoprotein nature. *J Biol Chem,* **239**, 2370-2378.

6. Omura, T. and Sato, R. (1964) The carbon monoxide-binding pigment of liver microsomes. II. Solubilization, purification, and properties. *J Biol Chem,* **239**, 2379-2385.

7. Estabrook, R. W., Cooper, D. Y., and Rosenthal, O. (1963) The light reversible carbon monoxide inhibition of the steroid C21-hydroxylase system of the adrenal cortex. *Biochem Z*, **338**, 741-755.

8. Phillips, A. H. and Langdon, R. G. (1962) Hepatic triphosphopyridine nucleotide-cytochrome *c* reductase: isolation, characterization, and kinetic studies. *J Biol Chem*, **237**, 2652-2660.

9. Lu, A. and Coon, M. J. (1968) Role of hemoprotein P-450 in fatty acid ω-hydroxylation in a soluble enzyme system from liver microsomes. *J Biol Chem*, **243**, 1331-1332.

10. Vermilion, J. L. and Coon, M. J. (1974) Highly purified detergent-solubilized NADPH-cytochrome P-450 reductase from phenobarbital-induced rat liver microsomes. *Biochem Biophys Res Commun*, **60**, 1315-1322.

11. Haugen, D. A., van der Hoeven, T. A., and Coon, M. J. (1975) Purified liver microsomal cytochrome P-450: separation and characterization of multiple forms. *J Biol Chem*, **250**, 3567-3570.

12. Guengerich F. P. (1977) Separation and purification of multiple forms of microsomal cytochrome P-450. Activities of different forms of cytochrome P-450 towards several compounds of environmental interest. *J Biol Chem*, **252**, 3970-3979.

13. Ryan, D., Lu, A., Kawalek, J., West, S. B., and Levin, W. (1975) Highly purified cytochrome P-448 and P-450 from rat liver microsomes. *Biochem Biophys Res Commun*, **64**, 1134-1141.

14. Lu, A, Ryan, D., Kawalek, J. Thomas, P., West, S. B., Huang, M. T., and Levin, W. (1976) Multiplicity of liver microsomal cytochrome P-450: separation, purification and characterization. *Biochem Soc Trans*, **4**, 169-172.

15. Shimada, T., Misono, K. S., and Guengerich, F. P. (1986) Human liver microsomal cytochrome P-450 mephenytoin 4-hydroxylase, a prototype of genetic polymorphism in oxidative drug metabolism. Purification and characterization of two similar forms involved in the reaction. *J Biol Chem,* **261**, 909-921.

16. Distlerath, L. M., Reilley, P. E., Martin, M. V., Davis, G. G., Wilkinson, G. R., and Guengerich, F. P. (1985) Purification and characterization of the human liver cytochromes P-450 involved in debrisoquine 4-hydroxylation and phenacetin *O*-deethylation, two prototypes for genetic polymorphism in oxidative drug metabolism. *J Biol Chem*, **260**, 9057-9067.

17. Guengerich, F. P., Martin, M. V., Beaune, P. H., Kremers, P., Wolff, T., and Waxman, D. J. (1986) Characterization of rat and human liver microsomal cytochrome P-450 forms involved in nifedipine oxidation, a prototype for genetic polymorphism in oxidative drug metabolism. *J Biol Chem*, **261**, 5051-5060.

18. Poulos, T. L., Finzel, B. C., Gunsalus, I. C., Wagner, G. C., and Kraut, J. (1985) The 2.6-Å crystal structure of *Pseudomonas putida* cytochrome P-450. *J Biol Chem*, **260**, 16122-16130.

19. Poulos, T. L., Finzel, B. C., and Howard, A. J. (1987) High-resolution crystal structure of cytochrome $P450_{cam}$. *J Mol Biol*, **195**, 687-700.

20. Li, H., Narasimhulu, S., Havran, L. M., Winkler, J. D., and Poulos, T. L. (1995) Crystal structure of cytochrome $P450_{cam}$ complexed with its catalytic product, 5-*exo*-hydroxycamphor. *J Am Chem Soc*, **117**, 6297-6299.

21. Cupp-Vickery, J. R. and Poulos, T. L. (1995) Structure of cytochrome P450eryF involved in erythromycin biosynthesis. *Nat Struct Biol*, **2**, 144-153.

22. Williams, P. A. , Cosme, J., Sridhar, V., Johnson, E. F., and MeRee, D. E. (2000) Mammalian microsomal cytochrome P450 monooxygenase: strutural adaptations for membrane binding and functional diversity. *Mol Cell*, **5**, 121-131.
23. Sansen, S., Yano, J. K., Reynald, R. L., Schoch, G. A., Griffin, K. J, Stout, C. D., and Johnson, E. F. (2007) Adaptations for the oxidation of polycyclic aromatic hydrocarbons exhibited by the structure of human P450 1A2. *J Biol Chem*, **282**, 14348-14355.

24. Ghosh, D., Griswold, J., Erman, M., and Pangborn, W. (2009) Structural basis for androgen specificity and oestrogen synthesis in human aromatase. *Nature*, **457**, 219-223.

25. Guengerich, F. P. (2003) Cytochrome P450s, drugs, and diseases. *Mol Interventions*, **3**, 8-18.

26. Ortiz de Montellano, P. R., ed. (2005) *Cytochrome P450: Structure, Mechanism, and Biochemistry*. 3rd Ed., KluwerAcademic/Plenum Publishers, New York.

27. Guengerich, F. P., Wu, Z-L., and Bartleson, C. J. (2005) Function of human cytochrome P450s: characterization of the remaining orphans. *Biochem Biophys Res Commun*, **338**, 465-469.

28. Yano, J. K., Hsu, M. H., Griffin, K. J., Stout, C. D., and Johnson, E. F. (2005) Structures of human microsomal cytochrome P450 2A6 complexed with coumarin and methoxsalen. *Nat Struct Biol*, **12**, 822-823.

29. Porubsky, P. R., Meneely, K. M., and Scott, E. E. (2008) Structures of human cytochrome P-450 2E1. Insights into the binding of inhibitors and both small molecular weight and fatty acid substrates. *J Biol Chem*, **283**, 33698-33707.

30. Guengerich, F. P. (2001) Common and uncommon cytochrome P450 reactions related to metabolism and chemical toxicity. *Chem Res Toxicol*, **14**, 611-650.

31. Guengerich, F. P. and Macdonald, T. L. (1984) Chemical mechanisms of catalysis by cytochromes P-450: a unified view. *Acc Chem Res*, **17**, 9-16.

32. Sohl, C. D., Isin, E. M., Eoff, R. L., Marsch, G. A., Stec, D. F., and Guengerich, F. P. (2008) Cooperativity in oxidation reactions catalyzed by cytochrome P450 1A2. Highly cooperative pyrene hydroxylation and multiphasic kinetics of ligand binding. *J Biol Chem*, **283**, 7293-7308.

33. Chowdhury, G., Calcutt, M. W., and Guengerich, F. P. (2010) Oxidation of *N*-nitrosodimethylamine and *N*-nitrosodiethylamine by human cytochrome P450 2A6: sequential oxidation to carboxylic acids and analysis of reaction steps. *J Biol Chem*, **285**, 8031-8044.

34. Bell-Parikh, L. C. and Guengerich, F. P. (1999) Kinetics of cytochrome P450 2E1-catalyzed oxidation of ethanol to acetic acid via acetaldehyde. *J Biol Chem*, **274**, 23833-23840.

35. Imai, T., Yamazaki, T., and Kominami, S. (1998) Kinetic studies on bovine cytochrome $P450_{11B}$ catalyzing successive reactions from deoxycorticosterone to aldosterone. *Biochemistry*, **37**, 8097-8104.

36. Yamazaki, T., Ohno, T., Sakaki, T., Akiyoshi-Shibata, M., Yabusaki, Y., Imai, T., and Kominami, S. (1998) Kinetic anaylsis of successive reactions catalyzed by bovine cytochrome $P450_{17\alpha,lyase}$. *Biochemistry*, **37**, 2800-2806.

37. Tagashira, H., Kominami, S., and Takemori, S. (1995) Kinetic studies of cytochrome $P450_{17\alpha,lyase}$-dependent androstenedione formation from progesterone. *Biochemistry*, **34**, 10939-10945.

38. Soucy, P. and Luu-The, V. (2000) Conversion of pregnenolone to DHEA by human 17 α-hydroxylase/17,20-lyase (P450c17). Evidence that DHEA is produced from the released intermediate, 17-α-hydroxypregnenolone. *Eur J Biochem*, **267**, 3243-3247.

39. Thompson, E. A., Jr., and Siiteri, P. K. (1974) Utilization of oxygen and reduced nicotinamide adenine dinucleotide phosphate by human placental microsomes during aromatization of androstenedione. *J Biol Chem*, **249**, 5364-5372.

40. Braselton, W. E., Jr., Engel, L. L., and Orr, J. C. (1974) The flux of intermediates and products in aromatizaton of C19 steroids by human placental microsomes. *Eur J Biochem*, **48**, 35-43.

41. Hollander, N. (1962) Role of 19-hydroxy, Δ^4-androstene-3, 17-dione as an intermediate for aromatization of Δ^4-androstene-3, 17-dione by placental microsomes. *Endocrinology*, **71**, 723-728.

42. Gillam, E. M. J., Baba, T., Kim, B-R., Ohmori, S., and Guengerich, F. P. (1993) Expression of modified human cytochrome P450 3A4 in *Escherichia coli* and purification and reconstitution of the enzyme. *Arch Biochem Biophys,* **305**, 123-131.

43. Schenkman, J. B., Remmer, H., and Estabrook, R. W. (1967) Spectral studies of drug interaction with hepatic microsomal cytochrome P-450. *Mol Pharmacol,* **3**, 113-123.

44. Kuzmic, P. (1996) Program DYNAFIT for the analysis of enzyme kinetic data: application to HIV protease. *Anal Biochem,* **237**, 260-273.

45. Johnson, K. A., Simpson, Z. B., and Blom, T. (2009) Global Kinetic Explorer: A new computer program for dynamic simulation and fitting of kinetic data. *Anal Biochem,* **387**, 20-29.

46. Fersht, A. (1999) *Structure and mechanism in protein science*. W. H. & Co., Freeman, New York.

47. Miller, G. P. and Guengerich, F. P. (2001) Binding and oxidation of alkyl 4-nitrophenyl ethers by rabbit cytochrome P450 1A2: evidence for two binding sites. *Biochemistry,* **40**, 7262-7272.

48. Shimada, T., Yamazaki, H., Foroozesh, M., Hopkins, N. E., Alworth, W. L., and Guengerich, F. P. (1998) Selectivity of polycyclic inhibitors for human cytochromes P450 1A1, 1A2, and 1B1. *Chem Res Toxicol,* **11**, 1048-1056.

49. Alterman, M. A. and Dowgii, A. I. (1990) A simple and rapid method for the purification of cytochrome P-450 (form LM4). *Biomed Chromatogr,* **4**, 221-222.

50. Vickery, L. E. and Kellis, J. T., Jr. (1987) Aromatase cytochrome P-450. Purification and characterization of the enzyme from human placenta. *Steroids,* **50**, 29-36.

51. Gartner, C. A., Thompson, S. J., Rettie, A. E., and Nelson, S. D. (2001) Human aromatase in high yield and purity by perfusion chromatography and its characterization by difference spectroscopy and mass spectrometry. *Protein Expression Purif,* **22**, 443-454.

52. Hagerman, D. D. (1987) Human placenta estrogen synthetase (aromatase) purified by affinity chromatography. *J Biol Chem,* **262**, 2398-2400.

53. Harada, N. (1988) Novel properties of human placental aromatase as cytochrome P-450: purification and characterization of a unique form of aromatase. *J Biochem,* **103**, 106-113.

54. Yoshida, N. and Osawa, Y. (1991) Purification of human placental aromatase cytochrome P-450 with monoclonal antibody and its characterization. *Biochemistry,* **30**, 3003-3010.

55. Kellis, J. T., Jr. and Vickery, L. E. (1987) Purification and characterization of human placental aromatase cytochrome P-450. *J Biol Chem,* **262**, 4413-4420.

56. Tan, L. and Muto, N. (1986) Purification and reconstitution properties of human placental aromatase: a cytochrome P-450-type monooxygenase. *Eur J Biochem,* **157**, 243-250.

57. Hosea, N. A. and Guengerich, F. P. (1998) Oxidation of non-ionic detergents by cytochrome P450 enzymes. *Arch Biochem Biophys,* **353**, 365-373.

58. Amarneh, B. and Simpson, E. R. (1995) Expression of a recombinant derivative of human aromatase P450 in insect cells utilizing the baculovirus vector system. *Mol Cell Endocrinol,* **109**, R1-5.

59. Sigle, R. O., Titus, M. A., Harada, N., and Nelson, S. D. (1994) Baculovirus mediated high level expression of human placental aromatase (CYP19A1). *Biochem Biophys Res Commun,* **201**, 694-700.

60. Kagawa, N., Cao, Q., and Kusano, K. (2003) Expression of human aromatase (CYP19) in *Escherichia coli* by *N*-terminal replacement and induction of cold stress response. *Steroids,* **68**, 205-209.

61. Kagawa, N., Hori, H., Waterman, M. R., and Yoshioka, S. (2004) Characterization of stable human aromatase expressed in *E. coli*. *Steroids,* **69**, 235-243.

62. Zhang, F., Zhou, D., Kao, Y. C., Ye, J., and Chen, S. (2002) Expression and purification of a recombinant form of human aromatase from *Escherichia coli*. *Biochem Pharmacol,* **64**, 1317-1324.

63. Kuby, S. A. (1991) *A study of enzymes, Vol. I, Enzyme catalysis, kinetics, and substrate binding*. CRC Press, Boca Raton, FL.

64. Wiebel, F. J., Leutz, J. C., Diamond, L., and Gelboin, H. V. (1971) Aryl hydrocarbon (benzo[*a*]pyrene) hydroxylase in microsomes from rat tissues: differential inhibition and stimulation by benzoflavones and organic solvents. *Arch Biochem Biophys,* **144**, 78-86.

65. Kapitulnik, J., Poppers, P. J., Buening, M. K., Fortner, J. G., and Conney, A. H. (1977) Activation of monooxygenases in human liver by 7,8-benzoflavone. *Clin Pharmacol Ther,* **22**, 475-485.

66. Buening, M. K., Fortner, J. G., Kappas, A., and Conney, A. H. (1978) 7,8-Benzoflavone stimulates the metabolic activation of aflatoxin B_1 to mutagens by human liver. *Biochem Biophys Res Commun,* **82**, 348-355.

67. Huang, M. T., Chang, R. L., Fortner, J. G., and Conney, A. H. (1981) Studies on the mechanism of activation of microsmal benzo[*a*]pyrene hydroxylation by flavonoids. *J Biol Chem,* **256**, 6829-6836.

68. Guengerich, F. P., Kim, B-R., Gillam, E. M. J., and Shimada, T. (1994) Mechanisms of enhancement and inhibition of cytochrome P450 catalytic activity.

Proceedings, 8th Int. Conf. on Cytochrome P450: Biochemistry, Biophysics, and Molecular Biology, Lechner, M. C. Ed. John Libbey Eurotext, Paris.

69. Shou, M., Grogan, J., Mancewicz, J. A., Krausz, K. W., Gonzalez, F. J., Gelboin, H. V., and Korzekwa, K. R. (1994) Activation of CYP3A4: evidence for the simultaneous binding of two substrates in a cytochrome P450 active site. *Biochemistry,* **33**, 6450-6455.

70. Lasker, J. M., Huang, M-T., and Conney, A. H. (1982) *In vivo* activation of zoxazolamine metabolism by flavone. *Science,* **216**, 1419-1421.

71. Ngui, J. S., Tang, W., Stearns, R. A., Shou, M., Miller, R. R., Zhang, Y., Lin, J. H., and Baillie, T. A. (2000) Cytochrome P450 3A4-mediated interaction of diclofenac and quinidine. *Drug Metab Dispos,* **28**, 1043-1050.

72. Witherow, L. E. and Houston, J. B. (1999) Sigmoidal kinetics of CYP3A substrates: an approach for scaling dextromethorphan metabolism in hepatic microsomes and isolated hepatocytes to predict *in vivo* clearance in rat. *J Pharmacol Exp Ther,* **290**, 58-65.

73. Hutzler, J. M. and Tracy, T. S. (2002) Atypical kinetic profiles in drug metabolism reactions. *Drug Metab Dispos,* **30**, 355-362.

74. Atkins, W. M. (2005) Non-Michaelis-Menten kinetics in cytochrome P450-catalyzed reactions. *Annu Rev Pharmacol Toxicol,* **45**, 291-310.

75. Guengerich, F. P. (2005) *Human Cytochrome P450 Enzymes*. 3rd Ed. Kluwer Academic/Plenum Press, New York.

76. Atkins, W. M. (2006) Current views on the fundamental mechanisms of cytochrome P450 allosterism. *Expert Opin Drug Metab Toxicol,* **2**, 573-579.

77. Tracy, T. S. (2006) Atypical cytochrome P450 kinetics: implications for drug discovery. *Drugs R D,* **7**, 349-363.

78. Williams, P. A., Cosme, J., Ward, A., Angove, H. C., Matak Vinkovic, D., and Jhoti, H. (2003) Crystal structure of human cytochrome P450 2C9 with bound warfarin. *Nature,* **424**, 464-468.

79. Williams, P. A., Cosme, J., Vinkovic, D. M., Ward, A., Angove, H. C., Day, P. J., Vonrhein, C., Tickle, I. J., and Jhoti, H. (2004) Crystal structures of human cytochrome P450 3A4 bound to metyrapone and progesterone. *Science,* **305**, 683-686.

80. Yano, J. K., Wester, M. R., Schoch, G. A., Griffin, K. J., Stout, C. D., and Johnson, E. J. (2004) The structure of human microsomal cytochrome P450 3A4

determined by X-ray crystallography to 2.05-Å resolution. *J Biol Chem,* **279**, 38091-38094.

81. Johnson, E. F., Schwab, G. E., and Dieter, H. H. (1983) Allosteric regulation of the 16α-hydroxylation of progesterone as catalyzed by rabbit microsomal cytochrome P-450 3b. *J Biol Chem,* **258**, 2785-2788.

82. Schwab, G. E., Raucy, J. L., and Johnson, E. F. (1988) Modulation of rabbit and human hepatic cytochrome P-450-catalyzed steroid hydroxylations by α-naphthoflavone. *Mol Pharmacol,* **33**, 493-499.

83. Harlow, G. R. and Halpert, J. R. (1998) Analysis of human cytochrome P450 3A4 cooperativity: construction and characterization of a site-directed mutant that displays hyperbolic steroid hydroxylation kinetics. *Proc Natl Acad Sci,* **95**, 6636-6641.

84. Hosea, N. A., Miller, G. P., and Guengerich, F. P. (2000) Elucidation of distinct binding sites for cytochrome P450 3A4. *Biochemistry,* **39**, 5929-5939.

85. Koley, A. P., Buters, J. T. M., Robinson, R. C., Markowitz, A., and Friedman, F. K. (1997) Differential mechanisms of cytochrome P450 inhibition and activation by α-naphthoflavone. *J Biol Chem,* **272**, 3149-3152.

86. Fernando, H., Davydov, D. R., Chin, C. C., and Halpert, J. R. (2007) Role of subunit interactions in P450 oligomers in the loss of homotropic cooperativity in the cytochrome P450 3A4 mutant L211F/D214E/F304W. *Arch Biochem Biophys,* **460**, 129-140.

87. Jushchyshyn, M. I., Hutzler, J. M., Schrag, M. L., and Wienkers, L. C. (2005) Catalytic turnover of pyrene by CYP3A4: evidence that cytochrome b_5 directly induces positive cooperativity. *Arch Biochem Biophy,* **438**, 21-28.

88. Ekroos, M. and Sjögren, T. (2006) Structural basis for ligand promiscuity in cytochrome P450 3A4. *Proc Nat Acad Sci*, **103**, 13682-13687.

89. Williams, J. A., Hyland, R., Jones, B. C., Smith, D. A., Hurst, S., Goosen, T. C., Peterkin, V., Koup, J. R., Ball, S. E. (2004) Drug-drug interactions for UDP-glucuronosyltransferase substrates: a pharmacokinetic explanation for typically observed low exposure AUC_i/AUC ratios. *Drug Metab Dispos,* **32**, 1201-1208.

90. Kim, D. and Guengerich, F. P. (2005) P450 activation of aromatic and heterocyclic amines. *Annu Rev Pharmacol Toxicol,* **45**, 27-49.

91. Isin, E. M. and Guengerich, F. P. (2006) Kinetics and thermodynamics of ligand binding by cytochrome P450 3A4. *J Biol Chem,* **281**, 9127-9136.

92. Isin, E. M. and Guengerich, F. P. (2007) Multiple sequential steps involved in the binding of inhibitors to cytochrome P450 3A4. *J Biol Chem,* **282**, 6863-6874.

93. Yun, C-H., Kim, K-H., Calcutt, M. W., and Guengerich, F. P. (2005) Kinetic analysis of oxidation of coumarins by human cytochrome P450 2A6. *J Biol Chem,* **280**, 12279-12291.

94. Griffin, B. W. and Peterson, J. A. (1972) Camphor binding by *Pseudomonas putida* cytochrome P-450. Kinetics and thermodynamics of the reaction. *Biochemistry,* **11**, 4740-4746.

95. Chun, Y-J., Shimada, T., Sanchez-Ponce, R., Martin, M. V., Lei, L., Zhao, B., Kelly, S. L., Waterman, M. R., Lamb, D. C., and Guengerich, F. P. (2007) Electron transfer pathway for a streptomyces cytochrome P450. Cytochrome P450 105D5-catalyzed fatty acid hydroxylation in streptomyces coelicolor A3(2). *J Biol Chem,* **282**, 17486-17500.

96. Sandhu, P., Guo, Z., Baba, T., Martin, M. V., Tukey, R. H., and Guengerich, F. P. (1994) Expression of modified human cytochrome P450 1A2 in *Escherichia coli*: stabilization, purification, spectral characterization, and catalytic activities of the enzyme. *Arch Biochem Biophys,* **309**, 168-177.

97. Hanna, I. H., Teiber, J. F., Kokones, K. L., and Hollenberg, P. F. (1998) Role of the alanine at position 363 of cytochrome P450 2B2 in influencing the NADPH- and hydroperoxide-supported activities. *Arch Biochem Biophys,* **350**, 324-332.

98. Shiu, W-Y. and Ma, K-C. (2000) Temperature dependence of physical-chemical properties of selected chemicals of environmental interest. I. Mononuclear and polynuclear aromatic hydrocarbons. *J Phys Chem Ref Data,* **29**, 41-120.

99. Nebert, D. W. and Gelboin, H. V. (1968) Substrate-inducible microsomal arylhydroxylase in mammalian cell culture: assay and properties of induced enzyme. *J Biol Chem,* **243**, 6242-6249.

100. Bauer, E., Guo, Z., Ueng, Y-F., Bell, L. C., and Guengerich, F. P. (1995) Oxidation of benzo[*a*]pyrene by recombinant human cytochrome P450 enzymes. *Chem Res Toxicol,* **8**, 136-142.

101. Guengerich, F. P. and Bartleson, C. J. (2007) Analysis and characterization of enzymes and nucleic acids. *Principles and Methods of Toxicology*. 5th Ed. Hayes, A. W., Ed. CRC Press, Boca Raton, FL.

102. Kim, Y. D., Todoroki, H., Oyama, T., Isse, T., Matsumoto, A., Yamaguchi, T., Kim, H., Uchiyama, I., Kawamoto, T. (2004) Identification of cytochrome P450 isoforms involved in 1-hydroxylation of pyrene. *Environ Res,* **94**, 262-266.

103. Parikh, A., Gillam, E. M. J., and Guengerich, F. P. (1997) Drug metabolism by *Escherichia coli* expressing human cytochromes P450. *Nat Biotechnol,* **15**, 784-788.

104. Ueng, Y-F., Kuwabara, T., Chun, Y-J., and Guengerich, F. P. (1997) Cooperativity in oxidations catalyzed by cytochrome P450 3A4. *Biochemistry,* **36**, 370-381.

105. Chetiyanukornkul, T., Toriba, A., Kameda, T., Tang, N., and Hayakawa, K. (2002) Determination of 1-hydroxypyrene in human urine by high-performance liquid chromatography with fluorescence detection using a deuterated internal standard. *J Chromatogr A,* **961**, 107-112.

106. Raha, C. R. (1983) Thin-layer chromatographic separation and spectra of oxygenated benzo[*a*]pyrene derivatives in dichloromethane. *J Chromatogr A,* **264**, 453-458.

107. Burleigh, B. D., Jr., Foust, G. P., and Williams, C. H., Jr. (1969) A method for titrating oxygen-sensitive organic redox systems with reducing agents in solution. *Anal Biochem,* **27**, 536-544.

108. Guengerich, F. P., Krauser, J. A., and Johnson, W. W. (2004) Rate-limiting steps in oxidations catalyzed by rabbit cytochrome P450 1A2. *Biochemistry,* **43**, 10775-10788.

109. Foust, G. P, Burleigh, B. D., Jr., Mayhew, S. G., Williams, C. H., Jr., and Massey, V. (1969) An anaerobic titration assembly for spectrophotometric use. *Anal Biochem,* **27**, 530-535.

110. Schwede, T., Kopp, J., Guex, N., and Peitsch, M. C. (2003) SWISS-MODEL: An automated protein homology-modeling server. *Nucleic Acids Res,* **31**, 3381-3385.

111. Schuttelkopf, A. W. and van Aalten, D. M. (2004) PRODRG: a tool for high-throughput crystallography of protein-ligand complexes. *Acta Crystallogr D Biol Crystallogr,* **60**, 1355-1363.

112. Cambillau, C. and Roussel, A. (1997) *Turbo Frodo,* Version OpenGL.1, Université Aix-Marseille II, Marseille, France.

113. Brunger A. T., Adams, P. D., Clore, B. M., DeLano, W. L., Gros, P., Grosse-Kunstleve, R. W., Jiang, J. S., Kuszewski, J., Nilges, M., Pannu, N. S., Read, R. J., Rice, L. M., Simonson, T., and Warren, G. L. (1998) Crystallography & NMR system: a new software suite for macromolecular structure determination. *Acta Crystallogr D Biol Crystallogr,* **54**, 905-921.

114. Rice, L. M. and Brunger, A. T. (1994) Torsion angle dynamics: reduced variable conformational sampling enhances crystallographic structure refinement. *Proteins,* **19**, 277-290.

115. Launen, L., Pinto, L., Wiebe, C., Kiehlmann, E., and Moore, M. (1995) The oxidation of pyrene and benzo[*a*]pyrene by nonbasidiomycete soil fungi. *Can J Microbiol,* **41**, 477-488.

116. Lambert, M., Kremer, S., Sterner, O., and Anke, H. (1994) Metabolism of pyrene by the Basidiomycete Crinipellis stipitaria and identification of pyrenequinones and their hydroxylated precursors in strain JK375. *Appl Environ Microbiol,* **60**, 3597-3601.

117. Johnson, E. F, Schwab, G. E, and Muller-Eberhard, U. (1979) Multiple forms of cytochrome P-450: catalytic differences exhibited by two homogeneous forms of rabbit cytochrome P-450. *Mol Pharmacol,* **15**, 708-718.

118. McManus, M. E., Minchin, R. F., Sanderson, N., Schwartz, D., Johnson, E. F., and Thorgeirsson, S. S. (1984) Metabolic processing of 2-acetylaminofluorene by microsomes and six highly purified cytochrome P-450 forms from rabbit liver. *Carcinogenesis*, **5**, 1717-1723.

119. Yang, C. S., Tu, Y. Y., Koop, D. R., and Coon, M. J. (1985) Metabolism of nitrosamines by purified rabbit liver cytochrome P-450 isozymes. *Cancer Res,* **45**, 1140-1145.

120. Haugen, D. A. and Coon, M. J. (1976) Properties of electrophoretically homogenous phenobarbital-inducible and β-naphthoflavone-inducible forms of liver microsomal cytochrome P-450. *J Biol Chem,* **251**, 7929-7939.

121. O'Haver, T. C. and Green, G. L. (1976) Numerical error analysis of derivative spectrometry for the quantitative analysis of mixtures. *Anal Chem,* **48**, 312-318.

122. Guengerich, F. P. (1983) Oxidation-reduction properties of rat liver cytochrome P-450 and NADPH-cytochrome P-450 reductase related to catalysis in reconstituted systems. *Biochemistry,* **22**, 2811-2820.

123. Lehrer, S. S. (1997) Intramolecular pyrene excimer fluorescence: a probe of proximity and protein conformational change. *Methods Enzymol,* **278**, 286-295.

124. Lakowicz, J. R., Ed. (1999) *Principles of Fluorescence Spectroscopy*, 2nd Ed. Kluwer Academic/Plenum Publishers, New York.

125. Dabrowski, M. J., Schrag, M. L., Wienkers, L. C., and Atkins, W. M. (2002) Pyrene-pyrene complexes at the active site of cytochrome P450 3A4: evidence for a multiple substrate binding site. *J Am Chem Soc,* **124**, 11866-11867.

126. Greenfield, N. and Fasman, G. D. (1969) Computed circular dichroism spectra for the evaluation of protein conformation. *Biochemistry,* **8**, 4108-4116.

127. Kelly, S. M., Jess, T. J., and Price, N. C. (2005) How to study proteins by circular dichroism. *Biochim Biophys Acta,* **1751**, 119-139.

128. Quattrochi, L. C., Pendurthi, U. R., Okino, S. T., Potenza, C., and Tukey, R. H. (1986) Human cytochrome P-450 4 mRNA and gene: part of a multigene family that contains *Alu* sequences in its mRNA. *Proc Natl Acad Sci,* **83**, 6731-6735.

129. Gotoh, O. (1992) Substrate recognition sites in cytochrome P450 family 2 (CYP2) proteins inferred from comparative analysis of amino acid and coding nucleotide sequences. *J Biol Chem,* **267**, 83-90.

130. Wiebel, F. J., Selkirk, J. K., Gelboin, H. V., Haugen, D. A., van der Hoeven, T. A., Coon, M. J. (1975) Position-specific oxygenation of benzo[*a*]pyrene by different forms of purified cytochrome P-450 from rabbit liver. *Proc Natl Acad Sci,* **72**, 3917-3920.

131. Johnson, E. F. and Muller-Eberhard, U. (1977) Resolution of two forms of cytochrome P-450 from liver microsomes of rabbits treated with 2,3,7,8-tetrachlorodibenzo-*p*-dioxin. *J Biol Chem,* **252**, 2839-2845.

132. Girsch, P. and de Vries, S. (1997) Purification and initial kinetic and spectroscopic characterization of NO reductase from Paracoccus denitrificans. *Biochim Biophys Acta,* **1318**, 202-216.

133. Segel, I. H. (1975) *Enzyme Kinetics*, John Wiley & Sons, Inc., New York.

134. Johnson, K. A., Ed. (2003) Introduction to kinetic analysis of enzyme systems. *Kinetic Analysis of Macromolecules. A Practical Approach*, vol 267, Oxford University Press, Oxford, UK.

135. Roberts, A. G., Campbell, A. P., and Atkins, W. M. (2005) The thermodynamic landscape of testosterone binding to cytochrome P450 3A4: ligand binding and spin state equilibria. *Biochemistry,* **44**, 1353-1366.

136. Parikh, A., Josephy, P. D., and Guengerich, F. P. (1999) Selection and characterization of human cytochrome P450 1A2 mutants with altered catalytic properties. *Biochemistry,* **38**, 5283-5289.

137. Conney, A. H. (1982) Induction of microsomal enzymes by foreign chemicals and carcinogenesis by polycyclic aromatic hydrocarbons: G. H. A. Clowes memorial lecture. *Cancer Res,* **42**, 4875-4917.

138. Schrag, M. L. and Wienkers, L. C. (2000) Topological alteration of the CYP3A4 active site by the divalent cation Mg^{2+}. *Drug Metab Dispos,* **28**, 1198-1201.

139. Cinti, D. L. (1978) Agents activating the liver microsomal mixed function oxidase system. *Pharmacol Ther,* **2**, 727-749.

140. Schoch, G. A., Yano, J. K., Sansen, S., Dansette, P. M., Stout, C. D., and Johnson, E. F. (2008) Determinants of cytochrome P450 2C8 substrate binding: structures of complexes with montelukast, troglitazone, felodipine, and 9-*cis*-retinoic acid. *J Biol Chem*, **283**, 17227-17237.

141. Schoch, G. A., Yano, J. K., Wester, M. R., Griffin, K. J., Stout, C. D., and Johnson, E. J. (2004) Structure of human microsomal cytochrome P450 2C8: evidence for a peripheral fatty acid binding site. *J Biol Chem,* **279**, 9497-9503.

142. Wester, M. R., Yano, J. K., Schoch, G. A., Yang, C., Griffin, K. J., Stout, C. D., and Johnson, E. F. (2004) The structure of human cytochrome P450 2C9 complexed with flurbiprofen at 2.0- Å resolution. *J Biol Chem,* **279**, 35630-35637.

143. Warburg, O., Negelein, E., and Christian, W. (1929) Carbylamine-hemoglobin and the photochemical dissociation of its carbon monoxide compounds. *Biochem Z,* **214**, 26-63.

144. Imai, Y. and Sato, R. (1968) Dual effect of ethyl isocyanide on drug hydroxylation by liver microsomes. *J Biochem (Tokyo),* **63**, 380-389.

145. Ichikawa, Y. and Yamano, T. (1968) The electron spin resonance and absorption spectra of microsomal cytochrome P-450 and its isocyanide complexes. *Biochim Biophys Acta,* **153**, 753-765.

146. Imai, Y., Horie, S., Yamano, T., and Iizuka, T. (1978) in: Sato, R. and Omura, T., Eds. *Cytochrome P-450*, 37-135.

147. Imai, Y., Ito, A., and Sato, T. (1966) Evidence for biochemically different types of vesicles in the hepatic microsomal fraction. *J Biochem,* **60**, 417-428.

148. Shumyantseva, V. V., Bulko, T. V., Bachmann, T. T., Bilitewski, U., Schmid, R. D., and Archakov, A. I. (2000) Electrochemical reduction of flavocytochromes 2B4 and 1A2 and their catalytic activity. *Arch Biochem Biophys,* **377**, 43-48.

149. Yun, C-H., Miller, G. P., and Guengerich, F. P. (2001) Oxidations of *p*-alkoxyacylanilides by human cytochrome P450 1A2: Structure-activity relationships and simulation of rate constants of individual steps in catalysis. *Biochemistry,* **40**, 4521-4530.

150. Lampe, J. N., Floor, S. N., Gross, J. D., Nishida, C. R., Jiang, Y., Trnka, M. J., and Ortiz de Montellano, P. R. (2008) Ligand-induced conformational heterogeneity of cytochrome P450 CYP119 identified by 2D NMR spectroscopy with the unnatural amino acid (13)C-p-methoxyphenylalanine. *J Am Chem Soc,* **130**, 16168-16169.

151. Ryan, K. J. (1959) Biological aromatization of steroids. *J Biol Chem,* **234**, 268-272.

152. Akhtar, M., Calder, M. R., Corina, D. L., and Wright, J. N. (1982) Mechanistic studies on C-19 demethylation in oestrogen biosynthesis. *Biochem J,* **201**, 569-580.

153. Cole, P. A. and Robinson, C. H. (1991) Mechanistic studies on a placental aromatase model reaction. *J Am Chem Soc,* **113**, 8130-8137.

154. Hackett, J. C., Brueggemeier, R. W., and Hadad, C. M. (2005) The final catalytic step of cytochrome P450 aromatase: a density functional theory study. *J Am Chem Soc,* **127**, 5224-5237.

155. Bednarski, P. J. and Nelson, S. D. (1989) Dissociation of 19-hydroxy- 19-oxo-, and aromatizing-activities in human placental microsomes through the use of suicide substrates to aromatase. *J Steroid Biochem,* **32**, 309-316.

156. Fishman, J. and Goto, J. (1981) Mechanism of estrogen biosynthesis. Participation of multiple enzyme sites in placental aromatase hydroxylations. *J Biol Chem,* **256**, 4466-4471.

157. Simpson, E. R., Clyne, C., Rubin, G., Boon, W. C., Robertson, K. Britt, K., Speed, C., and Jones, M. (2002) Aromatase--a brief overview. *Annu Rev Physiol,* **64**, 93-127.

158. Johnston, S. R. and Dowsett, M. (2003) Aromatase inhibitors for breast cancer: lessons from the laboratory. *Nat Rev Cancer,* **3**, 821-831.

159. Altundag, K. and Ibrahim, N. K. (2006) Aromatase inhibitors in breast cancer: an overview. *Oncologist,* **11**, 553-562.

160. Hoover, D. M. and Lubkowski, J. (2002) DNAWorks: an automated method for designing oligonucleotides for PCR-based gene synthesis. *Nucleic Acids Res,* **30**, e43.

161. Sandhu, P., Baba, T., and Guengerich, F. P. (1993) Expression of modified cytochrome P450 2C10 (2C9) in *Escherichia coli*, purification, and reconstitution of catalytic activity. *Arch Biochem Biophys,* **306**, 443-450.

162. Patil, P. V. and Ballou, D. P. (2000) The use of protocatechuate dioxygenase for maintaining anaerobic conditions in biochemical experiments. *Anal Biochem,* **286**, 187-192.
163. Lephart, E. D. and Simpson, E. R. (1991) Assay of aromatase activity. *Methods Enzymol,* **206**, 477-483.

164. Zhou, D. J., Korzekwa, K. R., Poulos, T., and Chen, S. A. (1992) A site-directed mutagenesis study of human placental aromatase. *J Biol Chem,* **267**, 762-768.

165. Yun, C-H., Miller, G. P., and Guengerich, F. P. (2000) Rate-determining steps in phenacetin oxidations by human cytochrome P450 1A2 and selected mutants. *Biochemistry,* **39**, 11319-11329.

166. Richardson, T. H., Jung, F., Griffin, K. J., Wester, M., Raucy, J. L., Kemper, B., Bornheim, L. M., Hassett, C., Omiecinski, C. J., Johnson, E. F. (1995) A universal approach to the expression of human and rabbit cytochrome P450s of the 2C subfamily in *Escherichia coli*. *Arch Biochem Biophys,* **323**, 87-96.

167. Kellis, J. T., Jr. and Vickery, L. E. (1984) Inhibition of human estrogen synthetase (aromatase) by flavones. *Science,* **225**, 1032-1034.

168. Falk, J. E. (1964) *Porphyrins and metalloporphyrins; their general, physical and coordination chemistry, and laboratory methods*. Elsevier Pub. Co., Amsterdam, New York, pp 213-230.

169. Nakayama, K., Puchkaev, A., and Pikuleva, I. A. (2001) Membrane binding and substrate access merge in cytochrome P450 7A1, a key enzyme in degradation of cholesterol. *J Biol Chem,* **276**, 31459-31465.

170. Tomaszewski, M., Charchar, F. J., Maric, C., Kuzniewicz, R., Gola, M., Grzeszczak, W., Samani, N. J., and Zukowska-Szczechowska, E. (2009) Association between lipid profile and circulating concentrations of estrogens in young men. *Atherosclerosis*, **203**, 257-262.

171. Fishman, J. and Dixon, D. (1967) 2-Hydroxylation of estradiol by human placental microsomes. *Biochemistry,* **6**, 1683-1687.

172. Osawa, Y., Higashiyama, T., Shimizu, Y., and Yarborough, C. (1993) Multiple functions of aromatase and the active site structure; aromatase is the placental estrogen 2-hydroxylase. *J Steroid Biochem Mol Biol,* **44**, 469-480.

173. Shimizu, Y., Yarborough, C., and Osawa, Y. (1993) Competitive product inhibition of aromatase by natural estrogens. *J Steroid Biochem Mol Biol,* **44**, 651-656.

174. Johnson, K. A. (1998) Advances in transient-state kinetics. *Curr Opin Biotechnol,* **9**, 87-89.

175. Meigs, R. A. and Ryan, K. J. (1971) Enzymatic aromatization of steroids. I. Effects of oxygen and carbon monoxide on the intermediate steps of estrogen biosynthesis. *J Biol Chem,* **246**, 83-87.

176. Moslemi, S., Vibet, A., Papadopoulos, V., Camoin, L., Silberzahn, P., and Gaillard, J. L. (1997) Purification and characterization of equine testicular cytochrome P-450 aromatase: comparison with the human enzyme. *Comp Biochem Physiol B Biochem Mol Biol,* **118**, 217-227.

177. Dintinger, T., Gaillard, J. L., Moslemi, S., Zwain, I., and Silberzahn, P. (1989) Androgen and 19-norandrogen aromatization by equine and human placental microsomes. *J Steroid Biochem,* **33**, 949-954.

178. Garrett, W. M., Hoover, D. J., Shackleton, C. H., and Anderson, L. D. (1991) Androgen metabolism by porcine granulosa cells during the process of luteinization in vitro: identification of 19-oic-androstenedione as a major metabolite and possible precursor for the formation of C18 neutral steroids. *Endocrinology,* **129**, 2941-2950.

179. Silberzahn, P., Gaillard, J. L., Quincey, D., Dintinger, T., and Al-Timimi, I. (1988) Aromatization of testosterone and 19-nortestosterone by a single enzyme from equine testicular microsomes. Differences from human placental aromatase. *J Steroid Biochem* **29**, 119-125.

APPENDIX

I. DynaFit scripts for P450 1A2 work (Chapter II)

DynaFit script for the fitting of pyrene binding to P450 1A2. The fit resulting from this script is seen in Figure 28.

```
; all units in μM, s
 [task]
task = fit
data = progress
[mechanism]
E + S <===> ES : k1 k-1
ES + S <==> ESS : k2 k-2
ESS <==> SES : k3 k-3
[constants]
k1 = 4 , k-1 = 0.4
k2 = 4 , k-2 = 40
k3 = 4 , k-3 = 1
[responses]
ES = 0
ESS = 0.13
SES = 0.13
[concentrations]
E = 2
S = 2
[sweep]
mesh linear from 0 to 4 step 0.009
[progress]
file ./Scripts/EMIpyrenebind.txt
[output]
directory ./projects/SigmoidalRbP4501A2/output/run118
[end]
```

DynaFit script for the fitting of *v vs.* pyrene concentration data for the conversion of pyrene to 1-hydroxypyrene by P450 1A2. The fit resulting from this script is seen in Figure 29.

```
; all units in μM, min
[task]
data = velocities
task = fit
[mechanism]
```

```
E + S <==> ES : k1 k-1
ES + S <==> ESS : k2 k-2
ESS ---> ESP : k3
ESP <==> ES + P : k4 k-4
ESP ---> ES + Q : k5
ESS <==> SES : k6 k-6
[constants]
k1 = 240, k-1 = 24
k2 = 240, k-2 = 2400
k3 = 20
k4 = 180, k-4 = 240
k5 = 20
k6 = 240, k-6 = 60
[sweep]
[velocity]
variable S = from 1 to 30 step 1
file ./scripts/Sigmoid1OHpyrene1A2.txt
[concentrations]
E = 0.25
[responses]
P = 1, ESP = 1
[progress]
delay = 0.001
[output]
directory ./projects/SigmoidalRbP4501A2/output/run119
[end]
```

DynaFit script for the fitting of pyrene product formation by P450 1A2 data. The fit resulting from this script is seen in Figure 30.

```
; all units in μM, min
[task]
data = progress
task = fit
[mechanism]
E + S <==> ES : k1 k-1
ES + S <==> ESS : k2 k-2
ESS ---> ESP : k3
ESP <==> ES + P : k4 k-4
ESP ---> ES + Q : k5
ESS <==> SES : k6 k-6
[constants]
k1 = 240, k-1 = 24
k2 = 240, k-2 = 2400
k3 = 20?
k4 = 180, k-4 = 240
```

```
k5 = 20?
k6 = 240, k-6 = 60
[sweep]
mesh linear from 0 to 10 step 1
[concentrations]
E = 0.25, S = 20
[responses]
[progress]
directory ./scripts
variable Pyrene
file Newpyrenecourse.txt
responses S = 1, ES = 1, ESS = 1, SES = 1, ESP = 1
variable 1-OH pyrene
file 1OHpyrenecourse.txt
S-24
responses P = 1, ESP = 1
variable Di-OH pyrene
file DiOHpyrenecourse.txt
responses Q = 1
[output]
directory ./projects/SigmoidalRbP4501A2/output/run120
[end]
```

II. DynaFit scripts and Kintek Explorer® parameters for P450 19A1 work (Chapter IV).

DynaFit script for fitting the binding of andro (stopped-flow spectroscopy binding data). The fit resulting from this script is seen in Figure 44*A*.

```
; P450 19A1
;Kinetics of ligand binding
;All units in uM & s
;A390 SF data
;Andro
[task]
data = progress
task = fit
[mechanism]
E + L <==> EL        :        k1      k-1
EL <==> LE           :        k2      k-2
[constants]
k1 = 5,  k-1 = 1.4
k2 = 0.42, k-2 = 0.2
[concentrations]
```

```
E = 2
L = 2
[responses]
EL = 0
LE = 0.07
[sweep]
mesh linear from 0 to 30 step 0.032
[progress]
directory ./scripts
extension txt
file      2v2andro1
[output]
directory ./projects/ANDRO0909/run32
[end]
```

DynaFit script for fitting the steady-state titration data of andro binding using K_d values generated from the previous script. The fit resulting from this script is shown in Figure 45*A*.

```
;P450 19A1
;Kinetics of ligand binding
;All units in uM & s
;Andro
[task]
data = equilibria
task = fit
[mechanism]
E + L <==> EL          :          K1 dissoc.
EL <==> LE   :          K2 dissoc.
[constants]
K1 = 0.28
K2 = 2.1
[concentrations]
E = 1
[responses]
EL = 0
LE = 0.08
[sweep]
[equilibria]
variable L = 0 to 4.4 step 0.001
file ./scripts/androquadfit1.txt
[output]
directory ./projects/ANDRO0909/run31
[end]
```

DynaFit script for fitting the binding of 19-OH andro (stopped-flow spectroscopy binding data). The fit resulting from this script is shown in Figure 44*B*.

```
; P450 19A1
;Kinetics of ligand binding
;All units in uM & s
;A390 SF data
;19-OH andro
[task]
data = progress
task = fit
[mechanism]
E + L <==> EL          :        k1       k-1
EL <==> LE             :        k2       k-2
[constants]
k1 = 40,  k-1 = 240
k2 = 0.8, k-2 = 0.15
[concentrations]
E = 2
L = 2
[responses]
EL = 0
LE = 0.065
[sweep]
mesh linear from 0 to 30 step 0.032
[progress]
directory ./scripts
extension txt
file      2v219OH1
[output]
directory ./projects/19OH0909/run64
[end]
```

DynaFit script for fitting the steady-state titration data of 19-OH andro binding using K_d values generated from the previous script. The fit resulting from this script is shown in Figure 45*B*.

```
;P450 19A1
;Kinetics of ligand binding
;All units in uM & s
;titration data
;19-OH andro
[task]
data = equilibria
task = fit
[mechanism]
```

```
E + L <==> EL          :          K1 dissoc.
EL <==> LE             :          K2 dissoc.
[constants]
K1 = 6
K2 = 5.5
[concentrations]
E = 1
[responses]
EL = 0
LE = 0.0255
[sweep]
[equilibria]
variable L = 0 to 7.5 step 0.001
file ./scripts/19Ohquadfit1.txt
[output]
directory ./projects/19OH0909/run61
[end]
```

DynaFit script for the binding of 19=O andro (stopped-flow spectroscopy binding data). The fit resulting from this script is shown in Figure 44*C*.

```
;P450 19A1
;Kinetics of ligand binding
;All units in uM & s
;A390 SF data
;19=O aldo
[task]
data = progress
task = fit
[mechanism]
E + L <==> EL :        k1       k-1
EL <==> LE    :        k2       k-2
[constants]
k1 = 5,  k-1 = 300
k2 = 2.4, k-2 = 0.13
[concentrations]
E = 2
L = 2
[responses]
EL = 0
LE = 0.06
[sweep]
mesh linear from 0 to 30 step 0.032
[progress]
directory ./scripts
extension txt
```

```
file      2v2aldo
[output]
directory ./projects/ALDO091109/run14
[end]
```

DynaFit script for fitting the steady-state titration data of 19=O andro binding using K_d values generated from the previous script. The fit resulting from this script is shown in Figure 45*C*.

```
;P450 19A1
;Kinetics of ligand binding
;All units in uM & s
;sf data
;19=O andro
[task]
data = equilibria
task = fit
[mechanism]
E + L <==> EL          :          K1 dissoc.
EL <==> LE   :          K2 dissoc.
[constants]
K1 = 60
K2 = 18
[concentrations]
E = 1
[responses]
EL = 0
LE = 0.028
[sweep]
[equilibria]
variable L = 0 to 19.4 step 1
file ./scripts/aldoquadfit.txt
[output]
directory ./projects/ALDO091109/run16
[end]
```

Kintek Explorer® set-up for fitting the single turnover experiment (Figure 50).

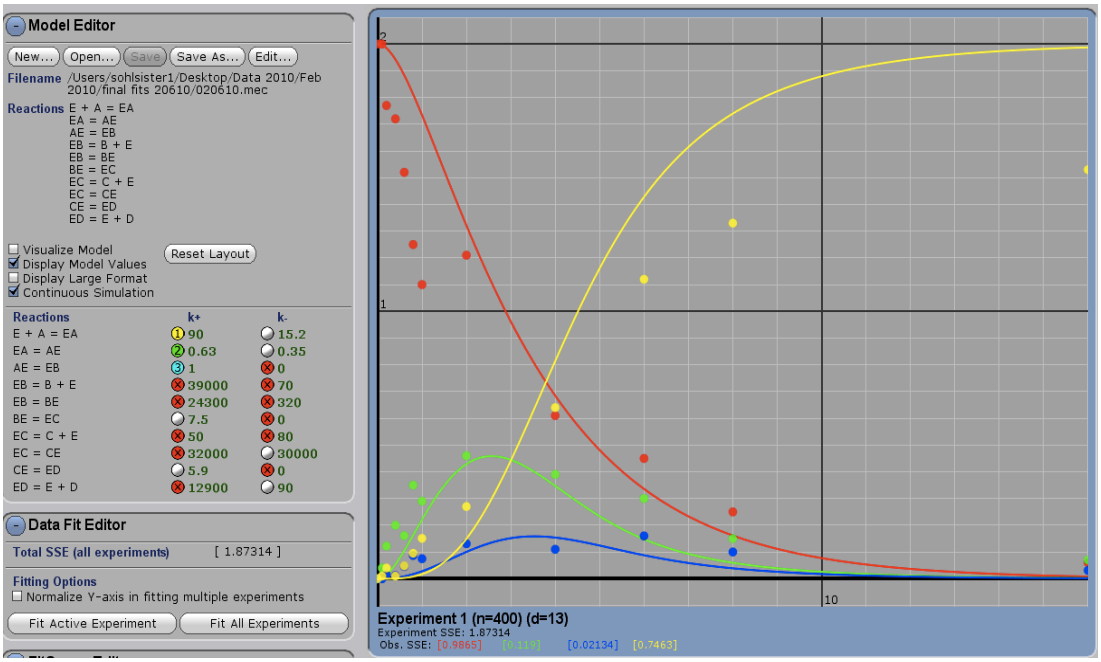

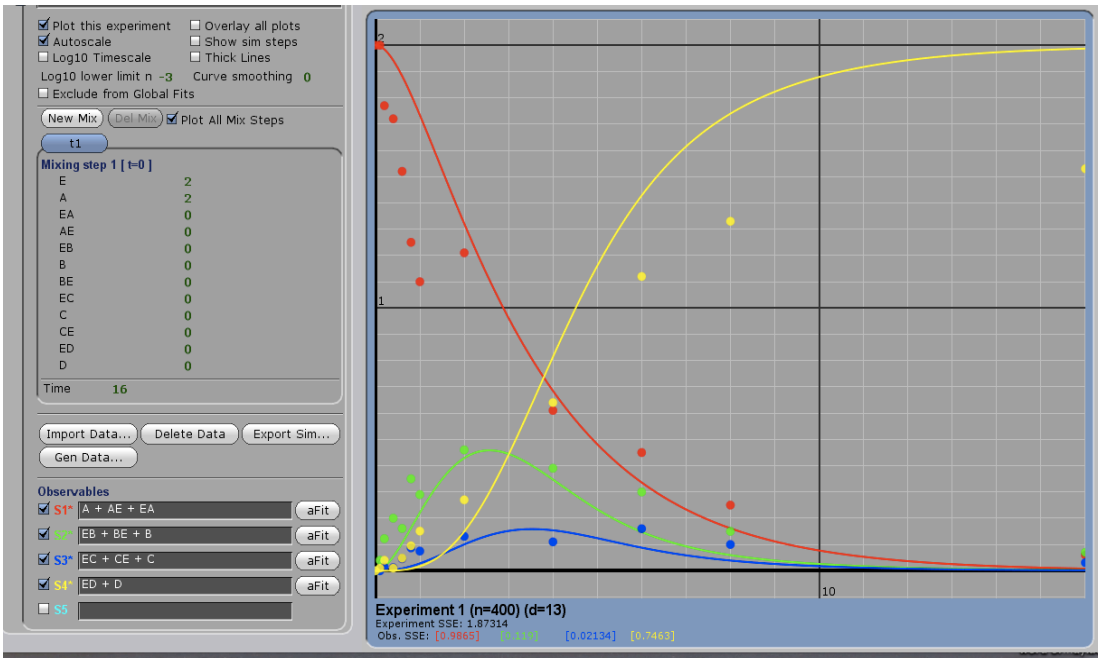

DynaFit iterations for global fitting. DynaFit script for fitting conversion of 19-OH andro to estrone. The fit resulting from the script is seen in Figure 51*A*.

```
;All units in uM, s
;A = andro, B = 19-OH andro, C = 19=O andro, D = estrone, E = 19A1
;19-OH v vs s
 [task]
data = velocities
```

```
task = fit
[mechanism]
B + E <==> EB        :        k1      k-1
EB <==> BE           :        k2      k-2
BE --> EC            :        k3
EC <==> E + C        :        k4      k-4
EC <==> CE           :        k5      k-5
CE --> ED            :        k6
ED <==> E + D        :        k7      k-7
[constants]
k1 = 70,         k-1 = 39000
k2 = 24300,    k-2 = 320
k3 = 7.5
k4 = 50, k-4 = 80
k5 = 32000, k-5 = 30000
k6 = 5.9
k7 = 12900, k-7 = 90
[concentrations]
E = 0.6
[progress]
delay = 0.01
[sweep]
[velocity]
variable B = 0, 8, 12, 15, 20, 40, 60, 100, 200, 300
file ./scripts/19Ohinsec.txt
responses D = 1
[output]
directory ./projects/19A101211019OH/run215
[end]
```

DynaFit iterations for global fitting. DynaFit script for fitting conversion of 19=O andro to estrone. The fit resulting from the script is seen in Figure 51*B*.

```
;All units in uM, s
;A = andro, B = 19-OH andro, C = 19=O andro, D = estrone, E = 19A1
;19=O v vs s
[task]
data = velocities
task = fit
[mechanism]
E + C <==> EC        :        k1      k-1
EC <==> CE           :        k2      k-2
CE --> ED            :        k3
ED <==> E + D        :        k4      k-4
[constants]
k1 = 80, k-1 = 50
```

k2 = 32000, k-2 = 30000
k3 = 5.9
k4 = 12900, k-4 = 90
[concentrations]
E = 0.1
[progress]
delay = 0.01
[sweep]
[velocity]
variable C = 0, 1, 5, 10, 15, 20, 40, 60, 100, 200, 300
file ./scripts/19Oinpersec.txt
responses D = 1
[output]
directory ./projects/19A101211019O/run240
[end]